Stick-Slip in Peeling of Soft Adhesives: a Finite Element Model Using Reversible Cohesive Elements

Evelyne Ringoot

In collaboration with:

Master thesis submitted under the supervision of
Professor Thierry J. Massart (Structural and Material Computational mechanics, ULB)

In collaboration with
Professor Tal Cohen (Cohen's Mechanics Group, MIT)
Professor Jean-François Molinari (Computational Solid Mechanics Laboratory, EPFL)
Thibault Roch (Computational Solid Mechanics Laboratory, EPFL)

In order to be awarded the master's degree in
Master of Science in Civil Engineering

Academic year 2019-2020

Stick-Slip in Peeling of Soft Adhesives: a Finite Element Model Using Reversible Cohesive Elements

Evelyne Ringoot

In order to be awarded the master's degree in Master of Science in Civil Engineering (2019-2020)

Abstract Soft adhesive pads attached to a rigid substrate show stick-slip behavior upon loading: they detach and reattach in a different location. This is accompanied by the lifting of the adhesive, the mechanical wave carrying this motion being known as a Schallamach wave. Especially for pads with a stiffer backing that are loaded parallel to the substrate, the reattachment behavior is crucial for the determination of the failure mechanism. Here we use finite element simulations to capture this kind of behavior, making use of tailored reversible cohesive elements allowing this type of reattachment. We manage to reproduce and explain the driving force for the behavior. While the observation of this type of Schallamach waves is widely recognized, and while numerical methods have been developed to deal with adhesion-friction coupling in adhesive spheres or cylinders, their representation past the instance of reattachment in finite element simulations of soft adhesive surface-surface interactions is new. We suggest that with rather limited and straightforward interventions in the cohesive law, reattachment can now be represented for soft adhesive detachment, but also in other fields. The better understanding of the mechanics driving this type of behavior and the different detachment modes, could inspire further applications in robotic grippers and even in earthquake engineering.

Keywords: Finite Element Method, Cohesive Elements, Stick-Slip, Schallamach Waves, Soft Adhesives, Surface Peeling

Acknowledgements

I would like to express my deepest gratitude to the people involved in this project: Professor Tal Cohen, Professor Thierry Massart, Professor Jean-François Molinari and Thibault Roch. Without them, I could not have achieved the results presented in this thesis.

I would like to thank Professor Tal Cohen for inviting me to join her group at the Massachusetts Institute of Technology to work on this thesis and for proposing this fascinating subject. Her passion for researching fundamental physical questions, has been the greatest inspiration. Her continuous availability for discussions, her insights in soft adhesive physics, in failure physics and her many suggestions on the critical points in the simulations and how to capture them, have been of paramount importance to this work. Her suggestions on the thesis writing and her personal support during this period have been immensely valuable as well. I would also like to thank all the members from Cohen's Mechanics Group for insightful discussions about adhesives and for the great atmosphere in the group.

I would like to thank Professor Thierry Massart for taking on this master thesis and for the great support throughout the entire year. His dedication to research work was tremendously motivating, and his continuous availability to discuss any challenges or questions, have allowed me to work on this thesis in the best possible conditions. His insights in the simulations, suggestions on how to advance them further, and how to treat numerical challenges have been crucial for the development of this model. Finally, his many detailed suggestions on how to improve the thesis writing allowed me to deliver the result of the research in an optimal way.

I would like to thank Professor Jean-François Molinari for inviting me to join his group at École Polytechnique Fédérale de Lausanne to work on developing the model for this thesis. His confidence in the project and his drive to achieve results, has motivated me to deliver the best result I could in this thesis. His help to set this project up, and his insights into failure mechanics have been essential as well. Further, I am incredibly thankful to Thibault Roch who helped me with the technical aspects of writing the code for the simulation development, and who was always available to answer any questions I had throughout the entire year. I also want to thank Thibault Roch and Professor Jean-François Molinari for proofreading the thesis.

In addition, I would like to thank all the members of Computational Solid Mechanics Laboratory LSMS for answering my questions on the use of Akantu. Next, I would like to acknowledge Ismail Honsali who provided me with the data from his master thesis and who was willing to answer my questions.

I would also like to thank the community of visiting students at the Massachussets Institute of Technology. Doing research and writing a thesis during the Covid-19 pandemic has been an unusual experience for all of us, and our community has been an enormous support during this period.

Lastly, I want to thank my family for their love and encouragement: my parents have been my biggest supporters all throughout my studies. Without them, this thesis would not have been possible.

Contents

List of Figures

List of Tables

1 Introduction

1.1 Soft Dry Adhesive Technology

Soft, dry adhesives are a subcategory of pressure-sensitive adhesives: they are elastomers with a very low stiffness. Because of their soft nature, they easily stick to hard surfaces upon application of pressure. Advances in dry soft adhesives technology and the corresponding production methods, have allowed to expand their application to robotics and even medicine. Some detailed examples are presented in Appendix A. The development of these applications has been possible thanks to more fundamental research on the general behavior of soft dry adhesives. In spite of all the research efforts, adhesion based mobility exhibited in the animal kingdom has yet to be matched in synthetic systems, and no unified theory predicting detachment mechanisms exists. This work has the aim to contribute to a better understanding of how soft adhesives work, to ultimately improve the existing applications, but also to feed the potential rise of new applications.

Examples of adhesion in nature include geckos and spiders that can climb on vertical reversed surfaces: their feet exhibit strong adhesive capacities and high-speed reversibility. The gecko for example, can hang from a wall with only one foot. In the time frame of less than 100 milliseconds, they can detach and reattach to a surface. This reversibility is unlimited, as the feet's adhesive capacity does not decline [Zhou et al., 2013]. Until now, a vast body of literature has been dedicated to understanding such natural adhesives, which have been shown to rely on Van Der Waals forces and thus allow detachment and full reattachment, even on rough surfaces. The high-speed movement has been explained by the hierarchical fibrillar structure of the feet (illustrated in Figure 1) and the directional adhesion. Geckos detach their feet by changing the angle between the surface and their feet, which is argued to be the main factor determining adhesive capacity [Autumn et al., 2002, Geim et al., 2003, Autumn et al., 2006]. This detachment can happen very fast, as they already subject their feet to frictional forces by sliding them over the surface during attachment. In this manner, the whole feet are subjected to a stress already during attachment and not much additional energy to reach detachment is necessary. As soon as the angle between the surface and the foot is then changed by the gecko's muscle movement, the whole foot will detach rapidly [Cheng et al., 2012].

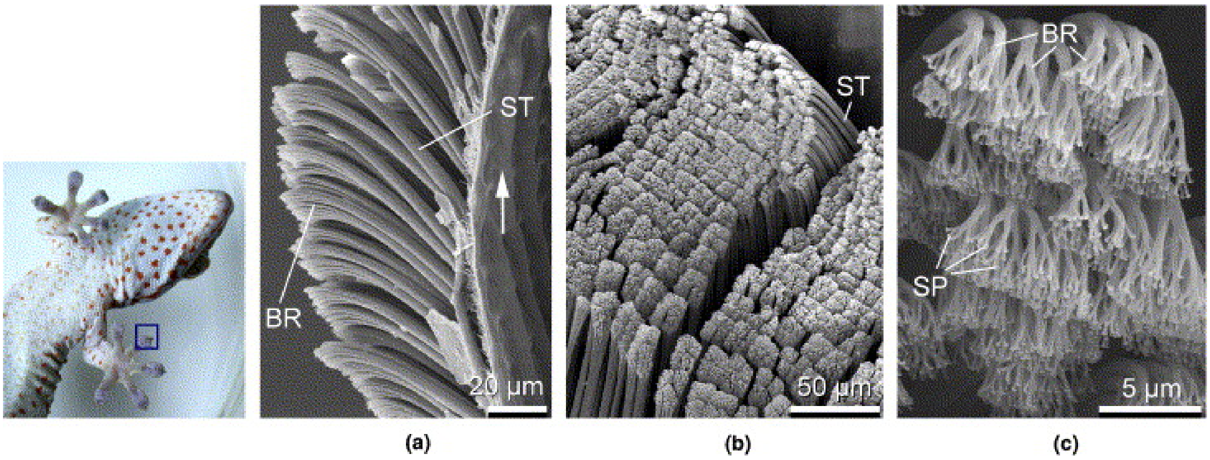

Figure 1: The fibrillar features in geckos that have been used to explain the exceptionally high adhesive capacity combined with the fast reversibility of adhesion on gecko feet. Figure from Gao et al. [2005].

While a large portion of the literature focuses on these fibrillar features and the directional adhesion properties [Gu et al., 2016, Brodoceanu et al., 2016, Li et al., 2016, Eisenhaure and Kim, 2017, O'Rorke et al., 2016], an alternative group of studies has been devoted to understanding how the stiffness of the adhesive surface layer is of importance. They state high adhesive strengths can be reached without fibrillar features, by using a bi-layered adhesive: a soft adhesive layer with a stiffer non-adhesive backing. This type of adhesive has shown large adhesive capacities on a stiff, smooth surface like glass [Jagota and Hui, 2011, Bartlett et al., 2012, Risan et al., 2015, Cohen et al., 2018, Liu et al., 2019].

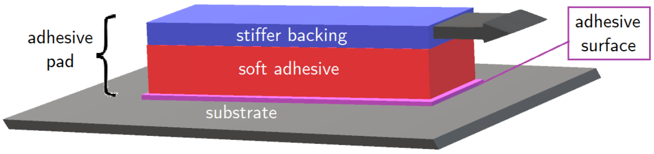

Figure 2: The zero-degree pulling test of the bi-layer adhesive. On the bottom is the stiffer surface to which the adhesive pad is adhered in black. The red and blue layers are polymers of finite thickness, while the red layer is an adhesive. The blue layer or backing is being pulled parallel to the surface.

Extensive research has been conducted on single-layer adhesives and their peeling behavior from a stiff substrate, as illustrated in Figure 3. The term peeling refers to the process of detachment of the surface area. A large part of the more recent research has focused on finding a physical explanation of experimentally observed failure behavior of soft adhesives, mostly under an angle, as evidenced by multiple review studies [Creton and Ciccotti, 2016, Noori et al., 2016, Federle and Labonte, 2019, Skopic and Schniepp, 2020], and for example the study of peeling of infinitely long pads under an angle by Xia et al. [2013] and Pesika et al. [2007], or the study of peeling of infinitely thin adhesive tapes [Yin et al., 2020, He et al., 2019a, Peng et al., 2019]. Some studies have already considered the bi-layer adhesive by considering a thin film under an angle with enhanced bending stiffness, thus for a linear case [Garg and Datla, 2019, Xia et al., 2013, Peng and Chen, 2015, Sauer, 2011a, Xu et al., 2019, He et al., 2019a]. Finite element models for these have been investigated as well [Wei, 2004, Thouless and Yang, 2008, Mohammed et al., 2013, Cheng et al., 2012, Biel and Stigh, 2017, Cheng et al., 2012].

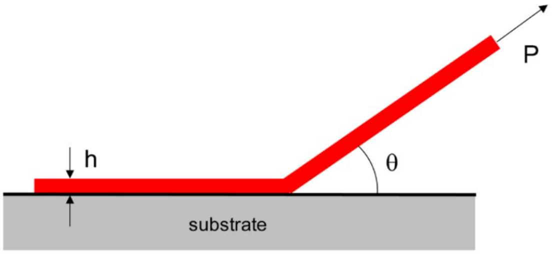

Figure 3: Illustration of the single-layer adhesive peeling test under an angle θ. The red material is the adhesive of a finite thickness h and pulled with a force P. Figure from Creton and Ciccotti [2016].

New research in the field continues as well. More recently, Eisenhaure and Kim [2018] investigated the influence of the degree of cross-linking on the adhesive properties of shape memory polymers, and Chopin et al. [2018] investigated the influence of visco-elastic behavior of the adhesive on its rate-dependent response. Ozbolat et al. [2018] also reported that the 3D printing of soft adhesives for medical applications significantly increases their strength of adhesion and bulk mechanical properties. A question still under investigation, refers to the production of controllable adhesives that can rapidly attach and detach [Croll et al., 2019, Risan et al., 2015]. Additional considerations on the extent of rate-dependence of the peeling behavior were scrutinized in Zhu et al. [2019].

1.2 Bi-layer Soft Adhesive Pads under a Zero-Degree Pulling Test and Stick-Slip

Bi-layer adhesive systems show especially interesting physics due to their high load-bearing capacity. This was demonstrated by the result of experimental and theoretical studies stating that the adhesive capacity of a polymer pad is related to the area of adhesion, but also inversely related to the compliance of the system. Thus, by artificially reducing compliance by adding a stiffer backing while keeping adhesive surface properties the same, the adhesive capacity can be increased [Risan et al., 2015, Bartlett et al., 2012]. An example of a peeling test of a bi-layer finite thickness adhesive is shown in Figure 2. Note that only the backing is pulled rather than the full adhesive.

Experimental studies [Ponce et al., 2015, Cohen et al., 2018] have shown that different failure modes exist and are competing in such pads: steady peeling from the pulled end of the pad or curling from the opposite end of the pad, shown in Figure 4 (a) and (b). Interfacial cavitation, the formation of an air bubble closer to the pulled end of the pad, shown in Figure 4 (c) has been observed as an intermediate failure mode before the occurrence of curling.

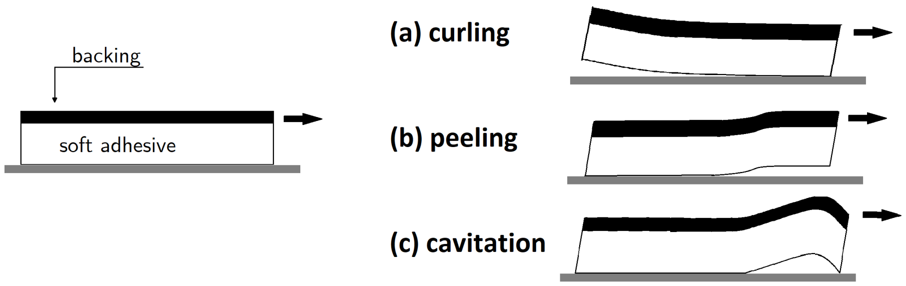

Figure 4: Failure modes of a bi-layer adhesive under a zero-degree adhesive. The Figure on the left is the initial configuration. Figure (a) on the right top shows curling from the opposite end of the pad, Figure (b) shows peeling from the pulling end of the pad while Figure (c) pictures cavitation. Figures inspired by Cohen et al. [2018].

Theoretical studies [Cohen et al., 2018] have determined the shape of an adhesive pad based on its material and geometric characteristics using an energy minimization approach. Assuming the location with the largest vertical displacement at the surface will be the location where the first failure occurs, the conditions for two different failure initiation modes were then identified: the cavitation and the curling modes. A different theoretical approach [Ponce et al., 2015, Mojdehi et al., 2017a,b] studied over which length the shear stress decays in the pad. This is called the shear lag length (Figure 5) and is a function of the material properties involved. If the adhesive length is a lot lower than this length, the full adhesive part will be under uniform shear and fail catastrophically. In the case the adhesive length is higher than the shear lag length, this shear lag length will detach and from there a steady peeling front will propagate from the pulling end.

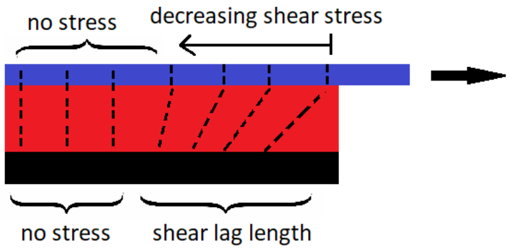

Figure 5: The shear lag length observed in the bi-layer pad under zero-degree pulling from the backing. Over the length of the backing the shear stress decreases, it is distributed over the adhesive over a longer length as the iso-stress lines run diagonally. The shear lag length is a function of material parameters of adhesive and backing. It is argued that the ratio between the pad length and shear lag length determines the failure mode. Figure adapted from Ponce et al. [2015].

While the available theoretical studies manage to capture and parametrically describe the conditions and the location of the first initial failure, they do not include the phase of subsequent failure propagation until full failure of the pad. This phase between failure initiation and full failure is especially challenging under zero-degree tests (angle of $\phi = 0°$ in Figure 3), as these can generally not be described by theories for arbitrary loading angles [Yamaguchi et al., 2016]. The reason for this is the stick-slip or sliding behavior of the adhesive on the surface: after partial detachment of the adhesive surface close to the pulled end, this part can reattach again further along the substrate surface. It reattaches upon contact with the substrate and displays again adhesive and frictional forces. Experimental evidence of this phenomenon in zero-degree pulling test has repeatedly been found [Cohen et al., 2018, Ponce et al., 2015, Amouroux et al., 2001, Collino et al., 2014, Zhu et al., 2019, Baumberger et al., 2002, Cortet et al., 2007, Zotti et al., 2019]. Evidence of occurrence of the same phenomenon (albeit to a lesser extent) was also found in the peeling test under an angle [Collino et al., 2014, Dalbe et al., 2015]. This behavior causes drops and re-increases in the force-displacement curve of the peeling tests, as is shown in Figure 6. These are believed to be caused by detachment and re-attachment of the peeling front [Begley et al., 2013, Lake and Stevenson, 1981].

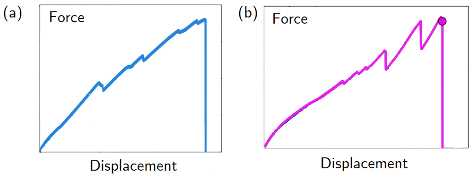

Figure 6: Experimental force-displacement curves of the zero-degree peeling test of bi-layer adhesives (displacement controlled), Figures adapted from Cohen et al. [2018] (a) and Ponce et al. [2015] (b). The x-axis shows displacement and the y-axis forces, units have been removed. In the curves, there appear multiple drops and re-increases in the force, that have been linked to reattachment. Both studies' results show the same type of behavior.

This stick-slip behavior is one of the ways in which instabilities during sliding in soft adhesives manifest. Frictional instability during sliding contact between hard materials on the micro- and nano-scale have been widely studied in the field of contact tribology [Wang and Chung, 2013, Johnson, 1985]. In contact between soft materials with a finite thickness such as rubber or PDMS (polydimethylsiloxane) with a smooth rigid substrate such as glass, the propagation of attachment-detachment front has been observed by Schallamach [1971] in the contact between a small sphere and a flat substrate. It is therefore commonly referred to as a Schallamach wave. The experimental setup used by Schallamach [1971] is shown in Figure 7 (a). Stick-slip is then the description of the behavior of the soft material during the movement of this Schallamach wave: it slips while detaching and reattaches or sticks later, as illustrated in Figure 7 (b). Finally, the force necessary to move the sphere over the surface oscillates around a constant frictional value as shown in Figure 7. Viswanathan et al. [2016b] have defined different subcategories of stick-slip events depending on the properties of the detachment front and frictional force reaction. However, all waves share the characteristics of propagating a cavitation-like shape on the surface and all frictional forces share the oscillation around a constant value.

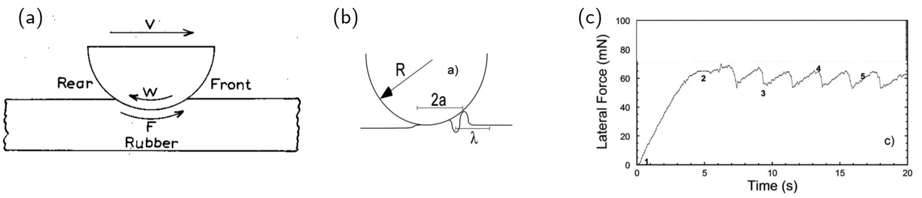

Figure 7: Illustration showing Schallamach waves, stick-skip, and their relation. In Figure (a) from Schallamach [1971], a half glass sphere is indented in a semi-infinite surface of rubber and moves parallel to the surface with speed v. The rubber exhibits a frictional force F. In Figure (b) from Rand and Crosby [2006] surface wrinkling or cavitation formation after the ball has moved is shown. Part of the rubber has detached from the glass. This surface behavior is referred to as slip: the detached part has slipped from the surface. Afterwards it will reattach: stick behavior. This will continue as the ball moves forward and the propagation of the attachment-detachment front is referred to as a Schallamach wave [Schallamach, 1971]. Figure (c) from Rand and Crosby [2006] shows the associated variation of the driving force, showing an oscillation around a constant frictional force.

More experimental and theoretical studies have been conducted on the appearance of these waves in sphere-surface, cylinder-surface or sphere-sphere contacts [Gabriel et al., 2010, Maegawa et al., 2016, Mishra et al., 2015a, Maegawa and Nakano, 2010, Schapery, 2020, Fukahori et al., 2010, Viswanathan et al., 2016a, Rand and Crosby, 2006, Lin and Hui, 2002, Barthel and Haiat, 2002, Das et al., 2013, Cortet et al., 2013]. Finite element models used in these studies describe the development of the detachment, the formation of the first Schallamach waves, but they do not include reattachment. An analytical study by Nakano and Maegawa [2009] considered the case of a small block sliding against a large surface, predicting how to prevent stick-slip. However, contrary to the occasional stick-slip in an increasing force curve like in Figure 7, the force obtained here is a periodic oscillation around a constant value like in Figure 7 (c). The driving mechanism behind the formation of Schallamach detachment fronts is argued to be buckling caused by compression-tension fields forming before and after the indentation [Gabriel et al., 2010, Schallamach, 1971]. This is shown in Figure 8: during the movement of the sphere over the rubber, where the rubber surface is compressed in front of the slider and is subjected to tension behind the surface. The couple created by these fields causes buckling of the surface. Mathematical proof of this was provided by Mishra et al. [2015b]. Moreover, the analytical studies by Brochard-Wyart and de Gennes [2007] and Memet et al. [2020] provide analytical evidence of the link between oscillations in the force-displacement curve and the stick-slip events on the surface.

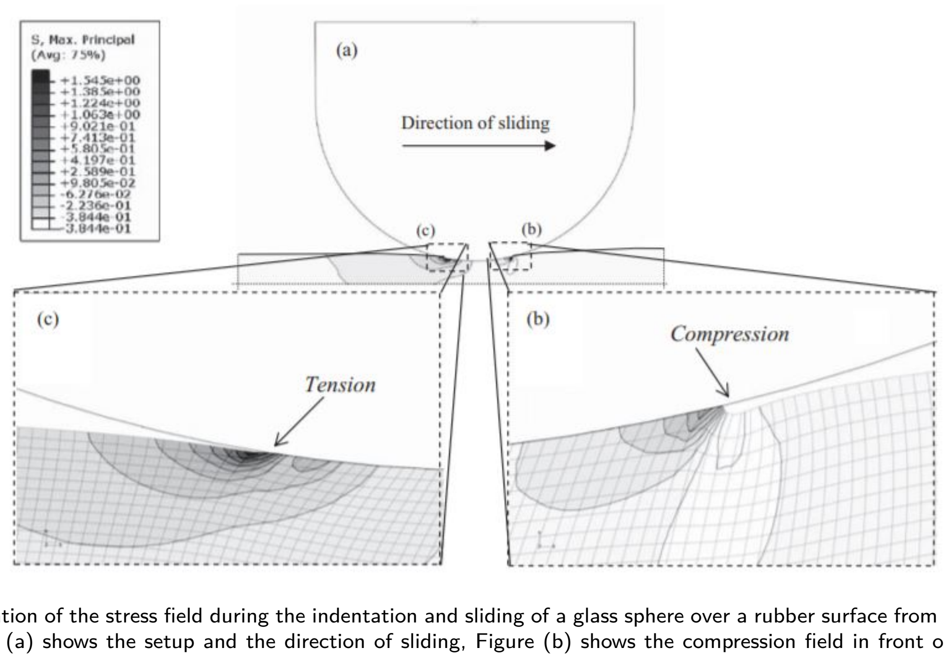

Figure 8: Variation of the stress field during the indentation and sliding of a glass sphere over a rubber surface from Gabriel et al. [2010]. Figure (a) shows the setup and the direction of sliding, Figure (b) shows the compression field in front of the sphere, and Figure (c) shows the tension field behind the sphere. It is argued these fields cause buckling.

More recently, finite element formulations have been developed to deal with the friction-adhesion contact coupling present on the contact surface [Cocou et al., 2010, Mergel et al., 2020, 2019, Raous, 2011, Khajeh Salehani et al., 2019, Sauer, 2016], both on a molecular and larger scale. These have been applied to single-layer adhesive peeling under an angle larger than zero degrees or to sphere-surface interactions [Gouravaraju et al., 2020, Mergel et al., 2020]. Meanwhile, another branch of research has simultaneously observed that modeling the adhesion-friction coupling is not critical for correct simulation of a soft adhesive, rather the finite deformations in the bulk material carry larger importance [Liu et al., 2019, Lengiewicz et al., 2020, Villey et al., 2015]. Yet, other researchers argue it is the mixed-mode (not pure mode I or mode II) failure behavior that is crucial [Waters and Guduru, 2010, Papangelo and Ciavarella, 2019]. A consensus has however not been reached so far, although the friction-adhesion contact coupling is the most supported hypothesis today.

Despite the interest in a proper understanding of Schallamach waves, their appearance in flat-surfaced soft adhesive pads against large flat substrate surfaces has not been widely studied yet. Of the studies that do, Ronsin et al. [2011] describe experiments on surface-surface sliding under pure shear. They found Schallamach waves propagating and analytically predicted their propagation speed. Baumberger et al. [2003] did the same type of experiments, providing evidence of velocity-dependence of the stick-slip events. The studies by Pan et al. [2009], Mukherjee and Sharma [2015] and Sarkar and Sharma [2010] describe parametrically the development of surface wrinkling of a thin elastic film on a substrate: multiple characteristic length scales of the wrinkling behaviors are reported. Finally, Honsali [2018] proposed a finite element model showing bi-layer adhesive pad detachment from a rigid surface without reattachment.

To the best of our knowledge, to date, no finite element simulation concerning surface-surface interaction has been able to capture the reattachment phenomena necessary for studying stick-slip behavior of the type observed in zero-degree peeling tests. Understanding the parameter values under which this phenomenon occurs and which effect this has on the global behavior of the adhesive pad, would pave the way to engineer the pads for specific applications.

It is to be noted that the manifestation of surface wrinkling waves is not limited to glass-soft polymer contacts or to detachment problems: they have been omnipresent in contact sliding settings. They have been observed in solid-solid interactions and on an atomic level [Ronsin et al., 2011, Wang and Chung, 2013, Gerde and Marder, 2001, Johnson, 1985], but they have also been linked to seismic waves that cause earthquakes [Ronsin et al., 2011, Galeano et al., 2000, Festa et al., 2010, Uenishi and Rice, 2003], and are historically referred to as self-healing slip pulses instead of Schallamach waves. Similarities between tectonic plate movements and adhesive surfaces sliding become immediately apparent in Figure 9. The same mechanical reasoning of compression-tension localization causing the slip has been provided and this phenomenon is now referred to as Heaton waves [Heaton, 1990]. Recently, hydrogel-solid interactions have been exploited as well as a means to study seismic activity in depth [Galeano et al., 2000, Ronsin et al., 2011].

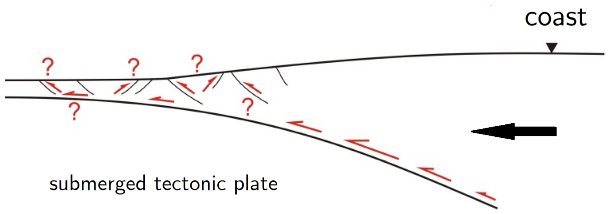

Figure 9: Tectonic plate sliding from Wang and Tréhu [2016], show a thick coastal plate (top) that is thinner on the left, sliding over a submerged tectonic plate and creating friction fields on the interface. On the transition zone between the top plate being thick and thin, sliding moments appear that cause slip waves and seismic activity. According to Wang and Tréhu [2016] they have yet to be explained.

1.3 Outline

As has been proven earlier by experiments, reattachment behavior or stick-slip motion is crucial for the correct representation of adhesive failure in pads, especially if loaded parallel to their substrate. Finite element simulations have not earlier investigated stick-slip behavior in surface-surface interaction of soft adhesives with a stiff substrate. Being able to model this behavior, will allow to gain more insight into the different failure modes of this type of adhesive pads and their driving forces. This understanding of the fundamental mechanism underlying detachment of the adhesives in function of their parameters, could provide an insight into how to engineer pads for specific applications. The understanding of this mechanism could even be extended to other fields where the Schallamach waves are observed, such as in earthquake engineering. Furthermore, these insights might inspire new applications or allow to improve current applications such as robotic grippers.

In this study, we will specifically look at the case of a soft adhesive pad with a stiffer backing being pulled under a zero-degree angle. A finite element model will be deployed and the effect of reattachment will be implemented in this model. Ultimately, we wish to represent experiments well in terms of development of detachment, explain their behavior, and predict under which conditions stick-slip will occur. Section 2 shows the physical situation description with all relevant parameters and Section 3 gives an overview of the experimental results for this type of setup. A finite element model is developed to solve the problem and Section 4 details the development of this model. Next, Section 5 shows the observed failure modes, stick-slip phenomena, and their correspondence to experimental results, as well as the mechanics of the failure modes and the stick-slip behavior. Section 6 then continues to explore under which general configuration stick-slip occurs. Finally, limitations and discussion of the relevance of the results can be found in Section 7.

2 Description of Setup

Consider a soft polymeric adhesive of length L and thickness t that is perfectly attached to a stiffer backing of thickness t_b and placed on a smooth, infinitely stiff substrate, as illustrated in Figure 10. The study is limited to adhesives that fail by detachment at the interface (adhesive surface in Figure 10) between the soft adhesive and the substrate, and do not exhibit failure inside the adhesive. One side of the backing perpendicular to the pad length is being pulled parallel to the substrate and is not allowed to move in the direction perpendicular to the surface.

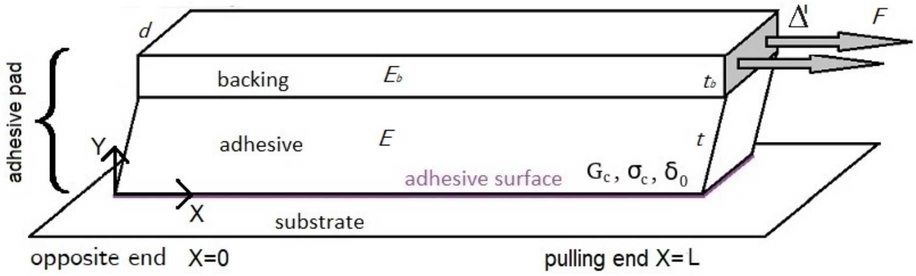

Figure 10: Physical configuration of the system with the different variables indicated: bi-layer adhesive pad with soft adhesive, stiffer backing, and adhesive surface attached to the rigid smooth substrate. Shown on the Figure are the stiffness of adhesive and backing E and E_b, the properties of the adhesive surface (surface energy G_c, ultimate surface strength σ_c, normalized opening at initiation of the softening phase δ_0), the geometric dimensions (length L, thickness of backing t_b and adhesive t, depth of the pad d), the pulling force F and the pulled distance Δ'. Right is the pulling end and left is the opposite end.

The Young's modulus of the adhesive and the backing are respectively E and E_b. The bulk properties are characterized by the following non-dimensional parameters [Cohen et al., 2018]:

$$\alpha = \frac{t_b}{t} \qquad \beta = \frac{E_b \cdot \alpha}{E} \qquad \frac{L}{t} \tag{1}$$

The adhesive and the backing are considered neo-hookean materials. The neo-hookean material law is a good trade-off between simplicity of the model and accuracy of the results. For rubber-like behavior with large strains, a linear elastic model is indeed insufficient [Kim et al., 2011b]. More accurate material laws require more detailed material data and increase complexity and thus calculation time. The neo-hookean law combines computational and physical simplicity with good results, even at moderately high amounts of strain up to around 200 % [Kim et al., 2011a, Marckmann and Verron, 2006, Martins et al., 2006]. As such, in the scope of this study, we will assume that large deformations higher than 200 % do not have a significant influence on the detachment mode of the adhesive, such that the approximation provided by the neo-hookean model is sufficient. The neo-Hookean law for a three-dimensional compressible material is characterized by the following strain energy density function W [Abeyaratne, 1988]:

$$W = \frac{\mu}{2}(I_1 - 3 - 2 - ln(J)) + \frac{\lambda}{2}(J-1)^2 \tag{2}$$

Where λ and μ are Lamé's first and second parameter, I_1 is the first invariant of the right Cauchy-Green deformation tensor and J is the determinant of the deformation gradient.

The neo-Hookean law matches the linear elastic law at small deformations and exhibits a less stiff response as stretch increases as illustrated in Figure 11 for the case of an incompressible material under uniaxial stress, thus providing better correspondence to the physical behavior at moderate and large strains.

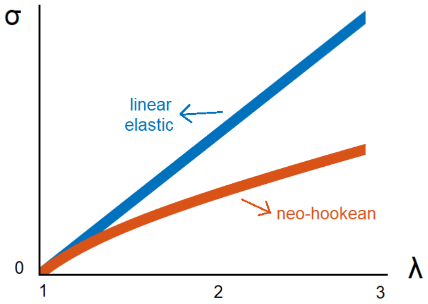

Figure 11: Comparison between the stress-stretch response of an isotropic incompressible sample under uniaxial stress of the neo-hookean and the linear elastic material law. At low stretches, both laws correspond. As stretch increases, the behavior of the neo-Hookean law shows softening, thus better representing physical behavior for moderate and large strains.

The adhesive surface response is assumed to exhibit a linear elastic phase where stress increases with bond stretch until maximal stress, and a linear softening phase from the maximal stress until zero stress where the stress decreases as bond stretch further increases, as illustrated in Figure 12.

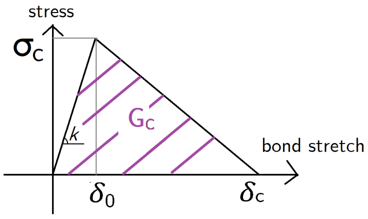

Figure 12: Illustration of the bond stretch - stress assumption for the adhesive surface. The bond stretch is expressed in units of length. The slope of the initial stiffening phase going from bond stretch 0 to bond stretch δ_0 is k. The area under the curve is bond failure energy G_c and the failure stretch is δ_c.

This behavior can be identified by 3 independent and 2 dependant material parameters. As independent parameters we choose the elastic bond stiffness k that relates traction and opening before the onset of softening of the adhesive surface, the peak strength σ_c, and the energy at complete detachment G_c. Further, κ relates the amount of energy in mode I fracture to the amount of energy in mode II fracture. This results in non-dimensional parameters ζ, θ and γ, defined as:

$$\gamma = \frac{kt}{E} \qquad \zeta = \frac{\sigma_c}{E} = \gamma\frac{\delta_0}{t} \qquad \theta = \frac{G_c}{Et} = \gamma\frac{\delta_0\delta_c}{2t^2} = \zeta\frac{\delta_c}{2t} \qquad \kappa = \frac{G_{c,II}}{G_{c,I}} \tag{3}$$

The other surface parameters are the values of the opening at peak strength $\delta_0 = \sigma_c/k$ and the opening at full detachment $\delta_c = \frac{2G_c}{\sigma_c}$. Note that $\delta_c > \delta_0$ or $\theta > \zeta^2\gamma$, because the opening at the completion of failure needs to be higher than the opening at the initiation of failure.

Finally, the level of loading of the adhesive pad at the pulling location can be described by the prescribed pulling displacement Δ' and pulling force F and their non-dimensional counterparts, defined as:

$$\Delta = \frac{\Delta'}{t} \qquad \frac{F}{E \cdot td} \tag{4}$$

3 Experimental Studies

Prior to this work, experiments on the zero-degree peeling of bi-layer adhesives were done by Honsali [2018] and Cohen et al. [2018]. We were kindly provided with the experimental data. First, stick-slip was observed in the pulling force diagrams. Secondly, two main failure modes are observed: the formation of an interfacial cavitation close to the pulling end followed by peeling for longer pads and unstable curling from the opposite end for shorter pads.

The material parameters used for the experiments in both studies are:

	Thickness		**Depth**	**Young's modulus**	
	adhesive	**backing**		**adhesive**	**backing**
Honsali [2018]	6.25 mm	4 mm	30 mm	700 kPa	20 MPa
Cohen et al. [2018]	8.3 mm	2.4 mm	30 mm	170 kPa	2 MPa

Table 1: Material parameters used for experiments on the zero-degree peeling test of a bi-layer adhesive.

Cohen et al. [2018] reported the pure curling from the opposite end as the failure mode for pads with shorter lengths ($l/t = 3.6$) and interfacial cavitation, followed by curling for longer pad lengths ($l/t = 11$). In the force diagrams from this study shown in Figure 13, stick-slip is visible only for the experiments that show interfacial cavitation close to the pulling end as a failure mode (the longer pads) as opposed to curling from the opposite end (shorter pads). A failure force of 20 N for interfacial cavitation and 2 N for pure curling is reported.

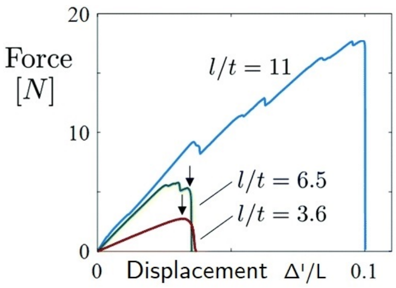

Figure 13: Figure of the force - imposed displacement graphs for the experiments done by Cohen et al. [2018]. On the y-axis the imposed force is shown and the x-axis the imposed displacement Δ', normalized by the pad length L is shown. Different pad lengths are used with the same thickness and the same material properties and the results for pad lengths $l/t = 3.6$, $l/t = 6.5$ and $l/t = 11$ are shown.

The images from the experiments that will be discussed next, detailing the development of failure in the adhesive, are taken from below the adhesive pad as shown in Figure 14. When we will be discussing the 2D simulations later, the perspective will be from the front of the adhesive (also shown in Figure 14) as this will allow to look at the state of the full pad in addition to the failure state.

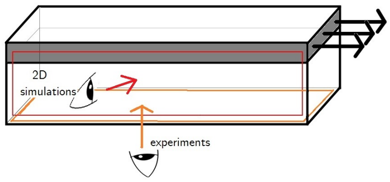

Figure 14: Illustration of the perspective from which the images from the experiments shown here and the images from the simulations that will be shown later are taken. The bi-layer adhesive pad pulled parallel to its surface is shown in the middle with the 2D simulation perspective looking at the front of the pad and the experimental perspective looking at the bottom of the pad.

Honsali [2018] observed the same failure modes and provided videos of the experiments. In Figure 15a the curling mode of detachment is shown, with the amount of imposed displacement increasing from Figure (I)-(IV). Figure (I) shows no detachment, and as pulling continues the first detachment areas are formed at the opposite end (II) and propagate rapidly (III) until full failure (IV). This sudden, catastrophic mode of detachment is characteristic for curling. In Figure 15b the experiment with the same materials but with a longer pad is shown: the imposed displacement increases between Figures (I)-(VII). A detached region close to the pulling end, named an interfacial cavitation, is the first detached region to develop in Figures (I.b)-(III). After this, part of the detached region close to the front of the detachment region reattaches in Figure (IV), stick-slip phenomena accompanied by Schallamach waves occur. Finally, from the opposite end of the pad a second detachment region propagates rapidly (V) and the pad fails (VI).

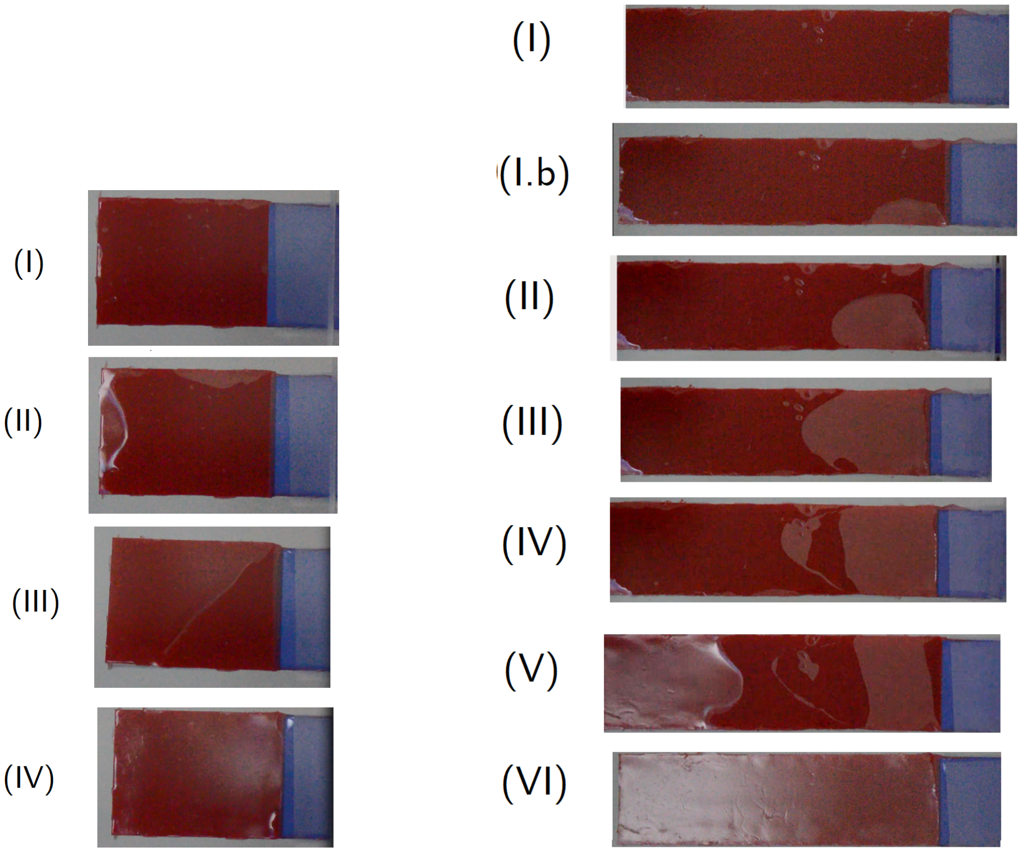

(a) Figure (I)-(IV) show the propagation of failure while displacement is increased for a shorter pad that shows curling behavior. (I) no failure is observed, the pad is placed under loading. (II) The opposite end shows the first detached region. (III-IV) This detached region quickly propagates further. First, half of the pad is detached (III) and next, the full pad is detached (IV).

(b) Figure (I)-(VI) show the propagation of failure while displacement is increased for a longer pad that shows interfacial cavitation behavior and stick-slip. (I) no failure is observed, the pad is placed under loading. (I.b) The first small detached regions show the most significant one near the pulling end at the side of the pad. (II-III) The propagation of the detached region near the pulling end continues. (IV) A first reattached region is observed close to the propagation front of the detached region. (V) The detachment at the opposite end starts and propagates fast over the pad. (VI) The pad is fully detached.

Figure 15: Images from the bottom of the bi-layer adhesive pad during experiments showing the detachment under a zero-degree peeling test as described in Section 1.2. Two main failure modes were observed during the experiments: curling as shown on (a) and interfacial cavitation followed by curling as shown on (b). Movies from which the images were extracted provided by Honsali [2018].

The failure states development shown in Figure 15 are also systematically represented in an imposed displacement (vertically increasing with an increasing axis) versus position along the pad length diagram in Figure 16. In these plots x=0 is located at the left-hand side of the pad and as the pad is pulled at the right at $x = L$. The consecutive states of the pad are vertically joined here, showing the development of the detachment regions as the imposed displacement increases. The light red regions mean detached zone and dark red zones are attached. Figure 16a shows the curling behavior at the opposite end for the short pad discussed earlier and Figure 16b shows the interfacial cavitations at the pulling end, reattachment (visible for an interfacial cavitation region that shrinks in size after initial development as the imposed displacement goes up) and curling behavior development for the longer pad discussed earlier. In Figure 16a it is seen the curling propagates faster near the end of the simulation, as evidenced by the change of slope indicated by number (1). In Figure 16b it is visible the interfacial cavitation keeps approximately the same length all throughout the experiment (except for the initial reattachment region, number 2 on the figure) and that the front of the original detachment region, where reattachment is formed behind (almost vertical left dashed black line, number 1), ultimately joins the curling region.

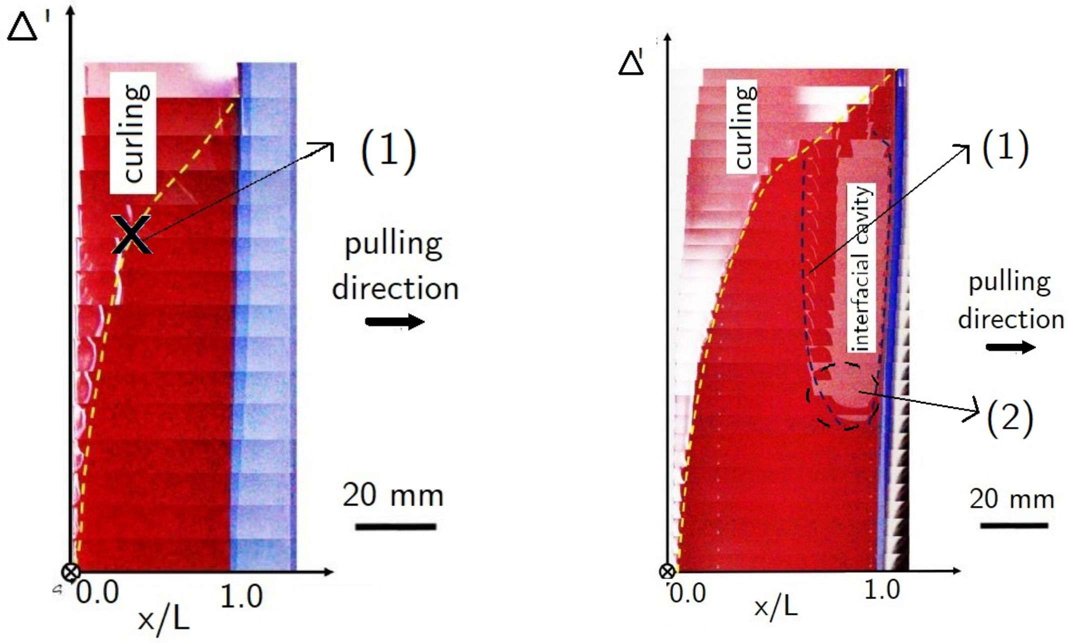

(a) Pad position-displacement graph of the failure of the shorter pad that exhibits curling. Composition of the different failure states from Figure 15a. The light red regions mean detached zone and dark red zones are attached. The curling behavior, detachment from the opposite end, is shown with a yellow dashed line. In the middle of the figure, the increase in velocity of the curling is marked with (1). Figure adapted from Honsali [2018].

(b) Pad position-displacement graph of the failure of the longer pad that exhibits interfacial cavitation, stick-slip, and finally curling. Composition of the different failure states from Figure 15b. The failure behavior: interfacial cavitation (from the pulling end) and curling (detachment from the opposite end), is shown with respectively a black and a yellow dashed line. The initiation of the interfacial cavitation is marked with (2) and the line of detachment moving from there to the change in slope of the curling shape, is marked with (2). Figure adapted from Honsali [2018].

Figure 16: Figures representing the failure behavior shown in Figure 15 in displacement-pad position graph. The imposed displacement Δ' is varied from 0 to failure displacement ax the y-axis goes up and the pad length is varied over the x-axis. I.e. the consecutive states of the pad during the increase of imposed displacement are joined vertically upwards. Figures adapted from Honsali [2018].

4 Model Solution Strategy

4.1 State of the Art

4.1.1 Cohesive Elements

As the need for a numerical study investigating the propagation of stick-slip and its potential benefits became apparent in the introduction, this study will propose a parametric finite element model that incorporates reversibility for this purpose. The reversibility will be modeled as a surface element fully recovering upon contact, even at a reattachment location different from the initial one.

While continuum mechanics problems can sometimes be treated analytically, this becomes excruciatingly more difficult or impossible as non-linearities in the mechanical behavior appear [de Borst and Verhoorsel, 2017, Ingraffea and de Borst, 2017]. One of the non-linearities that we specifically want to investigate, is the behavior of adhesives from the moment it reaches detachment at one point until it reaches detachment over the full pad length. As noted before, theoretical studies are often limited to linear mechanics for failure initiation before failure propagation [Cohen et al., 2018], or to the moment past full development of failure, after failure propagation [Ponce et al., 2015]. Propagation of this failure is however critical. Thus, to study this, numerical finite element simulations are necessary, where non-linearities can be numerically solved in the instance where this is analytically not possible anymore.

Cohesive elements are often used to model failure in finite element simulations. Cracks are associated with stress concentrations and thus singularities. Furthermore, numerical methods for continuum damage equations suffer from pathological mesh dependency when softening laws are considered which leads to convergence towards physically unacceptable solutions upon mesh refinement. Cohesive elements allow to represent displacement continuities at boundaries of elements, by lumping cracking on one surface and representing a crack process zone. By placing a displacement discontinuity over this crack process zone, the singularity is relieved. Additional zero thickness line (for two-dimensional simulations) or surface (for three-dimensional simulations) elements are inserted between two normal bulk finite elements where the crack grows. In the case of a large fracture process zone (the zone ahead of the crack tip where damage develops through micro-cracks), there is softening of the material happening in front of the crack tip. The cohesive zone model is especially interesting for this case, since it relates traction over its line or surface to the relative opening of the two sides of the crack displacement discontinuity. A characteristic of this crack model, is that the crack growth path is limited to the element boundaries [de Borst and Verhoorsel, 2017, Ingraffea and de Borst, 2017].

The reason to suggest a cohesive zone model for the surface adhesion properties of soft, dry adhesives is thus apparent. We are dealing with the cracking of a bond between elements for which we know the crack path in advance, since the bonds between adhesive and surface (Van Der Waals Forces [Autumn et al., 2002]) are a lot weaker than the chemical bonds in the material itself. Although some very soft adhesive fail in their bulk material (often with the formation of fibrils) [Williams and Kauzlarich, 2008, Zhang and Wang, 2009, Piau et al., 2005, Lengyel et al., 2016, Creton and Ciccotti, 2016], we will exclude bulk failure adhesive materials in this study. Secondly, we suspect bond softening past the ultimate critical stress state, as would be the case for most materials and has been observed for example in glue-type adhesives [Serrano, 2001] and in PUR-steel adhesive coatings [Zhu et al., 2009]. Finally, the linear stress opening relationship proposed in theoretical models by Cohen et al. [2018], Liu et al. [2019] bears great resemblance to the traction-displacement based element formulation used in the cohesive zone formulation.

Cohesive elements have also been commonly used in the past for modeling adhesive-like materials and even soft adhesives: for adhesives glues in bonded joints [Ramalho et al., 2020, Sarrado et al., 2016, He, 2011], for delamination processes [Tabiei and Zhang, 2018, Girão Coelho, 2016], for coating adhesion to bulk materials [Wang et al., 2016, Zhu et al., 2015, Borino and Parrinello, 2019], for peel tests of a thin strip [Peng et al., 2019, Garg and Datla, 2019, Thouless and Yang, 2008], and for soft adhesives [Zhang and Wang, 2009, Mergel et al., 2020, Biel and Stigh, 2017, Rahulkumar et al., 2000, Jagota et al., 2000, Wei, 2004].

The cohesive zone model proposes a traction-separation law to deal with failure. This model links the traction along the cohesive surface to the relative opening of its two sides. The cohesive surface initially has a zero thickness and will then be allowed to open while applying traction to the surrounding bulk elements. Intrinsic cohesive elements, i.e. elements with an initial elastic phase, are inserted at the beginning of the simulation and start with zero opening and zero traction. They show subsequently an increase (initial elastic phase) and decrease (secondary softening phase) in traction while the opening increases. Extrinsic cohesive elements are elements that are inserted once the stress threshold is reached at a surface and do not open before that: they do not exhibit any elastic behavior. Once the cohesive element is inserted, the transmitted traction only decreases. Thus, both types of elements have a softening behavior, but only the intrinsic elements include an initial linear elastic phase [Park and Paulino, 2013, Elices et al., 2002]. We will focus here on the use of intrinsic elements, as the literature review of adhesives suggests an initial compliance of the adhesive surface exists [Cohen et al., 2018].

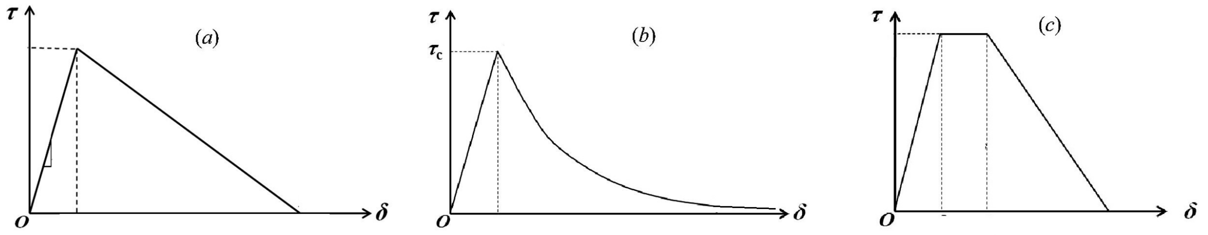

Figure 17: Different possible shapes used for intrinsic cohesive elements, adapted from Heidari-Rarani and Ghasemi [2017]. The traction is shown on the y-axes and the opening on the x-axes. As all are intrinsic, an initial linear elastic phase is included. Figure (a), (b) and (c) then respectively show the linear, exponential, and trapezoidal softening shape.

Multiple shapes of the softening law have been presented such as an exponential, a trapezoidal, or a triangular traction-separation relationship (the latter called linear softening) [Park and Paulino, 2013, Campilho et al., 2013, Volokh, 2004]. Figure 17 shows some of the possible intrinsic traction-separation laws. As all the shapes are intrinsic, after reaching the maximal stress capacity at the end of the linear phase, an initial opening already exists. The softening of the element, where the stress decreases while opening increases is shown for the linear (a), exponential (b) or trapezoidal (c) shapes. Research into the importance of the shape is still continued, and while for brittle elements it has been found that the most important quantities are the area of fracture energy under the curve and the maximal failure load [de Borst and Verhoorsel, 2017, Ingraffea and de Borst, 2017], for soft adhesive surface properties this has been contested [Zhang et al., 2018, Campilho et al., 2013, Fernández-Cañadas et al., 2016]. In the context of soft adhesive, alternative shapes like an exponential increase and linear decay of traction have been proposed as well [Anyfantis and Tsouvalis, 2012].

Other research areas still in progress include the mixed-mode and the frictional coupled behavior of the cohesive elements. The general cohesive law was designed for single-mode (mode I or mode II) failure, but failure generally occurs in a mixed-mode setting and moreover, the cohesive energy differs in mode I and mode II. In addition, during the failure of an element in the mode II direction, contact in the mode I direction can occur and friction should thus occur as well. Multiple approaches have been proposed to deal with these complexities [Park et al., 2009, McGarry et al., 2014, Dimitri et al., 2015, Venzal et al., 2020, Sauer, 2013].

In the current study, we will use the intrinsic version of the Snozzi-Molinari adaptation [Snozzi and Molinari, 2013] of the Camacho-Ortiz [Camacho and Ortiz, 1996] and Ortiz-Pandolfi [Ortiz and Pandolfi, 1999] linear cohesive law. This law addresses the above-mentioned problems fairly well and is already implemented in the dynamic, parallel, open-source framework Akantu [Richart and Molinari, 2015, Vocialta et al., 2016].

The following section where this cohesive law is described, including the relationships, is largely reproduced from [Snozzi and Molinari, 2013, Richart and Molinari, 2015, Vocialta et al., 2016, Richart, 2016] to set the background for the use in this work. The traction-separation relation with all the relevant properties marked is shown in Figure 18. The cohesive law consists of an initial elastic phase with a stiffness k where the traction increases linearly with opening δ until the peak stress σ_c, corresponding to the failure initiation opening δ_0, followed by a linear softening phase where the stress decreases while the opening increases until zero stress and full failure opening δ_c.

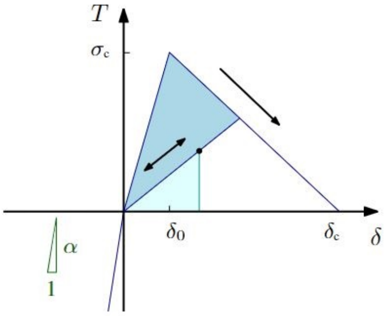

Figure 18: The cohesive law as described by Snozzi and Molinari [2013]. The law is intrinsic: it contains an initial elastic phase and a secondary softening phase. σ_c is the peak stress, δ_0 the failure initiation opening, δ_c the failure completion opening and the area under the curve represents the mode I cohesive energy. The slope of the initial curve is k. The black double arrow shows the unloading and reloading path: as soon as softening occurs, the damage is irreversible and the new peak stress is lower. Figure from [Richart, 2016].

Damage in the cohesive zone is defined by a damage parameter D that varies linearly between 0 and 1 as the opening varies between δ_0 and δ_c. As soon as damage occurs in usual cohesive laws, this is mechanically irreversible. The unloading and reloading path is a new linear path between the stress at the maximal encountered opening so far δ_{max} and the origin, as also shown in Figure 18 by the black double arrow which shows the unloading and reloading path.

$$D = \max\left(\frac{\delta - \delta_0}{\delta_c - \delta_0}, D_{history}\right) \quad \in [0,1] \qquad \text{with } \delta_{max} = \delta_0 + D(\delta_c - \delta_0) \tag{5}$$

The traction T_1 during the initial linear elastic part, and T_2 during the secondary softening phase are:

$$T_1 = \frac{\sigma_c}{\delta_{max}}\left(1 - \frac{\delta_{max}}{\delta_c}\right) \qquad \text{for } 0 < \delta < \delta_{max} \tag{6a}$$

$$T_2 = \frac{\sigma_c}{\delta - \delta_0}\left(1 - \frac{\delta - \delta_0}{\delta_c - \delta_0}\right) \qquad \text{for } \delta_{max} < \delta < \delta_c \tag{6b}$$

The cohesive energy G_c is the integral of the cohesive law:

$$G_c = \frac{\delta_c \sigma_c}{2} \tag{7}$$

In this law the effective opening of the initial-zero-thickness cohesive element δ is described as a function of the normal and tangential components of the separation or relative displacement Δ_n and Δ_t of the element over the surface. The tangential direction is parallel to the surface, corresponding to mode II failure and the normal direction is perpendicular to the surface, corresponding to mode I fracture. This effective opening reads as

$$\delta = \sqrt{\frac{\beta^2}{\kappa^2}\Delta_t^2 + \Delta_n^2} \qquad \text{if } \Delta_n > 0 \tag{8}$$

Where $\kappa = G_{c,II}/G_{c,I}$ is the ratio between the cohesive energies in mode II and mode I failure, and β is a coupling parameter between the normal and tangential displacements. In the remainder of this work, β will be assumed equal to 1. All the cohesive law parameters are then expressed in mode I, and the mode II cohesive law is derived from the mode I parameters, based on the κ parameter. Only the opening Δ_t axis will be scaled, the traction T axis is left unscaled, thus $\delta_{0,t}$, $\delta_{c,t}$, and k_t are scaled and σ_c is left unscaled. Note the underlying assumption of mode I and mode II maximal stress being equal.

$$\delta_{0,t} = \kappa \cdot \delta_0 \qquad \delta_{c,t} = \kappa \cdot \delta_c \qquad k_t = \kappa \cdot k \tag{9}$$

The mixed-mode cohesive law based on mode I law and parameter κ, as in the Snozzi-Molinari law is shown in Figure 19.

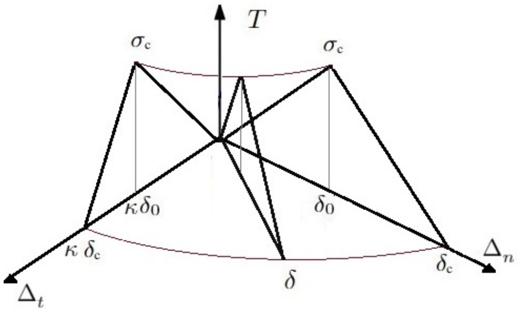

Figure 19: Mixed-mode cohesive law shape based on cohesive parameters failure initiation opening δ_0, full failure opening δ_c, maximal cohesive force σ_c and mode II scaling parameter $\kappa = G_{c,II}/G_{c,I}$. On the y-axis is traction T is shown, on the two other axes the normal opening perpendicular to the cohesive surface element Δ_n and the tangential opening parallel to the cohesive surface element Δ_t. The (T, Δ_n) plane shows the mode I cohesive law and the (T, Δ_t) plane the mode II cohesive law. In the middle, mixed-mode failure is shown with opening δ and corresponding cohesive law based on the mode I and mode II law. Figure inspired by Khoramishad et al. [2016].

Using the paramater κ, this traction allows recovering the tangential and normal components T_t and T_n according to:

$$T_n = \Delta_n T \quad \text{if } \Delta_n < 0 \tag{10}$$

$$T_t = \frac{\Delta_t}{\kappa} T \tag{11}$$

Further, a contact penalty is included in the model and implemented as a decomposition contact response: the interpenetration is dealt with separately first, and the effective opening is calculated solely based on the tangential opening:

$$\text{if } \Delta_n < 0 : \qquad T_n = \alpha \Delta_n \quad \wedge \quad \delta = \Delta_t \tag{12}$$

With α the interpenetration penalty stiffness.

These cohesive elements do not include any healing or reattachment. Although healing of fractured surfaces is common in biological systems, in engineered self-healing polymers, composites or coatings, its inclusion in cohesive zone models is still under development. Physically, the healing can be induced by physical conditions such as pressure, temperature, or light, by chemical transformation of the material upon cracking, by releasing additives or by biological growth [Hager, 2017]. Note that the material properties in this context are not always recovered in the same chemical way after healing. However, in the case of the soft dry adhesives, properties are exactly similar initially and after reattachment. In both cases, the adhesive gets attached to the substrate with Van Der Waals bonds upon contact between both.

Continuum damage models have been proposed to model healing and have been successfully implemented into finite element analysis using different fracture methods including discrete element methods and meshfree methods [Oucif and Mauludin, 2018, Javierre, 2019]. Recent advances on continuum damage models include for example chemico-mechanical coupling [Sanz-Herrera et al., 2019, Jefferson, Anthony et al., 2019, Roldán et al., 2019, Ozaki et al., 2016], thermodynamic healing [Alsheghri and Al-Rub, 2015, 2016] and inclusion of biologically known variables [He et al., 2019b]. These models allow broken elements to reverse damage. Another category of studies uses cohesive elements as a model for the insertion of a different material into a damaged crack. These include the behavior of curing agents released into micro-cracks from encapsulated units in the material [Maiti and Geubelle, 2006, Krishnasamy et al., 2018, Mauludin et al., 2018, Xue et al., 2019], other crack filling healing agents [Ponnusami et al., 2018, Zhang and Zhuang, 2018] as well as the resulting forces from fibers in cracks in fiber-reinforced composites [Karimi et al., 2019]. These do not actually allow damage to be reversed, rather in between a damaged surface, new elements are inserted to represent a different material inserted for healing.

In this study, we will not use one of the unified approaches to healing, rather we will adapt an existing formulation, the adaptation of the Ortiz-Pandolfi law in Akantu, to allow full recovery of cohesive energy upon contact (zero normal opening) at a different location (different tangential opening).

4.1.2 Energy in the Cohesive Zone

Following the irreversibility of the classical cohesive law, the energy $E_{coh,diss}$ is dissipated during the damage of a cohesive element: the energy above the unloading-reloading path cannot be recovered anymore (Figure 18 dark blue area). The energy under the unloading curve is elastic cohesive energy $E_{coh,el}$, and can still be recovered (Figure 18 light blue area). These energies can be expressed in function of the damage and the current normalized opening δ in the case of pure mode I failure.

$$E_{coh,el}(\delta, D) = \frac{(1-D)\sigma_c \delta^2}{2(\delta_0 + D(\delta_c - \delta_0))} \qquad E_{coh,diss}(D) = \frac{D\sigma_c}{2}(\delta_0 + D(\delta_c - \delta_0)) \tag{13}$$

For mixed-mode failure with a factor $\kappa \neq 1$, the exact failure path during damaging needs to be known, as a variation in the Δ_t/Δ_n ratio results in a different cohesive energy. Assuming a constant ratio $\phi = \Delta_t/\Delta_n$:

$$A = \frac{\sqrt{1+\phi^2}}{\sqrt{1+\phi^2/\kappa^2}} \qquad E_{coh,el}(\delta, D, \phi) = A \cdot E_{coh,el}(\delta, D) \tag{14a}$$

$$E_{coh,diss}(D, \phi) = A \cdot E_{coh,diss}(D) \tag{14b}$$

To calculate the cohesive dissipated and elastic energy over a mixed-mode loading path with different ratios ϕ along the path with N steps, where the index i designates the current step, it suffices to sum over the path and make a linear interpolation between values of $A(\phi)$.

$$E_{coh,el} = \sum^{N} (E_{coh,el}(\delta_i, D_i) - E_{coh,el}(\delta_{i-1}, D_{i-1})) \frac{A(\phi_i) + A(\phi_{i-1})}{2} \tag{15a}$$

$$E_{coh,diss} = \sum^{N} (E_{coh,diss}(\delta_i, D_i) - E_{coh,diss}(\delta_{i-1}, D_{i-1})) \frac{A(\phi_i) + A(\phi_{i-1})}{2} \tag{15b}$$

During the occurrence of interpenetration forces, Δ_n is assumed zero for the calculation of the energy. The indentation energy is elastic and due to the orders of magnitude difference with k, negligible.

4.1.3 Stability and Convergence of the Dynamic Solution Procedure

When considering non-linear problems, a finite element simulation can be solved using an implicit static, an explicit dynamic, or an implicit dynamic finite element solver [Richart and Molinari, 2015, Vocialta et al., 2016]. A static model considers an equilibrium situation with zero velocity and zero acceleration: the solver executes Newton-Rapson iterations until equilibrium between internal and external forces is found. A dynamic solver considers acceleration and velocity as well. It can also be solved iteratively with an implicit solution procedure or in a single operation with an explicit solution procedure. The exact solution procedure used in the Akantu framework is detailed in Appendix B.1.

The explicit dynamic procedure, deploying a central difference integration scheme is conditionally stable. Stability refers to the procedure's ability to reduce numerical errors while moving over the timestep. In other words, a lack of stability will cause numerical errors to accumulate over the time steps. The time step used for the integration needs to be smaller than twice the natural period of the whole system, which is approximated by the maximal natural period of the individual elements. This maximal time step is thus approximated by using the natural period of the smallest element [Mitchell and Griffiths, 1980, Richart, 2016].

$$\Delta T_{crit} = 2T_{nat} \approx \frac{\Delta x}{c} \approx \frac{\Delta x}{\sqrt{E/\rho}} \tag{16}$$

In this equation Δx is the smallest in-radius of an element and c is the celerity of the fastest wave speed, or the push-wave speed, which is equal to $\sqrt{E/\rho}$, with E the Young's modulus and ρ the mass density of the elastic material. Currently, there exist no reliable approximations to evaluate the critical time step for a cohesive element. Therefore, the one for the linear elastic material is typically taken as a first approximation.

While unconditionally stable implicit dynamic integration schemes are available, in highly non-linear systems the iterative algorithm often fails to converge. Explicit schemes do not suffer from this, as no iterations are executed and every new time step is calculated directly from the last time step. Any residual unbalance between internal and external forces, is compensated by the velocity and acceleration terms. In addition, the lack of iterations decreases computational cost at every time step. Yet, dynamic solutions can be more computationally expensive if they require small time steps (such as is the case for soft materials) [Mitchell and Griffiths, 1980].

4.1.4 Challenges in Soft Adhesives Surface Modeling

Using a finite element modeling for soft adhesive surface adhesion has two inherent challenges: the numerical challenges in modeling soft materials and the high variability in the physical behavior of the material.

The high computational cost associated with modeling adhesives or soft material failure in general has been widely documented. Specifically, it has been suggested that the crack process zone at the failure front would be of the size of several μm [Knauss, 2015] and therefore the mesh size would need to be unreasonably small. Sauer [2011b] developed an adapted FEM formulation to deal with this small process zone. However, Guo [2019] argues that this is the size of the length of the dissipation zone during which cracks actually develop and the material detaches (i.e. this is the moment of actual detachment around $D = 1$). To represent the behavior around the real failure events, rate-dependent material laws would be necessary as the actual crack process zone depends on crack speed. Rather, it is suggested the cohesive law is still a good way to represent detachment of soft materials from rigid substrates, but its interpretation is different. It represents the yielding phase of the attached surface and not a physical damage development phase. The length scale associated with the yielding is not rate-dependent and is of a more reasonable scale [Guo, 2019].

The physical properties of soft adhesives are especially variable. For a common soft adhesive, PDMS, the Young's modulus can vary between several kPa to several MPa [Raayai-Ardakani et al., 2019]. Equally uncertain are the surface properties: experimental literature values for PDMS-glass adhesion show a variability, ranging from 0.01 J/m^2 to values of 10 J/m^2 of surface adhesion energies [Collino et al., 2014, Galliano et al., 2003, Sofla et al., 2010]. Surface strengths are even more sparsely reported. While part of this variability can be attributed to the uncertainty and variability of the testing methods, the properties of soft materials are also very production-dependent. Exact mixing ratio of the components, curing temperature, curing time, air humidity, all contribute to the ultimate development of bonds between polymer chains in PDMS [Cho et al., 1998, Zosel, 1991, Creton and Ciccotti, 2016].

4.2 Implementation of Reversible Cohesive Elements

As mentioned in Section 1.2, modeling reattachment of the adhesive and sliding is of paramount importance for accurately describing the full behavior of the system. Figures 7 show the importance of the stick-slip behavior on the experimentally obtained force-displacement graphs. Moreover, it has to be taken into account that this reattachment does not happen at the same location as a result of the adhesive layer deformation.

A cohesive element between two T3 elements links them along a line element that opens. However, an element simply allowing full recovery is insufficient as reattachment occurs at a different location. The elements get back into contact at a different location and recover full pulling strength there. Reattachment between different elements than originally would need to be included and this would be computationally very costly. Instead, an approach will be adapted where the original cohesive elements will be allowed to recover, with a correction for the new cohesive reattachment locations implemented in the cohesive law. In this case, the forces acting on the soft adhesive layer side of the cohesive element will be correctly positioned. This will not be the case for the substrate side, but as it is not allowed to deform, the forces acting on it are of no importance here.

In Figure 20 (a), the initial (I), failure (II), and reattachment (III) of a cohesive element between two bulk elements are shown. In terms of the cohesive law, what happens after reattachment at a different location comes down to the moving of the (T, Δ_n) plane over the Δ_t axis with a distance $\Delta_{t,0}$ that is the distance between the original location of the detached element and the new location, as shown in Figure 20 b. Reattachment events can happen multiple times, it is sufficient to declare a different $\Delta_{t,0}$ value.

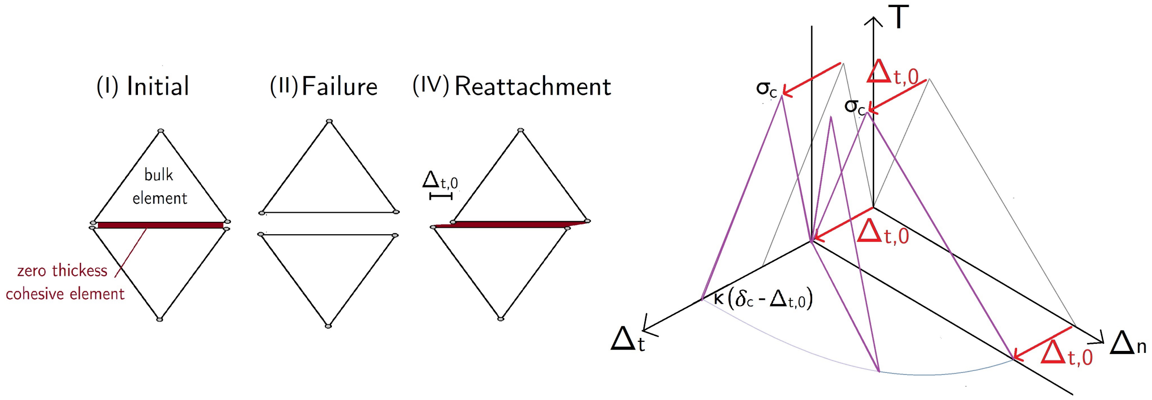

Figure 20: In Figure a, the geometrical configuration of failure of a cohesive element (II) and reattachment at a different location (III) is shown. Figure b shows the cohesive law corresponding to this reattachment: the (T, Δ_n) plane is moved over the Δ_t axis with a distance $\Delta_{t,0}$ that corresponds to the difference between the initial location of attachment (Figure I) and the reattachment location (Figure III).

The Snozzi-Molinari adaptation of the cohesive law including friction and described in Section 4.1.1 is adapted for this purpose. In the case of a damaged element subjected to a normal opening smaller than zero, i.e. the interface is in contact after having been broken, the full cohesive energy is recovered at the new tangential location $\Delta_{t,0}$ and the damage is set back to 0.

$$\text{if } D = 1 \;\; \& \;\; \Delta_n \leq 0 : D = 0 \quad \Delta_{t,0} = \Delta_t \tag{17a}$$

The expression for D, T_1, T_2 and T_n given in Section 4.1.1 remain the same and the expressions for δ and T_t are adapted.

$$\delta = \sqrt{\frac{\beta^2}{\kappa^2}\Delta_n^2 + (\Delta_t - \Delta_{t,0})^2} \qquad \text{if } \Delta_n > 0 \tag{18a}$$

$$\delta = \Delta_t - \Delta_{t,0} \qquad \text{if } \Delta_n < 0 \tag{18b}$$

$$T_t = \frac{\Delta_t - \Delta_{t,0}}{\kappa} T \tag{18c}$$

This adaptation of the cohesive law was validated and found to exhibit the same behavior before and after reattachment in both static and dynamic simulations as desired. The full validation test description can be found in Appendix B.2. This adaptation allows, when the focus is not set on the behavior of the substrate adapting any cohesive law with a rather limited intervention in the code to model sliding or stick-slip behavior. It can be directly extended to a three-dimensional simulation by replacing δ_t and $\Delta_{t,0}$ with a vector in the plane of the zero-thickness cohesive surface element.

4.3 Finite Element Model

A two-dimensional plane strain finite element model is developed to investigate the response of the system.

Bulk Material and Poisson's ratio. For the bulk material, first-order T3 elements (linear interpolation) are used because of their simplicity and advantage in computational time. General soft polymers are nearly incompressible and have a Poisson's ratio close to 0.5 [Müller et al., 2019]. In standard Finite Element Analysis, incompressible laws are accompanied with volumetric locking where a too stiff response is observed, due to interpolation errors. This is linked to the fact that the bulk modulus $K = \frac{E}{3(1-2v)}$ tends to infinity as the Poisson's ratio goes to 0.5. Adapted formulations with independent interpolations exist to deal with this (see for example [Dolbow and Belytschko, 1999, Hung et al., 2009, Coombs et al., 2018]), but here we will use an approximation of the Poisson's ratio of 0.45, avoiding these problems.

Adhesive surface representation. The adhesive surface is represented with intrinsic bilinear zero-thickness cohesive elements (linear interpolation). As discussed in the introduction, this law is especially interesting for the case of soft adhesive surfaces as an initial bond stiffness is included by an initial elastic phase. Furthermore, after full failure opening δ_c, the force transferred between the substrate surface and the adhesive material vanishes, as would be the case in reality. The cohesive law is however adapted to allow the adhesive surface to reattach at a different location on the substrate, as explained previously in Section 4.2. As previously shown in the introduction, modeling sliding and stick-slip is crucial in zero-degree peeling tests.

Substrate material. Under the adhesive surface, a substrate material is included that is modeled as a linear elastic material in order to ensure proper boundary conditions. The full block is clamped at every node and its elastic modulus thereby has no effect in this case. It can be chosen close to the elastic modulus of the backing or adhesive, thereby reducing computational cost: as explained in Section 4.1.3 a lower Young's modulus allows increasing the dynamic time step thereby reducing the number of steps that need to be calculated. This is a realistic assumption as glass has a stiffness 6 orders of magnitude higher than PDMS, a common soft adhesive. While in reality the properties of this surface (roughness) are important for the adhesive behavior as a while, they actually influence the adhesive surface only. The properties of this adhesive surface itself are essentially dependant on the surface of attachment, and the effect of roughness could be modeled by adapting the law used for the cohesive elements.

Execution of the pulling. The pulling is driven in the solution procedure by moving the right edge of the backing parallel to the substrate, while not allowing it to deform or move in the direction perpendicular to the substrate. Both the X and Y displacement components of this edge are thus prescribed, with a vanishing Y displacement and an increasing horizontal imposed displacement.

Solver and mesh generator. The simulation is solved in an open-source multi-core finite element solver, Akantu [Richart and Molinari, 2015, Vocialta et al., 2016]. This framework is specifically designed for parallel high-performance computations and includes the Snozzi-Molinari adaptation of the Camacho-Ortiz cohesive elements. The code uses a modified Newton-Raphson procedure to solve the discretized governing equations[Richart, 2016]. The dynamic solution procedure is based on a Newmark-Beta time discretization, with as default setting the central difference procedure, an explicit integration scheme [Richart, 2016]. Further details on this procedure are provided in Appendix B.1. The mesh is generated using the open-source mesh-generation software Gmsh [Geuzaine and Remacle, 2009] and visual post-processing is achieved using the open-source visualization application ParaView [Ahrens et al., 2005, Ayachit, 2015] and a Jupyter notebook.

4.4 Solution Procedure

Solving the system presented above causes both convergence issues in the static solution procedure and a low critical timestep in the dynamic solution procedure. The convergence issues in the static solution procedure are caused by the non-linearities inherent to the system.

- The first source of non-linearities is the neo-hookean material law. To resolve this, the loading (prescribed as displacement) is imposed incrementally in the static solution procedure.
- Secondly, the cohesive bilinear law used as discussed in Section 4.1.1 and Figure 18, shows discontinuities. In particular, the strong stress redistribution associated with the softening part of the cohesive law and the discontinuity between the softening and full failure region cause numerical challenges. At this discontinuity, any further opening or closing (before reattachment) is not linked to any traction, the surfaces that were normally connected with this element become free, which may cause instabilities and numerical convergence issues. For this reason, starting from the moment that one cohesive element fully fails, a dynamic solution procedure is used.

The dynamic solution procedure requires at low pulling speeds a high amount of steps to be implemented until failure of the pad as the critical time step is very low.[1] Therefore as long as possible, a static solution procedure with incremental displacements is preferred. The simulation is started as a static one with incremental small displacements of the right end of the backing. As soon as one element has advanced far enough in the softening region, the dynamic part of the simulation is initiated. For this purpose, a script communicating this condition between all cores after each time step is added to Akantu. The model then continues further dynamically. Note that we are interested in the quasi-static response of the pad, and a dynamic solution procedure is applied here for numerical purposes only.

---

[1] Using formula (16) and a cohesive element length of 0.1 mm, the Young's modulus and mass density respectively 100 kPa and 1000 $kg/m3$, the critical time step is approximately 10 μs.

As such, the mass densities of the backing and the adhesive will be included in the model in inertia terms. 1000 kg/m^3 is used, since this is an average value for soft adhesives such as for example PDMS. Note that their effect on the quasi-static behavior can be neglected and is included for numerical purposes only.

Upon switching to the dynamic solution procedure, a velocity v is imposed. This velocity v will be expressed as a non-dimensional value v' as well.

$$v' = \frac{\mathsf{v}}{\sqrt{E/\rho}} \tag{19}$$

In experiments such as in Cohen et al. [2018], the loading velocity is typically taken as the pad thickness per minute. We choose here a velocity five times larger as this speeds up the simulation significantly, while this loading velocity leads to marginal loading rate effects. The reader is referred to Appendix C.5 for the result of the sensitivity tests demonstrating this. The velocity is applied gradually. If we would impose the velocity immediately in one single timestep ΔT, a very high destabilizing acceleration of $2v/\Delta T$ would be imposed. Rather, a triangular acceleration profile is imposed over a time of 100 μs. This is incorporated in the solution procedure by varying the additional displacement imposed at every time step.

4.5 Quasi-static Behavior Enforcement

Although the nature of the system requires the use of a dynamic solution procedure to be solved, we actually wish to study the quasi-static response of the pad, ignoring any visco-elastic or other rate-dependent material behavior. Quasi-static loading behavior uniquely was studied because of the observed high-speed dynamic events related to the breaking of elements under certain parameter combinations (specifically low cohesive energy relative to the pad elastic deformation energy). The very sudden stress redistributions after the cohesive element failure, cause high-speed dynamic waves. These high-speed dynamics would lead to convergence failure even with very small time steps. To avoid such convergence issues, we choose to implement damping, filtering out high-frequency events, and to pause pulling behavior during cohesive element failure. As the cohesive element failure events are not quasi-static equilibrium states, we allow them to rearrange into a quasi-equilibrium state before continuing the simulation.

4.5.1 Damping

Damping is not included in the Akantu framework, but is desired here to damp out any high-frequency oscillations that would require very small time steps. Classically, damping is included in the equations of motion.

$$M\ddot{u} + C\dot{u} + Ku = F_{ext} \tag{20}$$

Where u is the displacement column vector of the nodes, $\ddot{u}$ the acceleration vector, $\dot{u}$ the velocity vector, F_{ext} the vector of applied forces, K is the global stiffness matrix, C the damping matrix and M the lumped mass matrix of the system.[2]

---

[2] There is no difference in notation between matrices and vectors, as the distinction is made in the text.

In the explicit central time difference integration scheme, this would result in the following discretized equations to compute the solution at time $t + \Delta t$ if the state at time t is known:

$$u_{t+\Delta t} = u_t + \Delta t \cdot \dot{u}_t + \frac{\Delta t^2}{2} \cdot \ddot{u}_t \tag{21a}$$

$$\dot{u}_{t+\Delta t}(1 + \frac{C\Delta t}{2M}) = \dot{u}_t + \frac{\Delta t}{2} \cdot \ddot{u}_t + \frac{\Delta t}{2M} \cdot (F_{ext,t+\Delta t} - Ku_{t+\Delta t}) \tag{21b}$$

$$\ddot{u}_{t+\Delta t} = \frac{1}{M}(F_{ext,t+\Delta t} - Ku_{t+\Delta t} - C\dot{u}_{t+\Delta t}) \tag{21c}$$

Since damping is not implemented in Akantu, it will be included in the simulation in a two-step procedure: the equation of motion is first solved as if $C = 0$, and a correction factor is subsequently applied on the velocity.

$$M\ddot{u} + Ku = F_{ext} \quad \text{and calculate } \dot{u}^{pred} \tag{22a}$$

$$\dot{u} = \alpha \cdot \dot{u}^{pred} \quad \text{with } \alpha < 1 \tag{22b}$$

Equations (21) in this case become:

$$u_{t+\Delta t} = u_t + \Delta t \cdot \dot{u}_t + \frac{\Delta t^2}{2} \cdot \ddot{u}_t \tag{23a}$$

$$\dot{u}_{t+\Delta t} \cdot \frac{1}{\alpha} = \dot{u}_t + \frac{\Delta t}{2} \cdot \ddot{u}_t + \frac{\Delta t}{2M} \cdot (F_{ext,t+\Delta t} - Ku_{t+\Delta t}) \tag{23b}$$

$$\ddot{u}_{t+\Delta t} = \frac{1}{M}(F_{ext,t+\Delta t} - Ku_{t+\Delta t}) \tag{23c}$$

While an equivalence of equations (21b) and (23b) is obtained if $\frac{1}{\alpha} = (1 + \frac{C\Delta t}{2M})$, it should be pointed out that the effect on the acceleration is not the same as the conventional introduction of a separate damping term. Rather, the damping of the velocity will influence the next position, which will in turn affect the acceleration. While the implementation causes subtle differences between both procedures, both take out higher frequency energy with the frequency determined by the amount of damping, and allow studying slower phenomena at a lower computational cost.

To ensure time step independence of the factor α, a material property $t_{damp1\%}$ is defined as the time in which the velocity is damped by 1%, and α is calculated from $t_{damp1\%}$ and the time step used in the simulation Δt.

$$\alpha = (0.99)^{t_{damp1\%}/\Delta t} \tag{24}$$

Similar to the non-dimensionalization introduced in equations (3), this coefficient will be transformed into a non-dimensional one: the ratio of the natural period of an element over the 1% damping time.

$$T_{damp} = \frac{L/t_{damp1\%}}{\sqrt{E/\rho}} \tag{25}$$

In this formula, L will be approximated by the cohesive element length.

A basic pure tension pulling and release simulation is done on a material block to study the oscillations occurring at release obtained for different amounts of damping. It is found that a value for $t_{damp1\%}$ of 1-10 μs provides a good trade-off between not enough and too much damping. This will be used as an initial estimate for the damping time and during the execution of the adhesive pad simulations, this will be further corrected where necessary. For details on this test, refer to Appendix B.3.

4.5.2 Snap-Through

During the modeling of the detachment phase of the adhesive, we observe phases where high-speed dynamics events distort the results. This has been earlier linked to the cohesive zone damage by Guo [2019]. Failure of cohesive elements is caused by the stress distribution around the area of detachment. This failure then allows stress relaxation, at which point the cohesive properties would require a very refined mesh, as discussed in Section 4.1.4. To mediate this, it has been proposed to include rate-dependence, which would allow for a more gradual stress relaxation. However, we opt to study the quasi-static response of the pad instead, we allow any dynamic effects related to the damage of cohesive elements to develop while holding the pad at the same displacement level rather than continuing to pull simultaneously. Only when a new static equilibrium state has been developed using the dynamic solution procedure, the pulling will be resumed. As the cohesive damage propagation is a dynamic phenomenon that takes place over a short timescale, and we wish to study quasi-static phenomena, ignoring these events is reasonable. The recovery of a static state is detected by a code that allows communication between the different cores executing the simulation, and that detects whether new elements have been broken. When resuming the enforcing of displacement increments, the increase in displacement again needs to be applied gradually, with the same triangular acceleration profile as before. The procedure is continued until 95% of the adhesive surface has failed: a further continuation of the simulation of caused numerical issues. A graphical visualization of this algorithm is included in Appendix B.4.

5 Competing Failure Mechanisms

Three main failure modes for the adhesive pads, one accompanied by stick-slip motions, were observed in the simulation results consistent with experimental observations detailed in Section 3, and are detailed in Section 5.1. The propagation of Schallamach waves accompanying the stick-slip is studied in more detail in a simulation of an infinitely long pad in Section 5.2.

The convergence of the simulations with respect to spatial and time discretization is confirmed in Appendix C.2. For an explanation of mechanics during the infinitesimal linear elastic deformation as reported in Cohen et al. [2018], Appendix C.3 is recommended. Internal force diagrams of the different simulation from Section 5.1 for a more in-depth analysis are provided in Appendix C.4. The initial response of a three-dimensional simulation (that could not be completed due to numerical limitations, as explained in Section 4) is discussed in Appendix C.6.

5.1 Three Main Failure Modes and Stick-Slip Occurrence

Three main failure modes have been experimentally observed (Section 3 and Section 1.2) and are illustrated in Figure 21: curling from the opposite end, steady peeling from the pulling end and interfacial cavitation close to the pulling end. These failure modes are retrieved in the simulations. The first simulation described in Section 5.1.1 initiates by the formation of an interfacial cavitation close to the pulling end that quickly propagates in both directions until the pulling end is detached. Then, the detachment front propagates over the pad in a slower steady peeling motion. This is accompanied by the reattachment, stick-slip movements, observed as well in the experiments. Finally, once the detachment front moves close enough to the opposite end of the pad, a detachment front from that side, curling, propagates rapidly and the full pad fails. A second simulation described in Section 5.1.2 exhibits no interfacial cavitation or steady peeling phase but fails immediately catastrophically with a curling mode. The third simulation described in section 5.1.3 initiates with a curling motion, but is interrupted in its propagation by the sudden detachment of an interfacial cavitation that joins the detachment region. This pad shows catastrophic failure as well and no steady peeling phase.

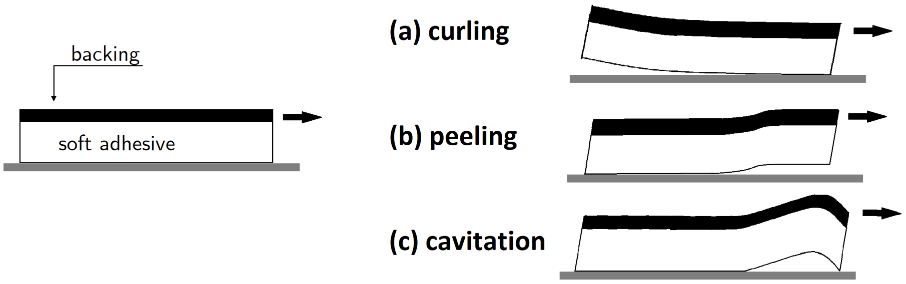

Figure 21: Failure modes of a bi-layer adhesive under a zero-degree adhesive. The Figure on the left is the initial configuration. Figure (a) on the right top shows curling from the opposite end of the pad, Figure (b) shows peeling from the pulling end of the pad while Figure (c) pictures cavitation. Figures inspired by Cohen et al. [2018].

For this simulation, the geometrical parameters L, t and t_b of the simulations are chosen in the same order of magnitude as the experiments described in Cohen et al. [2018]. Bulk properties of the adhesive and backing were chosen among reasonable values for a PDMS sample[3], a commonly used soft adhesive. The linear elastic stiffness of the adhesive surface is chosen of the same order of magnitude as approximations based on fitting to experiments in [Cohen et al., 2018]. For the other surface properties, a high variability of values was found in the literature, as discussed in Section 4.1.4. Due to this uncertainty, the values were chosen for numerical convenience: small enough to allow failure in a reasonable time and large enough to allow convergence. Table 2 details the parameters for the first discussed case of steady peeling in Section 5.1.1, as dimensional parameters with their non-dimensional equivalent. For the pure curling case in Section 5.1.2 and the curling-interfacial cavitation case in Section 5.1.3, the difference in non-dimensional values with the first simulation will then be mentioned.

Geometrical and Bulk Properties					
E	50 kPa	E_b	2 MPa	β	8
t	8 mm	t_b	1.6 mm	α	2
L	120 mm			L/t	15

Surface Properties					
G_c	0.2 J/m^2			θ	0.5 $\times 10^{-3}$
σ_c	1.6 kPa			ζ	32 $\times 10^{-3}$
k	16 $\times 10^6 N/m^3$			γ	2.6
κ	0.4				

Table 2: Parameters used for the interfacial cavitation simulation.

The exact numerical parameter values for each simulation, as well as the values for the simulation of the infinitely long pad, are discussed in Appendix C.1.

---

[3] Note that in ranges of large stiffness, PDMS does not have adhesive properties anymore (or very weak ones).

5.1.1 Interfacial Cavitation Followed by Steady Peeling and Curling

The behavior of the simulation that shows interfacial cavitation, steady peeling, and ultimately curling will be discussed in this section. The parameter values for this simulation were listed in Table 2.

5.1.1.1 Failure Development

Direct correspondence between the failure sequence of this pad in the simulations and the pad in the experiment exhibiting interfacial cavitation is found when comparing Figure 15b with Figure 22. The amount of imposed displacement is increased from Figure (I) to Figure (VI). Note that the perspective in both figures is different: in the experiments, we are looking at the bottom of the pad, while in the simulations we are looking at the vertical cross-section of the pad (see also Figure 14). In Figure 22 the cohesive zone damage is shown on the bottom of the pad at the original region of attachment, the pad deformation is magnified for clarity, and deformations in the Y direction are shaded. Figures (II)-(III) show the development of the interfacial cavity from the pulling end and its transition to a steady peeling mode (it will become clear later when discussing Figure 24 why this interfacial cavitation mode continues into a steady peeling mode). The boundary between the yellow attached elements and red detached elements, where the failure propagates forward, will be called the detachment front. Figure (IV) shows the development of the reattachment region trailing the detachment region (yellow recovered elements that were red in Figure (IV) to the right of the detachment front) and finally figures (V)-(VI) show the curling mode from the opposite end that concludes the failure mechanics when it joins the peeling front.

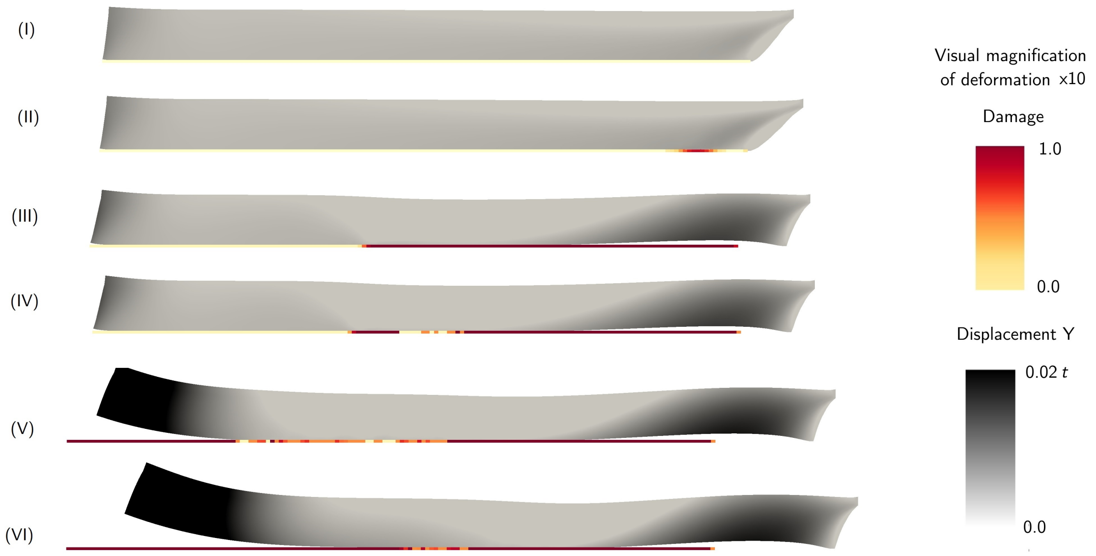

Figure 22: Failure sequence of the simulation with parameter values (β, α, L/t, θ, ζ, γ, κ) = (8, 2, 15, 0.5×10^{-3}, 32×10^{-3}, 2.6, 0.4)that exhibits a sequence of interfacial cavitation, steady peeling, and curling for failure. The imposed displacement is varied from Figure (I) to Figure (VI). At every stage, the (magnified) deformation of the pad is shown, with additional shading for the vertical displacements. On the bottom of the pad, the level of damage of the cohesive zone is shown. In Figure (I) the pad is placed under loading and no damage is observed yet. (II) The first small detachment region, the interfacial cavitation close to the pulling end start developing. (III) Rapid development of the interfacial cavitation continues, and eventually slows down when switching to the steady peeling failure mode. (IV) The detachment propagation front is now closely followed by a region of where reattachment develops. (V) The detachment at the opposite end starts and propagates fast over the pad. (VI) The pad is fully detached. Direct correspondence with Figure 15b is observed.

This pad behavior and the formation of the interfacial cavity can be intuitively understood by looking at the effect the pulling of the stiffer backing has on the pad shape. In the backing, a larger stress will develop than in the soft material, and the soft material will be more restricted in its deformation due to the backing. The internal force distributions resulting from this have a horizontal and vertical gradient, with as a resultant different couples along the pad length, illustrated in Figure 23. The length over which these couples are spread, depends on material properties.

Figure 23: Illustration of the force distribution in the pad that exhibits interfacial cavitation as a failure initiation mode. The pulling of the pad parallel to the substrate combined with the boundary conditions at the adhesive surface creates internal stress distributions with resulting couples in the pad. This results in the formation of the interfacial cavitation.

Note that this is only a simplified interpretation of the stress-state of the pad, with the goal of providing the reader with an intuition on the mechanics and their sensitivity to non-dimensional parameters. The internal force distributions and an in-depth analysis of the mechanical conditions of the pad, are discussed in Appendix C.4. An intuitive understanding of the curling behavior, will be later discussed in Section 5.1.2 and an intuitive understanding of the reattachment behavior in Section 5.2.

5.1.1.2 Surface Opening Profiles

In Figure 24, the same peeling process as in Figure 22 is shown by plotting the normalized vertical displacement at the pad surface (left) and the attached and detached regions (middle) along the length on the layer (x/L) for varying levels of imposed displacement (Δ). On the right, cross-sectional views of the layer at different instances throughout the peeling process as described in Figure 22 are shown.

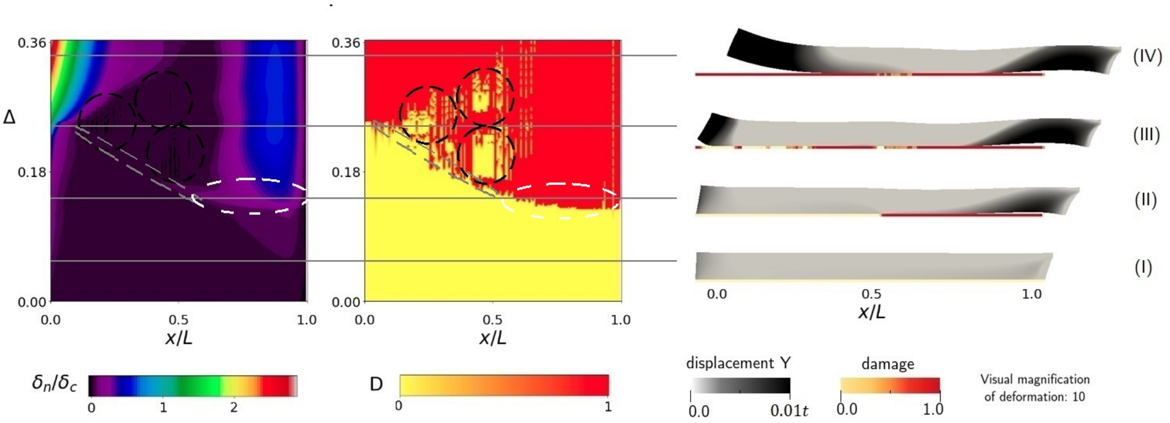

Figure 24: Development of failure for the simulation with parameter values $(\beta, \alpha, L/t, \theta, \zeta, \gamma, \kappa) = (8, 2, 15, 0.5\times10^{-3}, 32\times10^{-3}, 2.6, 0.4)$, that exhibits a sequence of interfacial cavitation, steady peeling, and curling for failure. (left) On the y-axis Δ or the amount of pulling displacement is advanced, and on the x-axes x/L or the pad length is advanced. The consecutive states of the pad are vertically joined over imposed displacements. The color scheme shows the normalized vertical displacement value. (middle) On the y-axis Δ or the amount of pulling displacement is advanced, and on the x-axes x/L or the pad length is advanced. The consecutive states of the pad are vertically joined over imposed displacements. The color scheme shows the advancement of the damage level. The areas on the middle graph that evolve vertically from red (damage) to yellow (no damage), have reattached. (right) The full pad deformation is shown at specific moments during the pulling process. The deformation of the pad is magnified for clarity and vertical deformation is shaded. Below the pad, the surface zone and its evolution of damage is shown. The white dashed lines signify the initial cavity development length, the grey dashed line the steady peeling detachment front, and the black dashes circles the reattachment zones.

First, by comparison of the left and middle figures, it is apparent that the vertical displacement and damage plots are not directly correlated, this will be explained when discussing Figure 25. In Figure 24 (I) the displacement is imposed and it is observed that early in the peeling process vertical displacements localize near the pulling end and at the opposite end. The stress distribution along the pad length, as shown in Figure 23, are responsible for this state. On the left graph, no noticeable amounts of vertical opening at the surface, and on the middle graph, no noticeable amount of damage can be seen for this level of imposed displacement.

Figure (II) shows how, as displacement increases, the region near the pulling end continues to lift off of the substrate until detachment initiates. The vertical lift-off of the interfacial cavitation, can be seen on the left figure as the start of the blue region near the pulling end $x = L$, the region in the white dashed lines. The initiation of detachment can be seen on the middle figure as the red zone. From the initiation, the failure of a certain interfacial cavitation length is almost immediate around the displacement corresponding to image (II) (horizontal boundary between yellow and red region in the middle graph in the white dashed lines). The further damage propagation between stages (II) and (III) shows a more gradual development of the detachment front (diagonal boundary going upwards left between yellow and red region in the grey dashed lines in the middle graph), a steady peeling process. It is in this region that reattachment is also observed. On the middle graph, reattachment can be seen by looking at a vertical line (evolution over time of a determined position on the pad length), and seeing after the first damage (yellow to red), damage disappear (red to yellow). These reattachment events happen multiple times and are localized near the steady peeling front (regions in the black dashed circles). During this steady peeling phase, the vertical lift of the interfacial cavitation remains nearly constant, as seen on the left graph where there is barely any change of color distribution between phase (II) and (III). When looking closely, the only difference is a diagonal line of positive vertical opening going upwards left (in the grey dashed lines), corresponding to the detachment front of the middle figure, and a small region of negative vertical opening (black region on the figure on top of the diagonal line, in the black dashed circles) falling in the reattachment region on the middle graph. As contact is necessary for reattachment, this region is the reattachment front.

Figure (III) shows the development of the curling region at the opposing end: a higher lift-off of the pad from the surface is now achieved there. This happens when the steady peeling front has moved close enough to the opposite end to induce there the stress state necessary for the curling. On the left figure, we can see that the vertical opening at the surface at the opposing end $x = 0$ now quickly increases and continues to increase to become bigger than the interfacial cavitation lift (region above line III). On the middle figure, we can see a horizontal detachment front on the graph (at $x = 0$ for horizontal line III) coinciding with the start of this significant increase in vertical displacement, the propagation of the curling front. Between lines (III) and (IV) on the middle graph, this curling detachment front intersects with the steady peeling front and a diagonal line moving upwards right marks the end of a region of reattachment (mixed red-yellow) and the start of a region of only failure (red), this is the top of the region with black dashed circles. This corresponds on the left graph to a diagonal line upwards right marking the start of a region of positive opening (the boundary between light and dark purple at the top of the region with the black dashed circles). Finally, Figure (IV) shows how full failure of the pad is achieved. The curling movement and the steady peeling movement have joined, the reattachment movements ceased, and the pad is no longer attached. On the left figure, this can be seen as the two regions with positive vertical opening joining: the dark purple region vanishes at the top of the left figure. In the middle figure, the diagonal line marking the end of the reattachment region and corresponding to the curling behavior positive lift-off at the opposite end, marks the end of the reattachment zone in the pad. It can be concluded the propagation of the curling front has stopped the reattachment mechanics created by the propagation of the steady peeling front.

Figure 24 left also shows very good correspondence with the experiment, as seen when comparing it to Figure 16b. The same shape of the curling region at $x = 0$ is observed: it starts lifting at the beginning of the peeling test, but only continues to propagate quickly near the end of the pulling (change of slope of the detachment region). The occurrence of an interfacial cavity near $x = L$ around the middle of the peeling test and its quick development is also observed in both graphs (it starts as almost a horizontal line on the figure in the white dotted lines, i.e. developed during a limited amount of time), but with a nearly constant length afterwards (limited by two vertical lines on the figure, i.e. no evolution of length of this cavity in time). Next, the diagonal line on the opening graph in the grey dotted region is also seen in both figures as a region of higher vertical opening (light purple line in Figure 24 left, light pink line under the left dashed black in Figure 16b).

For an understanding of why the normal opening graph and detachment graph provide little correspondence in Figure 24 left and middle, the tangential opening profile is depicted in Figure 25. This graph shows the normalized horizontal displacement at the pad surface along its length (x/L) for varying imposed levels of displacement (Δ). During the phase of low values of displacement, corresponding to the region before state (II) in Figure 24, virtually no tangential displacement is observed, the graph is black. After that, at the moment corresponding to state (II) (the quick detachment of the interfacial cavitation), the region on the x-axis corresponding to this interfacial cavitation length has almost the same shear displacement (approximately horizontal color lines in Figure 25 on the region between $x/L = 0.6$ and $x/L = 1$). The detached end of the pad is evenly pulled. For the region between $x = 0.1L$ and $x = 0.6L$ where steady peeling has initiated failure, and for the region where initial failure was curling induced near $x = 0$, the shear distributions also follow the pad surface failure line (the pad surface failure lines being the distinction between the black and colored regions in Figure 25 and the distinction between full yellow regions and mixed red/yellow and red regions in Figure 24 middle). This could be seen by the colored lines being parallel to the failure line if reattachment was not shown on the graph. However, since reattachment is included in the graph, as during reattachment the tangential opening gets artificially reset to 0 numerically, these regions show the reattached tangential displacement. We can thus observe reattachment in this figure as well by looking at the regions where the color quantifying the tangential opening is strongly jagged.

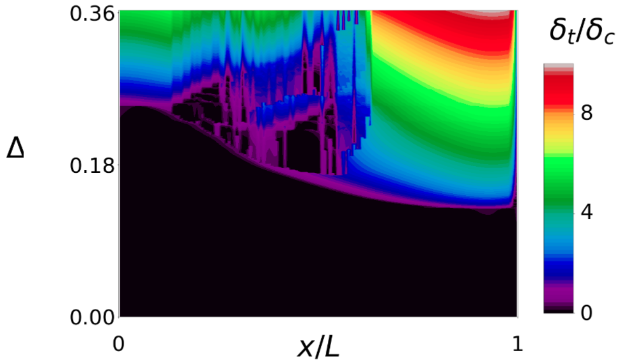

Figure 25: Development of tangential (shear) opening of surface area for the simulation with parameter values (β, α, L/t, θ, ζ, γ, κ) = (8, 2, 15, 0.5$\times10^{-3}$, 32$\times10^{-3}$, 2.6, 0.4), that exhibits a sequence of interfacial cavitation, steady peeling, and curling for failure. On the y-axis Δ or the amount of pulling displacement is advanced, and on the x-axis x/L or the pad length is advanced. In other words, the consecutive states of the tangential opening of the pad are vertically advanced over imposed displacement. The color represents the amount of the tangential displacement. The patterns in the middle show reattachment: during reattachment, the tangential opening gets artificially reset to 0 numerically.

In summary, there is clearly an easy match between the tangential opening figure and the damage graph, while the correspondence between the normal opening graph and the damage graph is less easily readable. It is observed that despite the opposite end vertical opening being higher initially, the difference in tangential opening between pulling end and opposite end causes the interfacial cavity to appear first, rather than to allow curling at the opposite end first. This interfacial cavitation fails almost immediately over a certain length: this is the length where sufficient shear traction has been developed, as can be concluded from the tangential opening profile. Further pulling then causes the steady peeling we observe. Ultimately, once the steady peeling front is close enough to the opposite end to induce sufficient surface shear traction there as well, curling starts. It is concluded that in pads with this failure mechanism, the tangential opening and shear force distribution determine failure, while the normal opening and reattachment is a result of the moments arising because of this shear force, as drawn in Figure 23.

5.1.1.3 Load-Displacement Response

The phenomenology of the failure modes observed experimentally being successfully captured, the load-displacement response will be studied. The graph showing applied force at the pulling end in function of the imposed displacement is shown in Figure 26(left), together with a global fraction of the surface that is detached (right) is plotted in function of the imposed displacement.

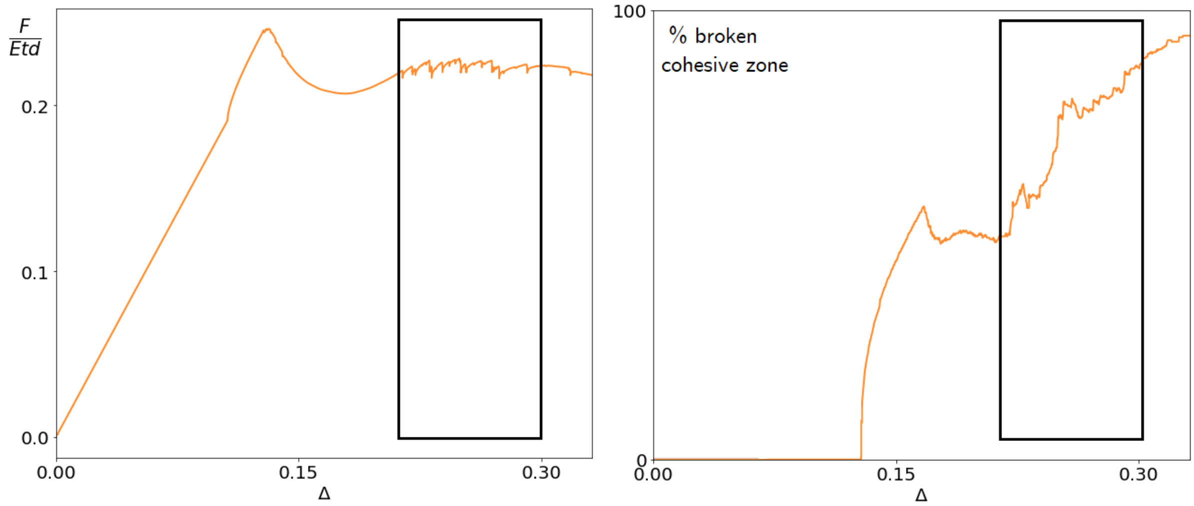

Figure 26: Force-displacement (left) and percentage of failure-displacement (right) graphs for the simulation with parameter values (β, α, L/t, θ, ζ, γ, κ) = (8, 2, 15, 0.5$\times 10^{-3}$, 32$\times 10^{-3}$, 2.6, 0.4)that exhibits a sequence of interfacial cavitation, steady peeling, and curling for failure. (left) The force is the total pulling force in the X-direction that needs to be exerted upon the pulling end of the backing to enforce the amount of displacement imposed and is shown on the y-axis. The amount of displacement imposed is shown on the x-axis. (right) The % of broken length on the cohesive zone or adhesive surface on the y-axis shows the advancement of failure and the instances of reattachment. The amount of displacement imposed is shown on the x-axis. Reattachment is characterized by the broken percentage going down again and stick-slip is recognized by repeated reattachment events that also relate to drops in the force-displacement curve on the right. The region in which stick-slip can be observed is surrounded by a black frame.

In the force-displacement response, a linear elastic phase until peak force and a subsequent softening region can be observed. The discontinuity in the linear elastic region emerges from the switch to a dynamic solution procedure and is thus not physical. In the failure plot, the region that showed a linear force phase shows no detachment, the pad has a high build-up of pre-peak stresses. At peak force, the surface starts detaching smoothly and after this, shows reattachment events. Reattachment can be observed in the figure on the right by the downwards movement of the graph: parts of the surface that were earlier detached (failed) are attached again and not counted anymore in the percentage failure. Further into the detachment, a black frame is drawn around the region that shows subsequent drops and increases in the force-displacement plot and multiple reattachment events in the failure plot: stick-slip is observed. Moreover, the stick-slip behavior shows similarities with the experimental force-displacement curves observed force stick-slip detailed in Section 1.2.

Lastly, when comparing the peak force of approximately $\frac{F}{Etd} = 0.2$ with the experimentally observed peak force in Cohen et al. [2018], detailed in Section 3, of $\frac{F}{Etd} = 0.5$, we find the values to be in the same order of magnitude. It is to be pointed out that the values of the surface properties are very uncertain (Section 4.1.4), over multiple orders of magnitude.

5.1.1.4 Correspondence with Experiments

As discussed in Section 1, the representation of stick-slip behavior for surface-surface interactions (showing local drops in an increasing force-displacement curve, rather than oscillations around a constant value) is a phenomenon that was not earlier captured in finite element simulations. In this simulation, both the phenomenology of the failure mechanics, the occurrence of stick-slip and its link to reattachment was achieved. The close matching of the simulations and the experiments is a strong indicator that our simplified implementation of reattachment is sufficient to approximately capture this phenomenon. Moreover, capturing this phenomenon in simulations, now allows further studying its mechanics, the driving force and the conditions of its occurrence in detail, which would be challenging experimentally.

5.1.1.5 Energy Distribution

The development of a finite element model allows analyzing quantities that we would not have been able to study in experiments, such as the variations and transfers of the energy, depicted in Figure 27 left. The top figure shows the variation of energy (y-axis) over the imposed displacement (x-axis). The dark blue line shows the total energy input by the application of a force, and the red, purple, green and light blue regions show respectively the elastically stored energy in the bulk, cohesive energy that has been dissipated (including this energy multiple times for elements that reattached multiple times), stored cohesive energy, and damped energy. The potential elastic bulk energy, cohesive energy that was dissipated, cohesive energy that is stored, and damped energy are plotted cumulatively. The cohesive energy is calculated for mixed-mode paths, and includes the energy of elements that have failed multiple times. The total energy put into the system by applying a force, is shown with a dark blue line as well.

First, remark the amount of damping energy is rather high. As we are dealing with dynamic solution procedures for a process we wish to study quasi-statically, this high amount of damping signifies the presence of a considerable amount of damped out high-frequency events. This fact could contribute to the not-exact numerical correspondence of the applied force in experiments and simulations. However, for studying quasi-static processes and sequences of events, the high amount of damping is not a limiting factor, especially considering that we pause the loading procedure during the propagation of highly dynamic events.

Regarding the evolution over imposed loading of the energy, only elastic energy is observed in the system until the dynamic solution procedure is started (pure red region before $\Delta = 0.12$). Then, the elastic energy is immediately dissipated into cohesive energy (decrease of the red area, increase of the purple area). Barely any cohesive elastic energy is stored in the system. When increasing the displacement even more, as the stick-slip region starts in the region marked with a black frame, but also at higher displacements and the amount of dissipated energy continues increasing in the region after that, while the elastic energy in the system decreases.

To examine the transfer of energy during the stick-slip phases in more detail, a zoom is made on what happens in the region indicated by the black square in Figure 27 bottom. The left bottom graph shows the amount of reattached length of the surface in function of the displacement (it can be higher than 100% since elements can reattach multiple times). The right bottom graph shows a zoom-in on the energy graph, non-cumulative, also in function of the displacement. The two vertical lines on the graph show the interesting transitions: during the significant increase in the number of reattached elements, the dissipated cohesive energy increases, and both the stored bulk elastic energy and the stored cohesive energy decrease. The reattachment of elements is linked to a decrease in elastic energy: the release in elastic bulk and cohesive energy, allows some elements to reattach and some elements to detach.

Note that at the end of the simulation the total force has not dropped to 0, as the simulation is stopped at 5% attached length of the surface. As a result, the total elastic energy does is not zero when the simulation is stopped. It is however decreasing after approximately $\Delta = 0.25$.

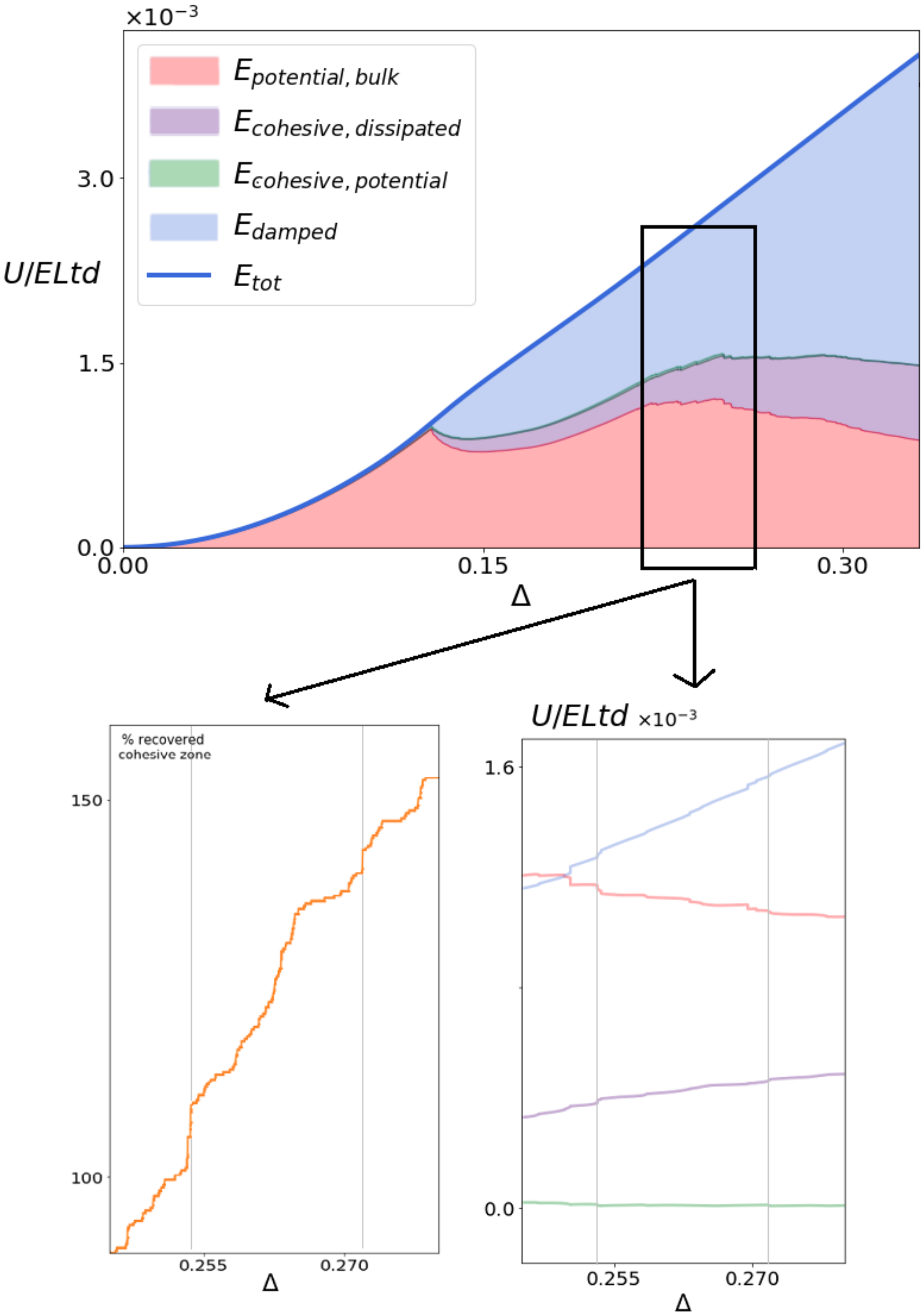

Figure 27: (top) Variation of the energy U during the peeling test for the simulation with parameter values (β, α, L/t, θ, ζ, γ, κ) = (8, 2, 15, 0.5$\times 10^{-3}$, 32$\times 10^{-3}$, 2.6, 0.4)that exhibits a sequence of interfacial cavitation, steady peeling, and curling for failure. On the x-axis the imposed displacement is varied and on the y-axis the energy U. The potential elastic bulk energy, cohesive energy that was dissipated, cohesive energy that is stored, and damped energy are plotted cumulatively. The cohesive energy is calculated for mixed-mode paths, and includes the energy of elements that have failed multiple times. The total energy put into the system by applying a force, is shown with a dark blue line as well. A region where stick-slip behavior first starts during the simulation is marked with a black frame and zoomed in on the bottom. (bottom left) The number of cohesive elements that have recovered during the simulation plotted in function of the imposed displacement, for the displacements in the black frame on the energy graph. Note that the percentage of elements is higher than 100, as elements are allowed to reattach multiple times. Two grey vertical lines are added at levels of displacement where a significant increase in the number of recovered elements is seen. (bottom right) Zoom-in on the different energies, plotted separately instead of cumulatively, for the imposed displacements marked with the black frame on the top graph. Two grey vertical lines are added at levels of displacement where a significant increase in the number of recovered elements is seen on the left bottom graph.

5.1.2 Pure Curling

5.1.2.1 *Failure Development*

In this simulation, with the exact same properties as the prior one detailed in Table 2, but only a different length ($L/t = 2$), the pure curling mode corresponding to the experiment described in Figure 15a is observed. The failure sequence is the same in the experiment and in the simulation when comparing the experimental figure with Figure 28. The amount of imposed displacement increases from Figure (I) to Figure (IV). In Figure (I) the pre-detachment state of the pad is shown. This pre-detached pad shows already a deformation field close to the one eventually observed under full failure, indicting a lot of induced stress before initiation of failure of the surface. In Figure (II) the curling from the opposite end is initiated and in Figure (III) it propagates until it is completed in Figure (IV).

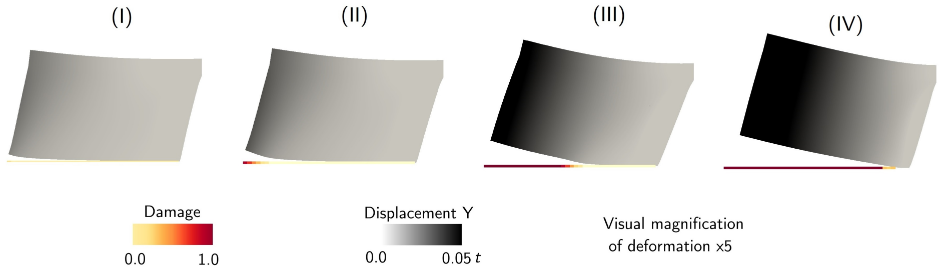

Figure 28: Failure sequence of the simulation with parameter values (β, α, L/t, θ, ζ, γ, κ) = (8, 2, 2, 0.5$\times10^{-3}$, 32$\times10^{-3}$, 2.6, 0.4)that exhibits a pure curling failure mode. The imposed displacement is varied from Figure (I) to Figure (IV). At every stage, the (magnified) deformation of the pad is shown, with additional shading for the vertical displacements. On the bottom of the pad, the level of damage of the cohesive zone is shown. In Figure (I) the pad is placed under loading and no damage is observed yet, a vertical lift at the surface near the opposite end is observed. (II) The first small detachment region near the opposite end starts developing. (III) Rapid development of the curling mode. (IV) The pad is fully detached. Direct correspondence with Figure 15a is observed.

Again, an intuitive understanding of the pad behavior can be achieved when examining the stress state of the pad. As illustrated in Figure 29 of the curling failure mode, the stress distribution gradients being spread over the whole pad, a resultant couple acts along its whole length. The mechanical and geometrical properties of the pad determine whether this one couple will be distributed over the whole pad or whether, as illustrated for the cavitation mode in Figure 23, the stress distribution will be more differentiated along the pad length. The internal force distributions and in-depth analysis of the mechanical conditions of the pad, are discussed in Appendix C.4.

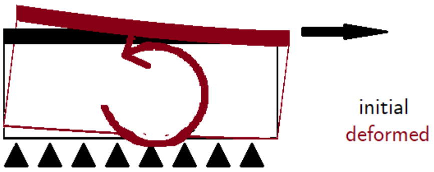

Figure 29: Illustration of the force distribution in the pad that exhibits pure curling as a failure initiation mode. The pulling of the pad parallel to the substrate combined with the boundary conditions at the adhesive surface creates a couple in the pad. This couple is distributed all over the pad, resulting in curling at the opposing end.

5.1.2.2 Surface Opening Profiles

In Figure 30, the same peeling process explained in Figure 28, is schematically represented by plotting the normalized horizontal displacement at the pad surface (left) and vertical displacement at the pad surface (middle) and the attached and detached regions (right) along the ad length (x/L) for an increasing imposed displacement (Δ). The curling process of detachment propagating quickly from the opposing end is visible on the right figure as the transition between the yellow and the red curve. No reattachment is present in this simulation, as along a vertical line (same position in the pad at different levels of imposed displacement), red (detached) does not transform back to yellow (attached). Before the curling development, the shear displacement on the left graph shows an almost uniform distribution over the full pad length (horizontal lines of the same color signifying the same tangential displacement). Once curling starts (top left of the left figure), the detached region shows higher displacement than the non-detached region. Meanwhile, before curling, the normal opening (middle graph), shows an approximately linear variation with respect to the position (linear variation of color in the horizontal direction). Before the curling then initiates, the normal opening already starts increasing significantly (region above the blue line on the top left of higher displacement). Based on this remark, in curling failure, the normal opening is concluded to be the main parameter driving failure behavior.

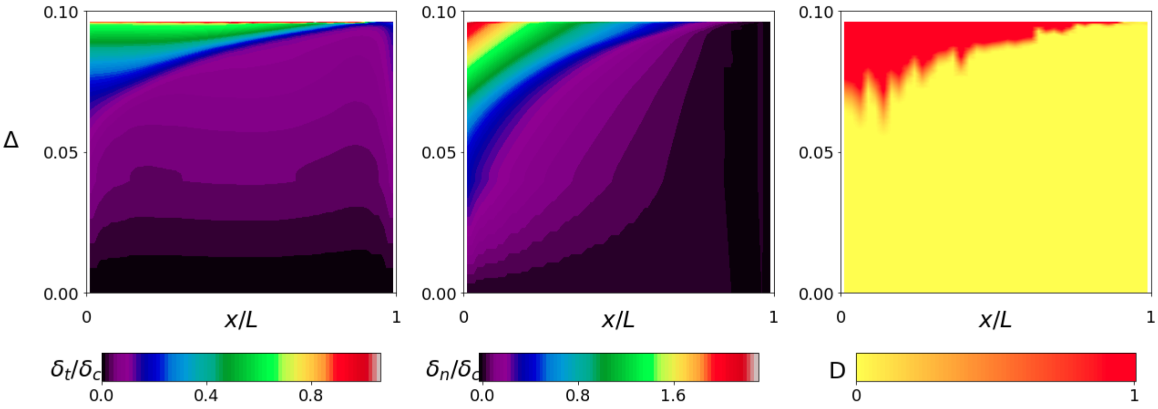

Figure 30: Development of failure and opening profiles for the simulation with parameter values $(\beta,\ \alpha,\ L/t,\ \theta,\ \zeta,\ \gamma,\ \kappa)$ = (8, 2, 2, 0.5$\times10^{-3}$, 32$\times10^{-3}$, 2.6, 0.4)that exhibits a pure curling failure mode. (left) On the y-axis Δ or the amount of pulling displacement is advanced, and on the x-axis x/L or the pad length is advanced. In other words, the consecutive states of the tangential opening of the pad are vertically advanced over imposed displacement. The color represents the amount of the tangential displacement. (middle) On the y-axis Δ or the amount of pulling displacement is advanced, and on the x-axis x/L or the pad length is advanced. The consecutive states of the pad are vertically joined over imposed displacements. The color scheme shows the normalized vertical displacement value. (right) On the y-axis Δ or the amount of pulling displacement is advanced, and on the x-axes x/L or the pad length is advanced. The consecutive states of the pad are vertically joined over imposed displacements. The color scheme shows the advancement of the damage level. No reattachment is observed in these graphs.

When comparing Figure 30 middle with the corresponding experimental vertical opening plot in the (Δ, δ_n) plane discussed in Figure 16a, again a very good correspondence is obtained. The curling vertical opening front starts at $\Delta = 0, x = 0$, and propagates diagonally upwards right on the graph: over time the size of the curling opening grows steadily (boundary between pink line and dark blue line). Near the end of the failure, both the simulation and the experiment show a change of slope of this opening front, where the lift-off front propagates faster before ultimate failure. This new slope coincides with the slope of the detachment front on the right detachment graph of Figure 30. This correspondence ads to the conclusion that the model developed here is able to successfully represent the different competing modes of adhesive pad failure with a proper link to the pad geometry.

5.1.2.3 Load-Displacement Response

Having successfully captured numerically the sequence of failure of the curling detachment mode as well, the applied force versus the imposed displacement is plotted in Figure 31 left together with the fraction of surface failure in function of the imposed displacement in Figure 31 right. The pure curling plots are shown in purple, and the interfacial cavitation, steady pealing and curling discussed in Section 24 is included again in orange. The latter was discussed already in Section 5.1.1.3. The curling mode force curve in Figure 31 left shows the same bump in the hardening part because of the switch to dynamics: this is not a physical phenomenon and can be ignored. The graph shows a non-linear hardening phase and once at peak force, fails immediately catastrophically. On the right graph, it can be seen the damage stays at zero for a certain displacement and at the initiation of the first failure occurring, continues to fail quickly (rather vertical line) without any reattachment (no subsequent decrease of the percentage of broken surface). Both the failure force and the stiffness during the hardening phase of the curling simulation is lower than that of the steady peeling plot. The main reason for this is of course the shorter length of the pad: there is less material that can absorb deformation energy, and the shorter length does not allow a significant variation of the shear stress.

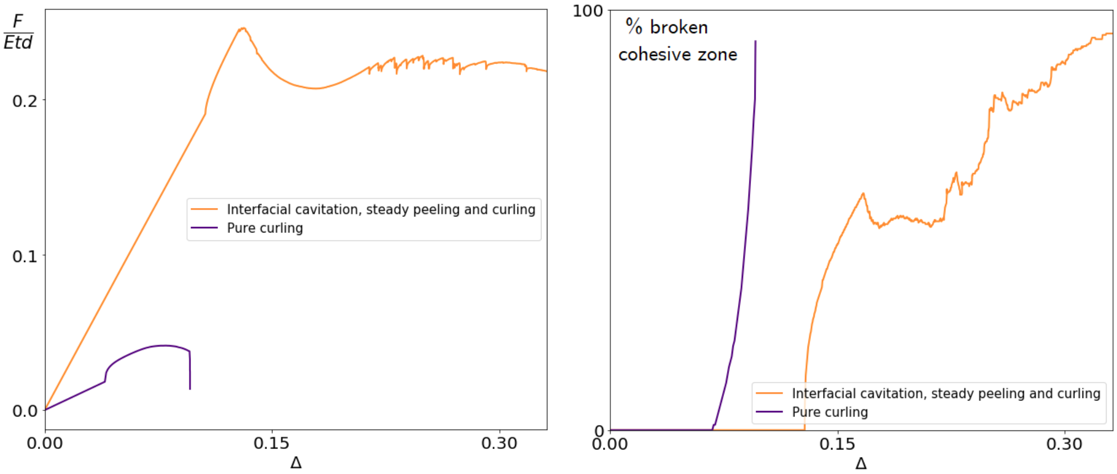

Figure 31: Force-displacement (left) and percentage of failure-displacement (right) graphs for the simulation with parameter values (β, α, L/t, θ, ζ, γ, κ) = (8, 2, 2, 0.5$\times 10^{-3}$, 32$\times 10^{-3}$, 2.6, 0.4)that exhibits a pure curling failure mode. (left) The force is the total pulling force in the X-direction that needs to be exerted upon the pulling end of the backing to enforce the amount of displacement imposed and is shown on the y-axis. The amount of displacement imposed is shown on the x-axis. (right) The % of broken length on the cohesive zone or adhesive surface on the y-axis shows the advancement of failure and the instances of reattachment. The amount of displacement imposed is shown on the x-axis. Reattachment is characterized by the broken percentage going down again. For reference, the plots of the interfacial cavitation with steady peeling is shown as well.

In the curling simulation as well, quantitative agreement in the order of magnitude with the experiments from Cohen et al. [2018] is found. The peak force for the curling mode is here $\frac{F}{Etd} = 0.02$, and the experimentally observed peak force is $\frac{F}{Etf} = 0.05$. Again, this increases the confidence in the model showing the right phenomena.

5.1.2.4 Energy Distribution

The energy evolution will be discussed, with Figure 32 representing the energy variation (y-axis) in function of the imposed displacement (x-axis). The dark blue line shows the total energy input by the application of a force, and the red, purple, green and light blue regions show respectively the elastically stored energy in the bulk, cohesive energy that has been dissipated (including it multiple times for elements that reattached multiple times), stored cohesive energy, and damped energy. During the initial linear elastic phase, all the energy is invested into elastic deformation (red region at the beginning). Upon the start of the failure line, first an increase in elastically stored energy in the cohesive elements and afterwards, a dissipation of the cohesive elastic and bulk elastic zone into an increasing dissipated cohesive energy is seen. Where the number of surface elements elastically loaded to a high degree, was virtually non-existent in the interfacial cavitation, it is apparent here. The surface zone first is loaded with elastic energy, to subsequently rapidly fail upon the dissipation of the bulk energy into the failure of surface elements.

It is seen the amount of damped energy is lower than for the first discussed failure mode, discussed in Figure 27. While the curling happens fast rather than steadily, the amount of high-frequency events that we relate to snap-through events is a lot lower. Almost no reattachment occurs and elements fail steadily at a rapid rate, rather than because of localized stress distributions.

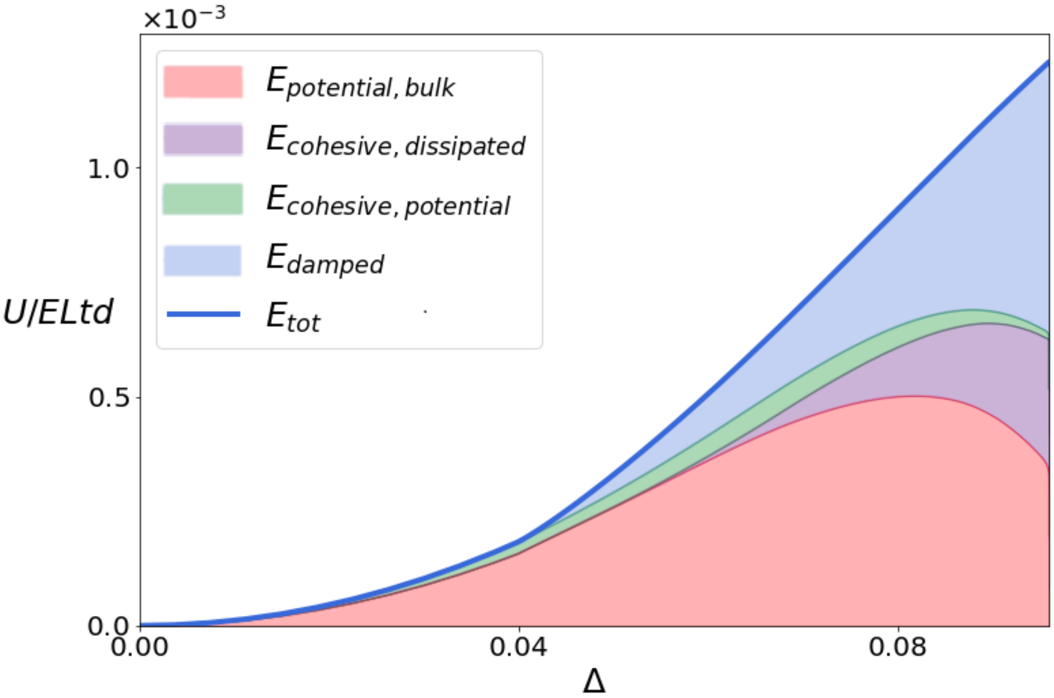

Figure 32: Variation of the energy U during the peeling test for the simulation with parameter values (β, α, L/t, θ, ζ, γ, κ) = (8, 2, 2, 0.5$\times 10^{-3}$, 32$\times 10^{-3}$, 2.6, 0.4)that exhibits a pure curling failure mode. On the x-axis the imposed displacement is varied and on the y-axis the energy U. The potential elastic bulk energy, cohesive energy that was dissipated, cohesive energy that is stored, and damped energy are plotted cumulatively. The cohesive energy is calculated for mixed-mode paths, and includes the energy of elements that have failed multiple times. The total energy put into the system by applying a force, is shown with a dark blue line as well.

5.1.3 Curling Followed by Interfacial Cavitation

To illustrate how curling, and the associated high level of stress build-up before failure (discussed in Section 5.1.2), can be influenced by more than only the length parameter, an additional simulation result is discussed. The same length as for the cavitation simulation in Section 5.1.1 is used, and the pad is shown to exhibit curling behavior as the failure initiation mode. All parameters are kept the same as in Section 5.1.1, except for the backing stiffness and the cohesive zone parameters.

	β	γ	ζ
Steady peeling	8	2.6	0.03
Pure curling	20	4.8	0.06

Table 3: Main difference between a steady peeling (Section 5.1.1) and a pure curling simulation (current section).

5.1.3.1 Failure Development

The failure of this pad, shown in Figure 33 with the imposed displacement increasing from (I)-(IV), shows a mixed-mode catastrophic failure with interfacial cavitation peeling. At every stage, the (magnified) deformation of the pad is shown, with additional shading for the vertical displacements. On the bottom of the pad, the level of damage of the cohesive zone is shown. Figures (I)-(II) show initially lift of the opposing end of the pad and curling detachment (I)-(II), Figure (III) shows the sudden development of an interfacial cavitation and finally in (IV) both failure field join.

Figure 33: Failure sequence of the simulation with parameter values (β, α, L/t, θ, ζ, γ, κ) = (20, 2, 15, 0.5×10^{-3}, 60×10^{-3}, 4.8, 0.4)that exhibits curling with interfacial cavitation. The imposed displacement is varied from Figure (I) to Figure (IV). At every stage, the (magnified) deformation of the pad is shown, with additional shading for the vertical displacements. On the bottom of the pad, the level of damage of the cohesive zone is shown. In Figure (I) the pad is placed under loading and no damage is observed yet, a vertical lift at the surface near the opposite end is observed. (II) The first small detachment region near the opposite end starts developing. (III) Sudden propagation of failure of the interfacial cavitation mode near the pulling. (IV) Interfacial cavitation detachment and curling detachment merge. The pad is fully detached.

For the intuitive understanding, a mix of the two earlier failure modes can be imagined: during phase (I)-(II) the stress distribution over the pad has a single resultant couple, as illustrated for the curling in Figure 29. After this, for pure curling to continue, the entire pad would need to continue to have a stress distribution spread over the whole pad, as shown for the pure curling mode 28. For this pad, because of its length, the variation in distribution of stresses resulted in multiple different couples over the pad length, so that the shape and stress state of the pad reverts back to the situation described for the interfacial cavitation and peeling mode in Figure 23. Again, for the detailed internal force distributions and an in-depth analysis of the mechanical conditions of the pad, the reader is referred to Appendix C.4. This simulation especially shows how competing failure modes in function of material and geometrical parameters develop.

5.1.3.2 Surface Opening Profiles

In Figure 30, the same peeling process explained in Figure 28, is schematically represented by plotting the normalized horizontal displacement at the pad surface (left), the vertical displacement at the pad surface (middle) and the attached and detached regions (right) along the length on the layer (x/L) for varying imposed levels of displacement (Δ). On the right figure, the long phase of build-up of pre-peak stresses (yellow) followed by rapid curling from the opposite end (red near $x = 0$) and rapid interfacial cavitation from the pulling end (red near $x = L$) are visible. During this long phase before any detachment occurs, the part of the pad near the pulling end develops a larger tangential opening (left figure) and the opposite end a larger normal opening (middle figure). When comparing this to the pure curling phase from Section 5.1.2, where the tangential displacement was uniform over the pad length, the reason for the development of the interfacial cavity becomes apparent: the driving force is the higher tangential displacement relative to the pulling end.

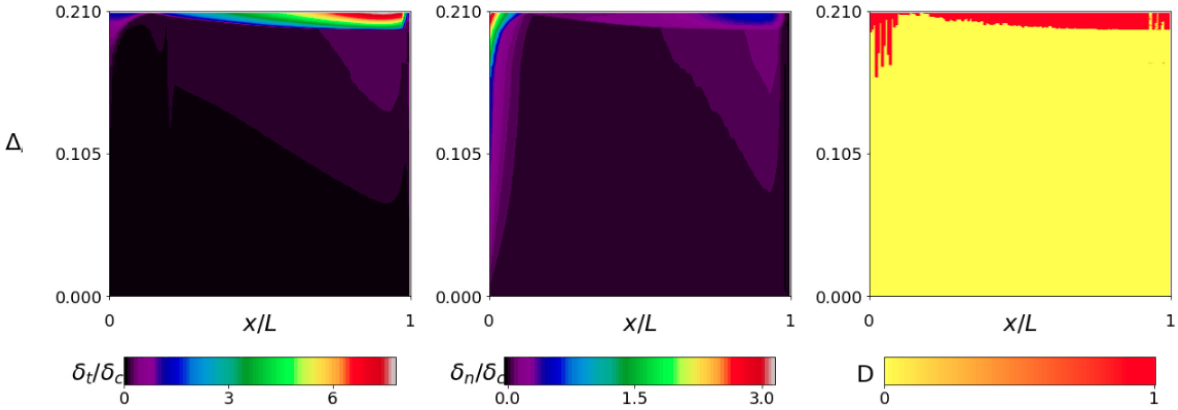

Figure 34: Development of failure and opening profiles for the simulation with parameter values (β, α, L/t, θ, ζ, γ, κ) = (20, 2, 15, 0.5$\times10^{-3}$, 60$\times10^{-3}$, 4.8, 0.4)that exhibits a curling with interfacial cavitation combined failure mode. (left) On the y-axis Δ or the amount of pulling displacement is advanced, and on the x-axis x/L or the pad length is advanced. In other words, the consecutive states of the tangential opening of the pad are vertically advanced over imposed displacement. The color represents the amount of the tangential displacement. (middle) On the y-axis Δ or the amount of pulling displacement is advanced, and on the x-axis x/L or the pad length is advanced. The consecutive states of the pad are vertically joined over imposed displacements. The color scheme shows the normalized vertical displacement value. (right) On the y-axis Δ or the amount of pulling displacement is advanced, and on the x-axes x/L or the pad length is advanced. The consecutive states of the pad are vertically joined over imposed displacements. The color scheme shows the advancement of the damage level. No reattachment is observed in these graphs.

5.1.3.3 Comparison with Steady peeling

This simulations in which the pad failure initiates with curling shows two main differences with the simulation that has a steady peeling mode as a main failure mode if L/t is kept constant.

First, it has a higher value of β, meaning a higher Young's modulus of the backing, so that more elastic energy can be stored in the backing. The larger difference in Young's modulus between the adhesive and the backing, makes that for the same displacement level a higher applied force is necessary. This force creates stresses further through the pad, affecting a larger pad length. The higher β allows loads spreading out further through the pad, facilitating the normal opening at the opposite end through the spreading of force distribution over the whole pad, as opposed to locally, which eventually leads to curling.

Secondly, a higher value of γ and ζ for the same value of θ has also been used: the tension at the initiation of failure of the adhesive surface is higher while the fracture energy remains the same, also resulting in a shorter, steeper, softening phase of the cohesive law. The shorter softening phase with a higher peak stress in the surface law allows more of the elastically stored energy to be available at the moment of the failure of the first element. In the case where all of the pad surface is already loaded to almost peak stress and very little additional energy can be absorbed by one single element, this will quickly lead to failure of multiple elements.

5.1.3.4 Load-displacement Response

The high build-up of pre-failure stress over the full adhesive pad and surface zone, and the subsequent quick stress drop in the different surface elements, is also directly visible on the force-displacement plots in Figure 35. This figure shows the applied force versus imposed displacement left and the fraction of failed surface elements in function of the imposed displacement on the right. The current simulation plots are shown in red, the steady peeling discussed in Section 24 is included again in orange and the pure curling discussed in Section 5.1.2 is included in purple. The curling followed by interfacial cavitation simulation has a relatively long linear elastic phase (compared to the two other simulations, left figure), corresponding with a level of almost zero damage (right figure). Once the peak force is reached, the very short softening phase (left figure), corresponding to a sudden failure without reattachment (right graph) concludes the abrupt failure of this adhesive pad.

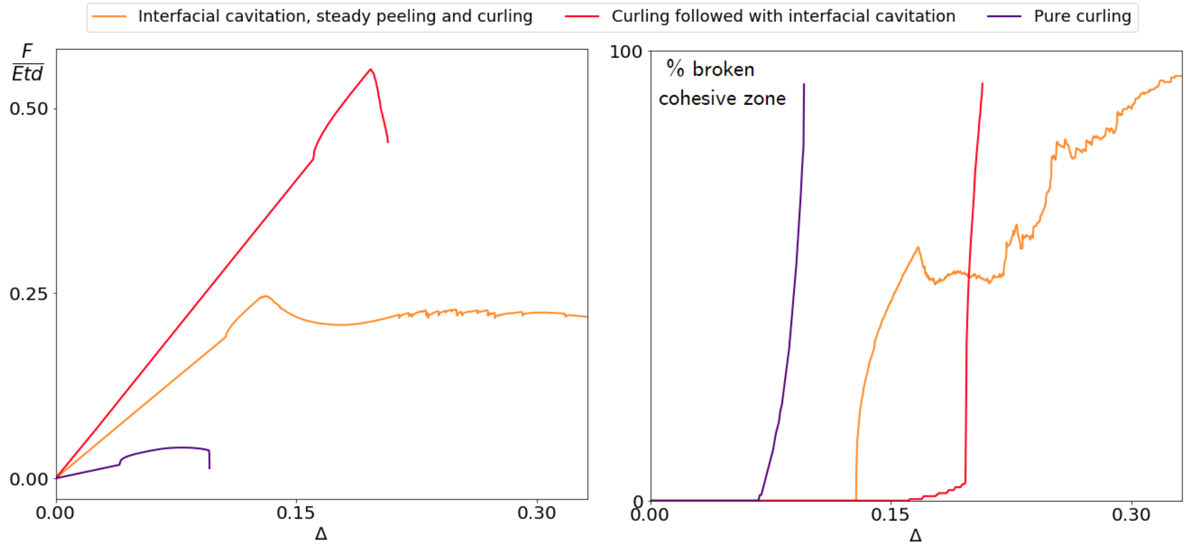

Figure 35: Force-displacement (left) and percentage of failure-displacement (right) graphs for the simulation with parameter values (β, α, L/t, θ, ζ, γ, κ) = (20, 2, 15, 0.5×10^{-3}, 60×10^{-3}, 4.8, 0.4)that exhibits a pure curling failure mode. (left) The force is the total pulling force in the X-direction that needs to be exerted upon the pulling end of the backing to enforce the amount of displacement imposed and is shown on the y-axis. The amount of displacement imposed is shown on the x-axis. (right) The % of broken length on the cohesive zone or adhesive surface on the y-axis shows the advancement of failure and the instances of reattachment. The amount of displacement imposed is shown on the x-axis. Reattachment is characterized by the broken percentage going down again and is not observed for the curling mode. For reference, the plots of the interfacial cavitation with steady peeling, and the pure curling mode are shown as well.

Compared to the steady peeling failure mode, the overall elastic stiffness of the pad and its peak force is higher than for the previous cases. This corresponds to the argument made earlier stating that the curling pad accumulates more elastic energy over a longer pad length for the same level of displacement. The softening phase after the peak strength is also very abrupt and short for the curling mode, corresponding to the abrupt failure of almost all elements, relative to a long softening phase for the steady peeling simulation, where the elements fail slowly and have time to reattach. This supports again the earlier explanation about the high amount of stored elastic energy being absorbed by the very quick and sudden failure of the surface elements that are already loaded close to their failure level.

5.1.3.5 Energy Distribution

The energy evolution will be discussed, with Figure 36 representing the energy variation (y-axis) in function of the imposed displacement (x-axis). The dark blue line shows the total energy input by the application of a force, and the red, purple, green and light blue regions show respectively the elastically stored energy in the bulk, cohesive energy that has been dissipated (including it multiple times for elements that reattached multiple times), stored cohesive energy, and damped energy. During a very long initial elastic phase, all the energy is invested into elastic deformation (red region until $\delta = 0.18$). This region, contrary to what was observed in the pure curling simulation, continues rather far in the simulation. As a longer pad is loaded here, this higher investment of elastic energy to fully pre-load the pad prior to any failure is natural. At the encounter of maximal failure stress, the elastic energy transferring into cohesive dissipated energy, also supporting our earlier argument about the mechanical reason for the occurrence of this failure mode. The lack of a high build-up of elastic cohesive energy before peak force is not corresponding to the mechanism observed in pure curling, where the dissipation of energy into the failure of the surface starts already before peak force.

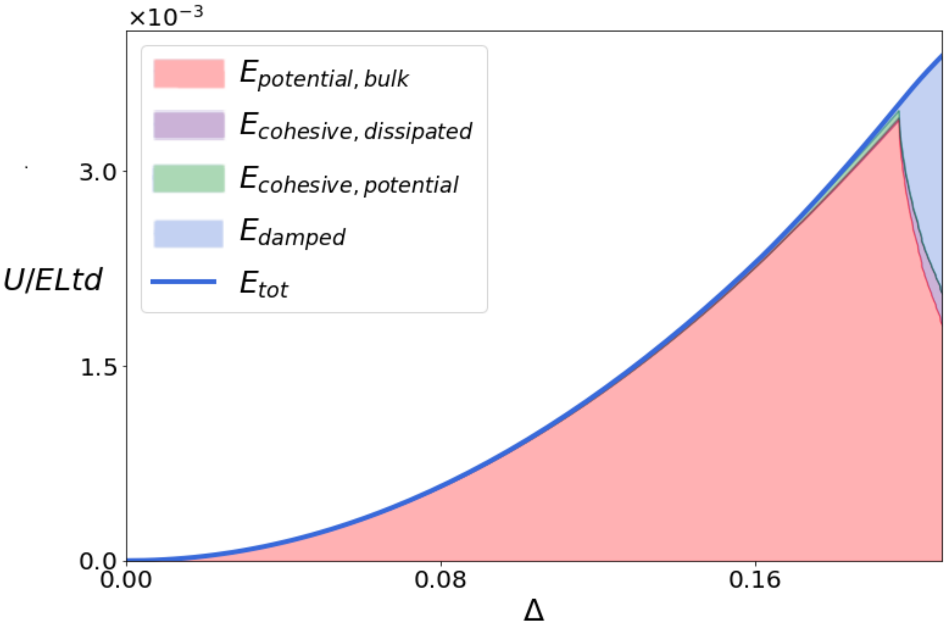

Figure 36: Variation of the energy U during the peeling test for the simulation with parameter values (β, α, L/t, θ, ζ, γ, κ) = (20, 2, 15, 0.5$\times10^{-3}$, 60$\times10^{-3}$, 4.8, 0.4)that exhibits a curling with interfacial cavitation failure mode. On the x-axis the imposed displacement is varied and on the y-axis the energy U. The potential elastic bulk energy, cohesive energy that was dissipated, cohesive energy that is stored, and damped energy are plotted cumulatively. The cohesive energy is calculated for mixed-mode paths, and includes the energy of elements that have failed multiple times. The total energy put into the system by applying a force, is shown with a dark blue line as well.

5.2 Infinitely Long Pad

To study the emergence of the stick-slip events in more detail, consider an infinitely long pad: the present pad length was such that no stress at all is created at the opposite end of the pad. The material parameters used for this simulation are detailed in Appendix C.1. The intuitive mechanics of failure can be predicted based on the previous simulation results and are shown in Figure 37. The boundary conditions of a rigid substrate, a compliant surface (lower stiffness k than the adhesive stiffness E/t), and a stiffer backing pulled to the side, are responsible for the introduction of stress distributions in the adhesive pad with resultant couples. In an infinitely long pad, the stress distributions will gradually decrease from the pulling end through the pad.

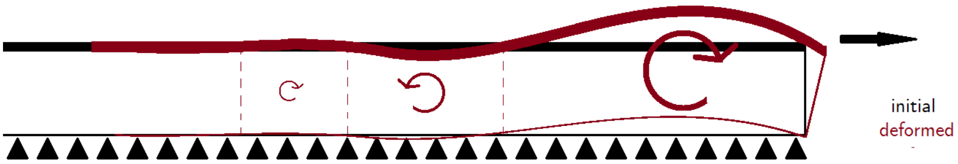

Figure 37: Illustration of the force distribution in the infinitely long pad. The pulling of the pad parallel to the substrate at the stiffer backing combined with the boundary conditions at the adhesive surface creates a gradient in stress states over the pad. Notably, there is also a gradient along the pad length in the pad, resulting in multiple different resultant couples from the internal stress distributions.

Figure 38 shows the propagation of peeling over the pad. The imposed displacement is increased from (I) to (VIII). At every stage, the (magnified) deformation of the pad is shown, with additional shading for the vertical displacements. On the bottom of the pad, the level of damage of the cohesive zone is shown. In light of the above analysis and with this failure sequence as pictured in Figure 38, it is now possible to explain the mechanics related to the reattachment events.

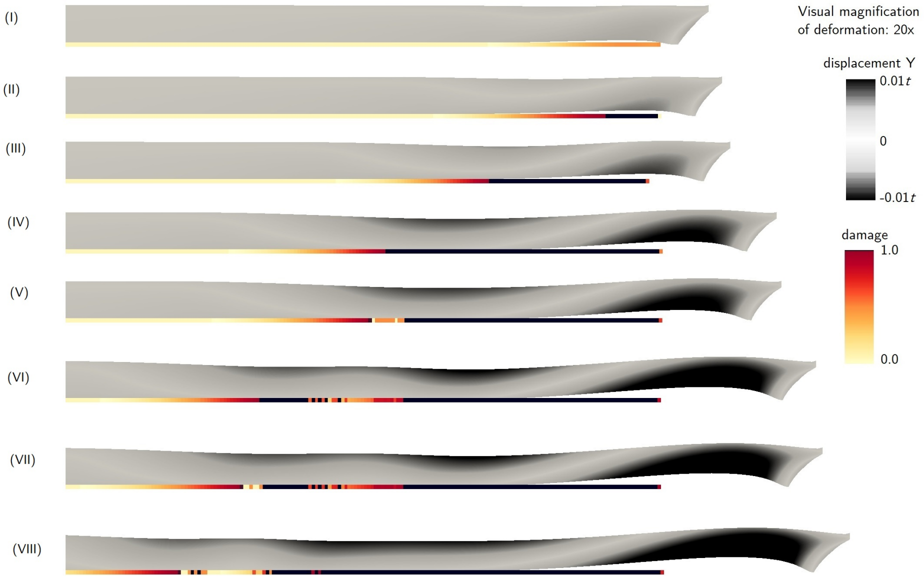

Figure 38: Failure sequence of the simulation of an infinitely long pad with parameter values (β, α, L/t, θ, ζ, γ, κ) = (8, 2, 8, 0.5$\times 10^{-3}$, 8$\times 10^{-3}$, 0.64, 0.4). The imposed displacement is varied from Figure (I) to Figure (VII). At every stage, the (magnified) deformation of the pad is shown, with additional shading for the vertical displacements. On the bottom of the pad, the level of damage of the cohesive zone is shown. (I) Start of the loading, vertical lift of the pad at the surface near the pulling can be observed, as well as the initiation of damage development at the region with the lift. (II)-(IV) A damage front develops and propagates over the pad length from the pulling end. (V) A reattachment region is developed close to the detachment propagation front. (VI) Detachment and reattachment front propagate. (VII-VIII) A new reattachment region behind the detachment front is formed: the process from (V)-(VI) repeats itself.

In Figure 38 (I), before the onset of failure, the initiation of the failure of an interfacial cavity is observed as the pad above it lifts vertically under the influence of imposed stresses (shown in Figure 37). Figure (II)-(III) show then the quick formation of this interfacial cavitation region and the steady peeling phase afterwards. In Figure (IV) a region of downwards displacement on the pad is formed (dark shaded, to the right of the failure propagation front). We see here the mechanics that were also observed in the simulation with steady peeling (Section 5.1.1): the pad length is too long (for its other energetic properties such as the backing stiffness) for the full detached region to be under one uniform stress state. Rather, a different stress distribution in the middle is observed and causes the downwards moment of the adhesive pad at this point in space and time. In Figure (V) it can then be observed that this earlier region of downwards displacement is where the adhesive pad will reattach due to contact with the surface. On Figure (VI) both the detachment front and the reattachment front propagate and influence the stress state in the pad around them: we observe now two regions of downwards displacement of the top of the adhesive pad. On Figure (VII) the development of a new reattachment region close to the pulling end is observed. The influence of this region development on the stress distributions in the pad will eventually cause the first reattachment region to definitively detach, as shown in Figure (VIII). This process of development of a reattachment region due to stress release propagated as a stress state through the pad length, is then stopped by the next reattachment movement. This sequence is repeated in a steady-state manner while the pad failing continues.

Figure 39 depicts for this simulation the applied force versus imposed displacement left and the fraction of failed surface in function of the imposed displacement on the right. After an initial elastic region on the left force graph, corresponding to zero failure on the right failure graph, the pad starts detaching (increase in the right graph). The drops and re-increases in the force graph on the left, relating to the reattachment of cohesive elements (drops in the failure propagation graph on the right), confirm that these events of detachment and reattachment are indeed stick-slip events. Furthermore, the eventually approximately constant slope of the reattachment region, is an additional indicator for a steady-state regime in the simulation.

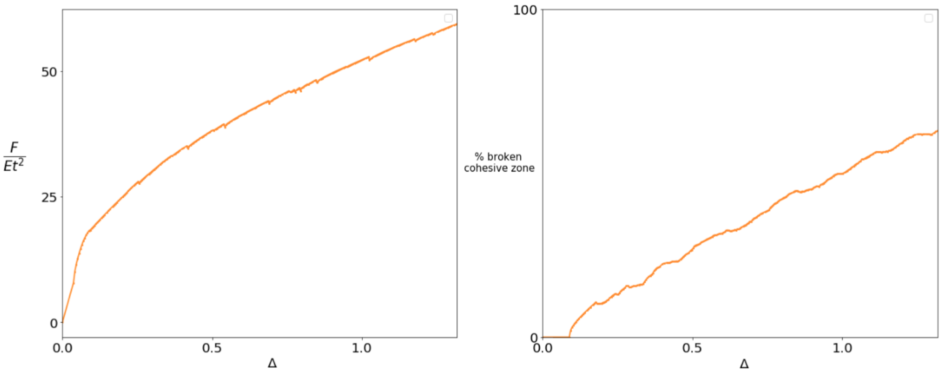

Figure 39: Force-displacement (left) and percentage of failure-displacement (right) graphs for the infinitely long pad with parameter values (β, α, L/t, θ, ζ, γ, κ) $=$ (8, 2, 8, 0.5$\times10^{-3}$, 8$\times10^{-3}$, 0.64, 0.4). (right) graphs for the simulation with parameter values (β, α, L/t, θ, ζ, γ, κ) $=$ (20, 2, 15, 0.5$\times10^{-3}$, 60$\times10^{-3}$, 4.8, 0.4)that exhibits a pure curling failure mode. (left) The force is the total pulling force in the X-direction that needs to be exerted upon the pulling end of the backing to enforce the amount of displacement imposed and is shown on the y-axis. The amount of displacement imposed is shown on the x-axis. (right) The % of broken length on the cohesive zone or adhesive surface on the y-axis shows the advancement of failure and the instances of reattachment. The amount of displacement imposed is shown on the x-axis. Reattachment is characterized by the broken percentage going down again and is not observed for the curling mode.

In Figure 40, the normalized vertical displacement at the pad surface (left) and the attached and detached regions (right) along the position in the pad (x/L) for increasing imposed displacement (Δ) are shown. Reattachment on the right failure graph is observed if over a vertical line (thus on one position in the pad over the variation of time) the damage reverts back from 1 (red) to 0 (yellow). These figures correspond to the failure mechanism of stress distributions driving the detachment and reattachment regions as described in Figure 38, but is zoomed out over a longer range of Δ values. On the left graph, after the initial development of failure, there is a detachment front moving upwards left in the figure (the most left boundary between the pink region and the dark blue line). To the right of this detachment front on the figure is a reattachment area of zero vertical opening and thus contact with the surface: the pink line on the figure to the right of the detachment wave. Perpendicular to this line on the figure, smaller alternating blue and pink lines are observed: alternating detachment and reattachment fronts. On the right failure graph, the most left first detachment front corresponds to the transition between the fully attached region (yellow) to the mixed (yellow-red, reattachment) and full failure region (red). The reattachment wave in pink on the left Figure, with connecting perpendicular smaller pink lines, correspond to the regions on the right failure graph where reattachment is observed (dotted yellow regions in the red region). In summary, after the initial development of failure, the detachment wave and reattachment wave are steady-state or propagate with a constant velocity and transmits periodic waves of reattachment perpendicular to its direction on the figure.

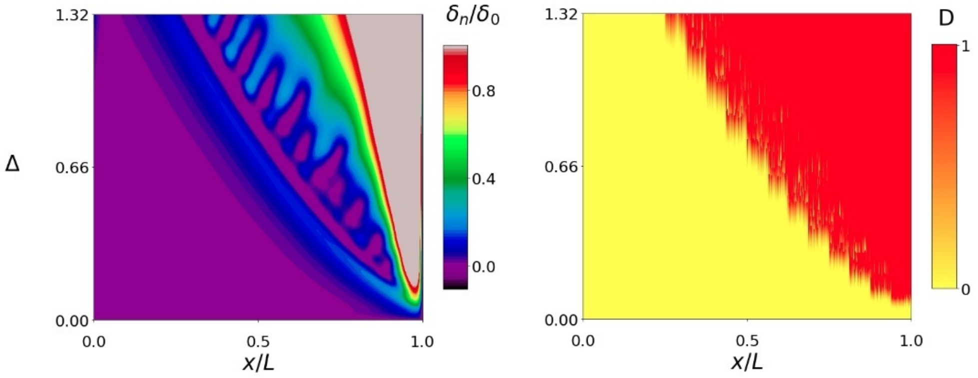

Figure 40: Development of failure and opening profiles for the infinitely long pad with parameter values (β, α, L/t, θ, ζ, γ, κ) = (8, 2, 8, 0.5$\times 10^{-3}$, 8$\times 10^{-3}$, 0.64, 0.4), where no effect from the opposite end is felt during development of the steady peeling front. (left) On the y-axis Δ or the amount of pulling displacement is advanced, and on the x-axis x/L or the pad length is advanced. The consecutive states of the pad are vertically joined over imposed displacements. The color scheme shows the normalized vertical displacement value. (right) On the y-axis Δ or the amount of pulling displacement is advanced, and on the x-axes x/L or the pad length is advanced. The consecutive states of the pad are vertically joined over imposed displacements. The color scheme shows the advancement of the damage level. The areas on the right graph that evolve vertically from red (damage) to yellow (no damage), have reattached.

The propagation of the areas of detachment is also referred to as a Schallamach wave. While extensive studies for force-displacement diagrams oscillating around a constant force have been done, the ones showing this steady-state increase in force are rather sparse. Here, this type of Schallamach wave can be observed in the simulation of the zero-degree peeling behavior of an adhesive pad. If we take for example the vertical line in the middle of the figure matching the point located at the half of the pad, moving upwards means increasing level of imposed displacement. One can see that the state of this point goes from contact (pink on the left graph) to vertical upwards displacement, to contact and vertical displacement again. Conversely, if we take a horizontal line at the middle of the y-axis, we have the state of the entire pad at all locations at a fixed moment in time[4]. The transition from contact to vertical opening to contact and to vertical opening again can also be seen in this direction. The phenomenon is considered a wave since it exhibits an oscillatory shape in both variables and location dependent. The understanding of the mechanics driving the Schallamach wave propagation, contributes to a better understanding of the stick-slip phenomena observed.

---

[4] In the quasi-static simulations, time needs to be interpreted as the increasing displacement in the absence of dynamics.

6 Discussion on the Effect of Non-Dimensional Parameters

Now that correspondence between failure modes, stick-slip, and failure forces of simulations and experiments is confirmed, the influence of the surface properties on the mechanical behavior of the pad can be further investigated. This point is especially important considering the fact that the cohesive properties are those that are the most difficult to identify. The influence of geometrical and bulk properties β and L/t has become clear when studying the mechanics of the different failure modes. Parameter α has little influence, as confirmed in Appendix C.5. Meanwhile, the surface properties are experimentally observed to have a large range of available values (Section 4.1.4) and their influence is less mechanically evident than the influence of β and L/t. Moreover, as will become clear here their influence is crucial for the stick-slip mechanism.

This chapter will conduct a sensitivity analysis on parameters θ and ζ that are the non-dimensional equivalents of respectively the fracture energy and maximal stress of the cohesive law. Parameters ζ and θ were chosen since the parametric study (Appendix C.5) showed that changing γ by changing δ_0 had practically no influence on the occurrence of stick-slip events in the studied parameter range. Appendix C.5 contains the sensitivity analysis for all other parameters as well for the sake of completeness. Simulations will be run from the reference cases, of which parameter values are listed in Appendix C.1.

6.1 Influence of Cohesive Zone Parameters

6.1.1 Influence of Surface Failure Energy θ

With increasing θ (non-dimensional equivalent of surface fracture energy), while keeping all other parameters constant, the softening phase of the cohesive law becomes longer, while the elastic phase remains constant. The same opening plots that were studied earlier for the failure mode are now compared for two simulations that only differ in the value of θ used in them. Figure 41 shows the normalized horizontal displacement along the pad surface (left) and the normalized vertical displacement along the pad surface (middle), as well as the attached and detached regions (right) along the pad length (x/L) for varying imposed displacements (Δ).

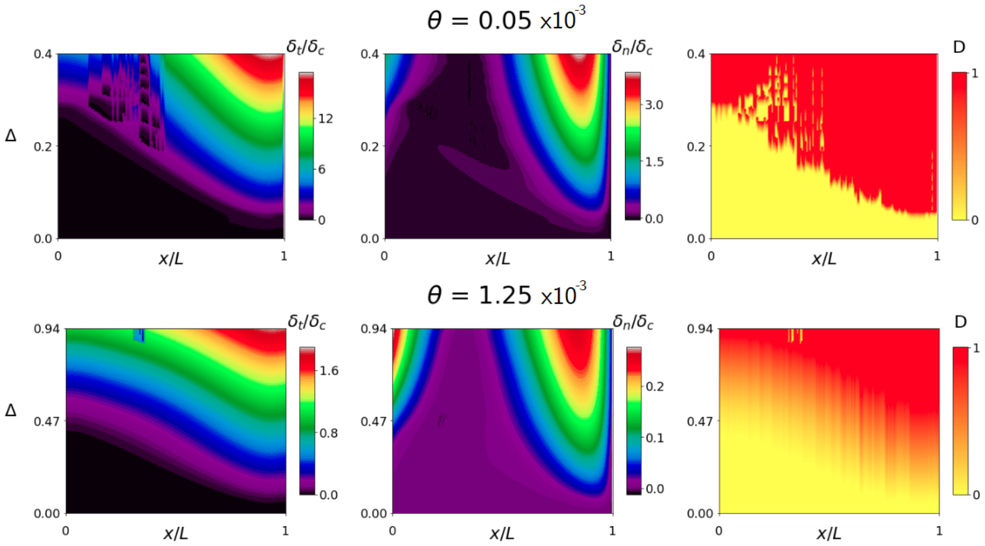

Figure 41: Detachment analysis of the surface of two pads with as only different parameter θ. The amount of displacement is advanced over the y-axis and the pad length is advanced over the x-axis on each of the Figures. The left graphs show the opening of the adhesive surface in the tangential direction, the middle graphs the opening in the normal direction, and the right graphs the damage of the surface.

The first very clear difference is observed in the right damage graph, where the larger value of θ is responsible for a softening phase (orange parts, $0 < D < 1$) that is a lot more extended over the y-axis (imposed displacement) than at the smaller value of θ, where virtually no softening phase is observed (almost no intermediate values of damage present). Interestingly, in the area where softening occurs on the large θ graph, reattachment occurs on the small θ graph. Virtually no reattachment is observed for the larger θ. Thus, a higher area under the softening part of the curve, equivalent to a higher fracture toughness of the surface, prevents reattachment. The initiation of the softening phase is also seen to be starting at a higher displacement for a large θ. In the Figure 41 left graphs, it is observed that the tangential opening in both graphs follows the shape of the propagation front (initiation of detachment line where D becomes larger than 0) on the failure development graph. Additionally, the curling normal opening on the middle graph for a higher θ is higher than for a lower θ as a result of these tangential displacements, the curling has more time to develop as its failure is accompanied by softening as well.

As discussed earlier, during the failure of cohesive surface elements stress relaxation to the surrounding bulk material is provided. This sudden stress relaxation and its corresponding deformation field, then create stress distributions in the pad that cause vertical displacements and ultimately reattachment. As the softening is stretched out over a longer range of imposed displacements for a bigger value of θ, this stress relaxation is not happening suddenly anymore. In addition, as softening of the cohesive elements is going on after the peak stress for higher θ, in a region where the element would have broken for lower θ, during this softening phase energy is absorbed and the rest of the pad initiates failure later.

In Figure 42 left the corresponding applied force in function of the imposed displacement, and on the right, the fraction of broken elements of the surface are plotted for a range of θ values. In this right figure, the lack of reattachment in the graphs with higher θ is confirmed. The globally increased force with increasing θ (Figure 42 left) also corresponds to the higher total energy of the system to reach full failure. Further, it is visible on the figure that stick-slip related to the reattachment events is present only at low values of θ.

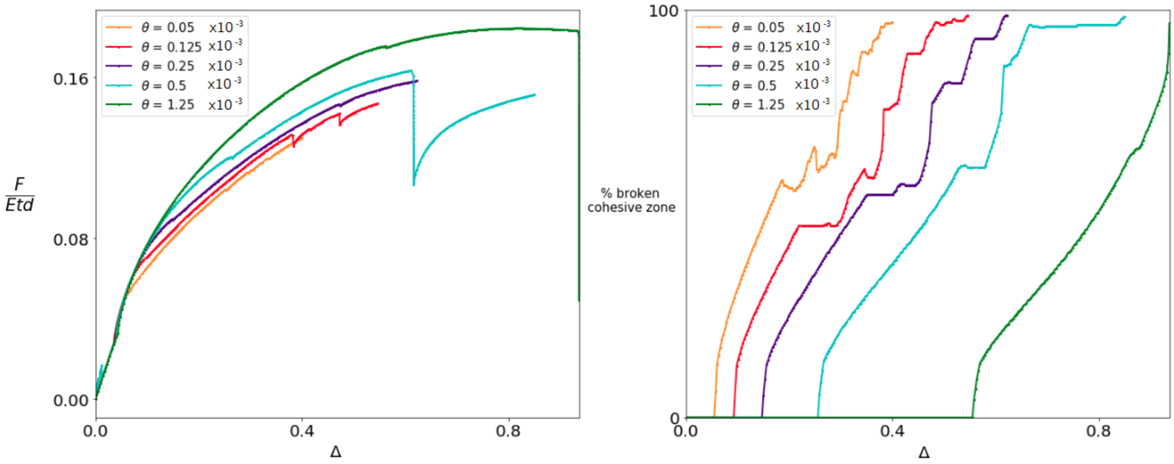

Figure 42: Force-displacement (left) and percentage of failure-displacement (right) graphs for pads with as only different parameter θ. The force is the total pulling force in the X-direction that needs to be exerted upon the pulling end of the backing to pull this end the amount of displacement imposed. Note that the large drop in the force near the end of the simulation in the blue curve is a non-physical mesh effect and can be disregarded, as explained in the convergence analysis in Appendix C.2.

6.1.2 Influence of Maximal Surface Traction ζ

With increasing ζ (non-dimensional equivalent of peak traction of the cohesive law), while keeping other parameters (including θ or non-dimensional surface energy) constant, the higher maximal stress will lead to a lower area under the softening part of the cohesive law (while increasing the area under the elastic part of the law). A shorter softening phase will be obtained, meaning the difference between δ_c and δ_0 is lower. In Figure 43 left the corresponding force in function of the imposed displacement, and on the right, the fraction of surface failure is plotted for a range of ζ values. On this figure, it is clear that with increasing ζ, the applied force levels increase and stick-slip events increase (Figure 43). The increase of force is a natural result of the maximal stress in the cohesive law increasing.

For interpretation of the increase in stick-slip events, there are two possible explanations. The first one is the increase of peak traction of the cohesive law and the second one is the resulting decrease in area under the softening part of the cohesive law. Now, as θ also creates the latter effect, but the difference in the occurrence of stick-slip is less pronounced for varying values of θ (Figure 42), it cannot be the sole factor that explains the increase in stick-slip events. The increase in maximal stress must contribute as well. Essentially, the increase in peak traction creates a localization of the detachment of elements, while at low peak stresses a larger part of the pad length will be activated.

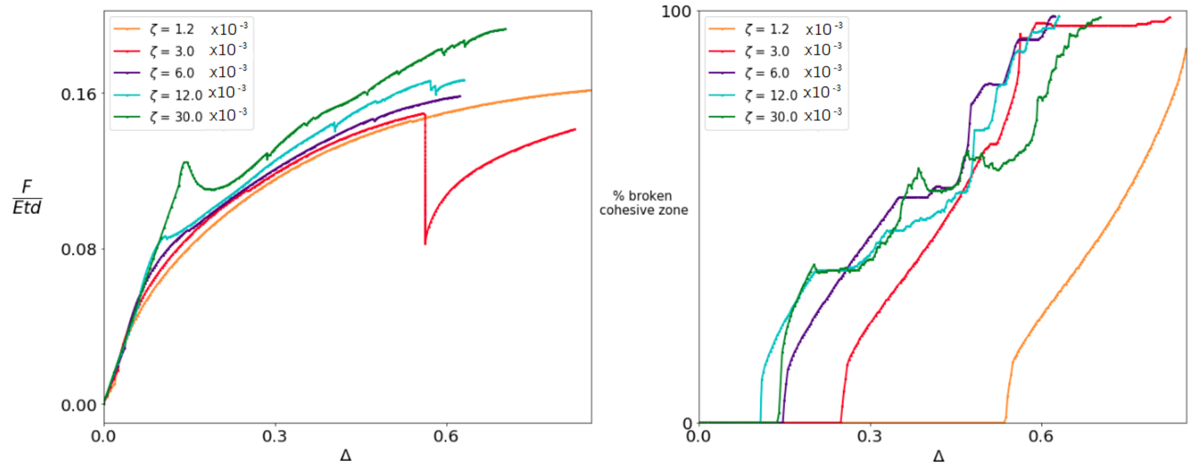

Figure 43: Force-displacement (left) and percentage of failure-displacement (right) graphs for pads with as only different parameter ζ. The force is the total pulling force in the X-direction that needs to be exerted upon the pulling end of the backing to pull this end the amount of displacement imposed. Note that the large drop in the force near the end of the simulation in the red curve is a non-physical mesh effect and can be disregarded, as explained in the convergence analysis in Appendix C.2.

Figure 44 shows the normalized horizontal displacement at the pad surface (left) and vertical displacement at the pad surface (middle) and the attached and detached regions (right) along the pad length (x/L) for varying imposed displacements (Δ) for two different values of parameter ζ, all other values being equal.

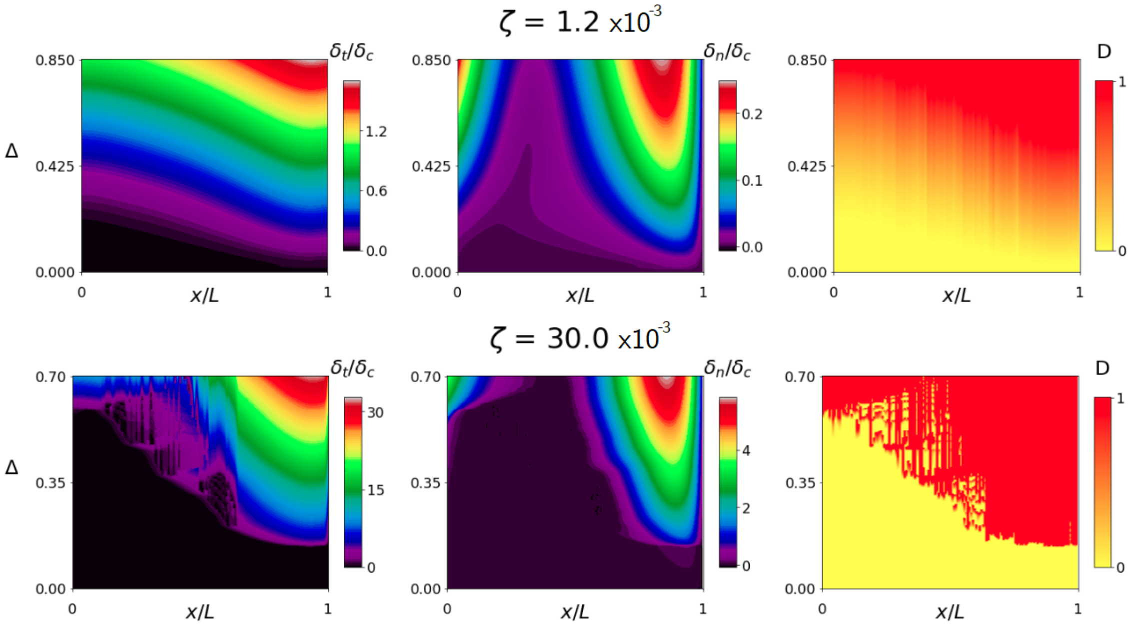

Figure 44: Detachment analysis of the surface of two pads with as only different parameter ζ. The amount of displacement is advanced over the y-axis and the pad length is advanced over the x-axis on each of the Figures. The left graphs show the opening of the adhesive surface in the tangential direction, the middle graphs the opening in the normal direction, and the right graphs the damage of the surface.

First, the right figure shows that indeed higher values of ζ are linked to reattachment events. Further, the right figure shows that the initiation of detachment happens at a lower displacement for a lower ζ, something we did not observe in Figure 41 for the variation of θ. This is linked to a lower energy under the elastic part of the cohesive law and a higher energy under the elastic part of the simulations with a lower ζ: elements will reach maximal stress faster and during the softening phase, more of the pad length will be activated as the elements' maximal stress value is lower. The result of this mechanism is also visible on the displacement graph on the left and the middle figure where both the tangential and normal opening are spread out more over the whole pad for lower values of ζ. This relates to the dissipation of energy and over a longer pad length, altering the distribution of internal stresses, spreading it over the whole pad, rather than to stay localized for the smaller value of ζ.

6.2 Occurrence of Stick-Slip

The observation of these energy transitions and mechanics responsible for the influence of the surface parameters, inspires a broader search of the effect of the variation of both parameters to characterize in which regions of the parameter space stick-slip will be observed. The corresponding phase-diagram for the variation of $\zeta = \frac{\sigma_c}{E}$ (y-axis) and $\theta = \frac{G_c}{Et}$ (x-axis) of the occurrence of stick-slip is shown in Figure 45. In the dark grey crosses stick-slip events were observed in the simulations, while the light grey crosses indicate no stick-slip observed in the simulations. The 'cohesive' law limit is the zone for which the elastic energy in the cohesive zone at the peak stress would become higher than the total energy (corresponding to a negative fracture energy for the softening area under the graph, which is physically impossible). The time limit is where simulations ran too long because of their long softening phases with large δ_c values: no result could be analyzed.

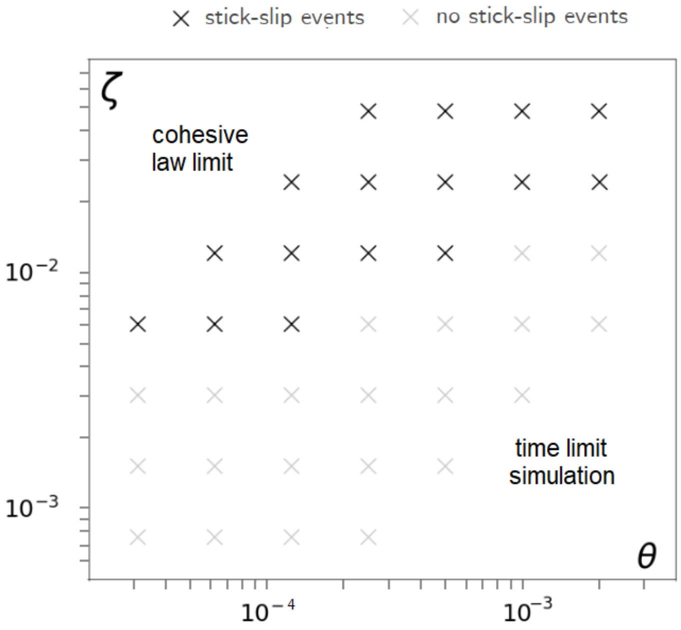

Figure 45: Diagram of occurrence of stick-slip in function of $\zeta = \frac{\sigma_c}{E}$ and $\theta = \frac{G_c}{Et}$. The dark grey crosses are simulations where stick-slip occurred and the light ones where stick-slip was absent. On the top left no simulations could be done, as $\delta_c < \delta_0$, while on the bottom left the long non-linear phases of the simulation caused the simulation to time out before it was finished. The stick-slip events are observed close to the cohesive law limit, i.e. when the softening phases are very short (low $\delta_c - \delta_0$) and snap-through behaviors are observed as well. For the development of this graph, one single event of stick-slip was ignored and only curve with consistently a large amount of stick-slip were marked as having stick-slip. Large non-physical drops and re-increases in force as discussed in Appendix C.2 were disregarded.

The phase-diagram shows that stick-slip occurs mostly for higher values of ζ, and secondly that the combination of a low θ and a high ζ favors the occurrence of stick-slip even more. This supports our earlier conclusion: stick-slip events are related mostly to higher maximal stresses of the adhesive surface, and even more if those are combined with steep, short softening phases. Steep refers to a more negative slope (induced by the higher maximal surface stress) and short refers to a smaller difference between δ_c and δ_0. The higher stress allows for the localization of the internal stresses (as discussed in Section 6.1.2), while the short softening phase (low δ_c) allows for the energy to be transferred into elastic energy (creating stress distributions) that will eventually cause reattachment. As the softening phase becomes longer and δ_c higher, the softening of other elements will modify their energy balance and no reattachment will occur. At the same time, if the softening phase is short, but the maximal stress (ζ) is low, the energy that is released during softening is too low to create the reattachment wave.

7 Conclusion and Perspectives

A finite element model was used to investigate the driving force for the detachment of a bi-layer adhesive pad under a zero-degree peeling test. The possibility of reattachment was included, based on a dedicated cohesive zone model. Following recent experimental observations of competing failure modes and stick-slip, the experimental behavior was very well captured by the simulations. The influence of material and geometrical parameters on the failure mode was explained and stick-slip was observed to occur for the same geometrical and material parameter ranges as in the experiments. The model was further exploited to investigate the physical range of the adhesive surface zone parameters.

Failure modes and occurrence of stick-slip. The development of this finite element model allowed not only to study the conditions under which the three different failure modes: interfacial cavitation, steady peeling, and curling, occur, but it also allowed to explain their mechanical origin, their driving force and the energetic exchanges responsible for their occurrence. It was shown that the stress distributions in the adhesive pad under the influence of the boundary conditions and of the interfacial failure are the driving force for the failure mechanism and for the stick-slip behavior. Interfacial cavitation and curling are linked to a high degree of build-up of pre-peak stresses of the surface, corresponding to a brittle, unstable behavior of the pad. Meanwhile, the steady peeling mode shows a more ductile force-displacement response, also being the only failure mode during which stick-slip is observed. To model this peeling mode correctly, reattachment is crucial.

Representing stick-slip and Schallamach waves with reversible cohesive elements. As no earlier finite element study of surface-surface sliding of a soft material of finite thickness over a rigid substrate was previously conducted for this type of stick-slip behavior, the relatively limited adaptation we deployed here to represent reattachment in the cohesive law can potentially be employed in future work in classical cohesive elements. Our work also showed that to correctly represent peeling under a zero-degree angle of adhesive, reattachment is crucial. The stick-slip is accompanied by Schallamach waves carrying the elastic deformation that cause the reattachment. The observation of stick-slip and Schallamach waves in a quasi-static simulation, suggests they could be prevalent in a larger extent of mechanical situations than first thought. Peeling simulations could be further exploited to investigate these waves in more depth. Future work could use the adaptation we propose here in any intrinsic cohesive zone model for the modeling of adhesive peeling under a zero-degree test, other peeling geometries such as torsion, or for other mechanical phenomena where stick-slip accompanied by Schallamach waves occurs.

Surface properties. Next, it was shown that both bulk properties and surface properties are of importance for the stress state of the adhesive. In this context, it needs to be remarked that the cohesive zone properties were assumed independent of the bulk properties. While surface properties can be indeed adapted with different techniques, for a non-altered soft adhesive, a certain set of natural surface properties are related to the bulk material as well, but this relation is still unknown. It was also remarked that reported experimental values of surface properties show a large variability, depending on production methods. We remark that the exact matching of failure force in the experiments and simulation might become possible if the physical surface properties are actually known. Two suggestions for future studies emerge. For future studies in the chemical field, exploring the relations between the bulk material and the surface properties of soft materials, could allow extending the results of simulations and analytical studies to a pad-optimization process. For experimental studies on soft materials, a study on the production-method variability analysis of the adhesive surface properties, would allow for more exact numerical comparisons between theory or numerical model and reality.

Cohesive law shape. Regarding the cohesive zone properties, it was shown that stick-slip events are promoted in parameter ranges where the cohesive zone has a relatively high failure stress and a low cohesive energy under the softening part of the cohesive law. As stick-slip is also observed in experiments, this suggests that the cohesive law with high peak stresses and a limited softening will provide numerical results close to reality. For future numerical studies, we suggest using this type of law.

Perspectives. The assumptions included in the simulation are the use of the neo-Hookean material law instead of a visco-elastic rate-dependent law, the not exact matching of incompressible properties, the consideration of only the quasi-static case rather than a full dynamic case, and the approximation of the system by a two-dimensional simulation. Further, this adaptation of the cohesive law does not allow to represent the forces in the stiff substrate well. As discussed in the introduction, it was also recently suggested that an adhesive reattachment force is already acting on the sample before it comes into contact with the surface, while this study only considers reattachment once adhesive and rigid surface come into full contact. Future studies might explore the significance of these assumptions on the simulation results. There is especially an interest in exploring the inclusion of rate-dependent behavior, as this could potentially allow modeling the snap-through behaviors dynamically and explore the physics happening during this phase.

Impact on the state of the art. Soft adhesives have long been of great interest, as they show a superior capacity to re-adhere. Their behavior has been widely studied, experimentally, analytically, and in finite element simulations. However, a large part of the physics responsible for their detachment behavior is still not fully understood. In particular, stick-slip behavior where the pad detaches and reattaches, corresponding to a drop and re-increase in the force-displacement curve, has been experimentally observed and partially analytically explained, but so far finite element simulations have not been able to capture the phase after reattachment. Recently, formulations coupling friction and adhesion to deal with this have emerged. Until now, their focus has been on the sliding of a sphere or cylinder over a surface, either the surface or sphere/cylinder being a soft adhesive and the other a stiff substrate. The representation of stick-slip behavior and the accompanying Schallamach waves have not earlier been investigated. In this study, we managed to capture this behavior and obtain very good correspondence with the experiments. The finite element model allows explaining the mechanics underlying the failure and reattachment mechanisms, and explores the variability of the surface properties. The fundamental mechanics that are the driving force for the stick-slip, suggest that Schallamach waves could be more omnipresent over different length scales than originally thought. In particular, in the field of earthquake engineering for the study of tectonic plate sliding, this has been suggested already [Ronsin et al., 2011, Galeano et al., 2000, Festa et al., 2010, Uenishi and Rice, 2003]. More generally, the sliding of any soft surface over a rigid surface that is gradually loaded could exhibit the same kind of behavior. Moreover, the adaptation to the cohesive law proposed here is implementable in any intrinsic cohesive law with limited adaptations.

References

Rohan Abeyaratne. *Continuum Mechanics: Volume II of Lecture Notes on the Mechanics of Solids*, volume 2. Electronic Publication, Cambridge, MA 02139-4307, USA, 1 edition, 7 1988. ISBN 978-0-9791865-1-6. `http://web.mit.edu/abeyaratne/Volumes/RCA_Vol_II.pdf` [Accessed: 2020].

J. Ahrens, Berk Geveci, and Charles Law. Paraview: An end-user tool for large data visualization. *Visualization Handbook*, 01 2005.

Ammar A. Alsheghri and Rashid K. Abu Al-Rub. Thermodynamic-based cohesive zone healing model for self-healing materials. *Mechanics Research Communications*, 70:102 – 113, 2015. ISSN 0093-6413. doi: https://doi.org/10.1016/j.mechrescom.2015.10.003.

Ammar A. Alsheghri and Rashid K. Abu Al-Rub. Finite element implementation and application of a cohesive zone damage-healing model for self-healing materials. *Engineering Fracture Mechanics*, 163:1 – 22, 2016. ISSN 0013-7944. doi: https://doi.org/10.1016/j.engfracmech.2016.06.010.

Nicolas Amouroux, Jérôme Petit, and Liliane Léger. Role of interfacial resistance to shear stress on adhesive peel strength. *Langmuir*, 17(21):6510–6517, Oct 2001. ISSN 0743-7463. doi: 10.1021/la010146r.

Konstantinos N. Anyfantis and Nicholas G. Tsouvalis. A novel traction–separation law for the prediction of the mixed mode response of ductile adhesive joints. *International Journal of Solids and Structures*, 49(1): 213 – 226, 2012. ISSN 0020-7683. doi: https://doi.org/10.1016/j.ijsolstr.2011.10.001.

K Autumn, A Dittmore, D Santos, M Spenko, and M Cutkosky. Frictional adhesion: A new angle on gecko attachment. *The Journal of experimental biology*, 209(Pt 18):3569—3579, September 2006. ISSN 0022-0949. doi: 10.1242/jeb.02486.

Kellar Autumn, Metin Sitti, Yiching A. Liang, Anne M. Peattie, Wendy R. Hansen, Simon Sponberg, Thomas W. Kenny, Ronald Fearing, Jacob N. Israelachvili, and Robert J. Full. Evidence for van der waals adhesion in gecko setae. *Proceedings of the National Academy of Sciences*, 99(19):12252–12256, 2002. ISSN 0027-8424. doi: 10.1073/pnas.192252799.

Utkarsh Ayachit. *The ParaView Guide: A Parallel Visualization Application*. Kitware, Inc., USA, 2015. ISBN 1930934300, 9781930934306.

Sangyul Baik, Heon Joon Lee, Da Wan Kim, Ji Won Kim, Youngkwan Lee, and Changhyun Pang. Bioinspired adhesive architectures: From skin patch to integrated bioelectronics. *Advanced Materials*, 31(34):1803309, 2019. doi: 10.1002/adma.201803309.

E. Barthel and G. Haiat. Approximate model for the adhesive contact of viscoelastic spheres. *Langmuir*, 18 (24):9362–9370, 2002. doi: 10.1021/la025959+.

Michael D. Bartlett, Andrew B. Croll, Daniel R. King, Beth M. Paret, Duncan J. Irschick, and Alfred J. Crosby. Looking beyond fibrillar features to scale gecko-like adhesion. *Advanced Materials*, 24(8):1078–1083, 2012. doi: 10.1002/adma.201104191.

T. Baumberger, C. Caroli, and O. Ronsin. Self-healing slip pulses and the friction of gelatin gels. *The European Physical Journal E*, 11(1):85–93, May 2003. ISSN 1292-8941. doi: 10.1140/epje/i2003-10009-7.

Tristan Baumberger, Christiane Caroli, and Olivier Ronsin. Self-healing slip pulses along a gel glass interface. *Phys. Rev. Lett.*, 88:075509, Feb 2002. doi: 10.1103/PhysRevLett.88.075509.

Matthew R. Begley, Rachel R. Collino, Jacob N. Israelachvili, and Robert M. McMeeking. Peeling of a tape with large deformations and frictional sliding. *Journal of the Mechanics and Physics of Solids*, 61(5):1265 – 1279, 2013. ISSN 0022-5096. doi: https://doi.org/10.1016/j.jmps.2012.09.014.

A. Biel and U. Stigh. Cohesive zone modelling of nucleation, growth and coalesce of cavities. *International Journal of Fracture*, 204(2):159–174, Apr 2017. ISSN 1573-2673. doi: 10.1007/s10704-016-0168-9.

Guido Borino and Francesco Parrinello. Multiple surface cracking and debonding failure for thin thermal coatings. *Procedia Structural Integrity*, 18:866 – 874, 2019. ISSN 2452-3216. doi: https://doi.org/10.1016/j.prostr.2019.08.237. 25th International Conference on Fracture and Structural Integrity.

Silviya Boyadzhieva, Katharina Sorg, Martin Danner, Sarah C. L. Fischer, René Hensel, Bernhard Schick, Gentiana Wenzel, Eduard Arzt, and Klaus Kruttwig. A self-adhesive elastomeric wound scaffold for sensitive adhesion to tissue. *Polymers*, 11(6), 2019. ISSN 2073-4360. doi: 10.3390/polym11060942.

F. Brochard-Wyart and P.-G. de Gennes. Naive model for stick-slip processes. *The European Physical Journal E*, 23(4):439–444, Aug 2007. ISSN 1292-895X. doi: 10.1140/epje/i2007-10215-3.

D Brodoceanu, C T Bauer, E Kroner, E Arzt, and T Kraus. Hierarchical bioinspired adhesive surfaces—a review. *Bioinspiration & Biomimetics*, 11(5):051001, aug 2016. doi: 10.1088/1748-3190/11/5/051001.

G.T. Camacho and M. Ortiz. Computational modelling of impact damage in brittle materials. *International Journal of Solids and Structures*, 33(20):2899 – 2938, 1996. ISSN 0020-7683. doi: https://doi.org/10.1016/0020-7683(95)00255-3.

R.D.S.G. Campilho, M.D. Banea, J.A.B.P. Neto, and L.F.M. da Silva. Modelling adhesive joints with cohesive zone models: effect of the cohesive law shape of the adhesive layer. *International Journal of Adhesion and Adhesives*, 44:48 – 56, 2013. ISSN 0143-7496. doi: https://doi.org/10.1016/j.ijadhadh.2013.02.006.

Q. H. Cheng, B. Chen, H. J. Gao, and Y. W. Zhang. Sliding-induced non-uniform pre-tension governs robust and reversible adhesion: a revisit of adhesion mechanisms of geckos. *Journal of The Royal Society Interface*, 9(67):283–291, 2012. doi: 10.1098/rsif.2011.0254.

Kilwon Cho, Daeho Lee, Tae Oan Ahn, Kyung Hoon Seo, and Han Mo Jeong. Adhesion behavior of pdms-containing polyimide to glass. *Journal of Adhesion Science and Technology*, 12(3):253–269, 1998. doi: 10.1163/156856198X00867.

Julien Chopin, Richard Villey, David Yarusso, Etienne Barthel, Costantino Creton, and Matteo Ciccotti. Nonlinear viscoelastic modeling of adhesive failure for polyacrylate pressure-sensitive adhesives. *Macromolecules*, 51(21):8605–8610, Nov 2018. ISSN 0024-9297. doi: 10.1021/acs.macromol.8b01374.

Marius Cocou, Mathieu Schryve, and Michel Raous. A dynamic unilateral contact problem with adhesion and friction in viscoelasticity. *Zeitschrift für angewandte Mathematik und Physik*, 61(4):721–743, Aug 2010. ISSN 1420-9039. doi: 10.1007/s00033-009-0027-x.

Tal Cohen, Chon U Chan, and L. Mahadevan. Competing failure modes in finite adhesive pads. *Soft Matter*, 14(10):1771–1779, 2018. ISSN 1744-683X, 1744-6848. doi: 10.1039/C7SM02378B.

Rachel R. Collino, Noah R. Philips, Michael N. Rossol, Robert M. McMeeking, and Matthew R. Begley. Detachment of compliant films adhered to stiff substrates via van der waals interactions: role of frictional sliding during peeling. *Journal of The Royal Society Interface*, 11(97):20140453, 2014. doi: 10.1098/rsif.2014.0453.

William M. Coombs, Tim J. Charlton, Michael Cortis, and Charles E. Augarde. Overcoming volumetric locking in material point methods. *Computer Methods in Applied Mechanics and Engineering*, 333:1 – 21, 2018. ISSN 0045-7825. doi: https://doi.org/10.1016/j.cma.2018.01.010.

Pierre-Philippe Cortet, Matteo Ciccotti, and Loïc Vanel. Imaging the stick-slip peeling of an adhesive tape under a constant load. *Journal of Statistical Mechanics Theory and Experiment*, 2007, 03 2007. doi: 10.1088/1742-5468/2007/03/P03005.

Pierre-Philippe Cortet, Marie-Julie Dalbe, Claudia Guerra, Caroline Cohen, Matteo Ciccotti, Stéphane Santucci, and Loïc Vanel. Intermittent stick-slip dynamics during the peeling of an adhesive tape from a roller. *Phys. Rev. E*, 87:022601, Feb 2013. doi: 10.1103/PhysRevE.87.022601.

Costantino Creton and Matteo Ciccotti. Fracture and adhesion of soft materials: a review. *Reports on Progress in Physics*, 79(4):046601, mar 2016. doi: 10.1088/0034-4885/79/4/046601.

Andrew B. Croll, Nasibeh Hosseini, and Michael D. Bartlett. Switchable adhesives for multifunctional interfaces. *Advanced Materials Technologies*, 4(8):1900193, 2019. doi: 10.1002/admt.201900193.

Marie-Julie Dalbe, Pierre-Philippe Cortet, Matteo Ciccotti, Loic Vanel, and Stéphane Santucci. Multiscale stick-slip dynamics of adhesive tape peeling. *Physical Review Letters*, 115, 09 2015. doi: 10.1103/PhysRevLett.115.128301.

Saurabh Das, Sathya Chary, Jing Yu, John Tamelier, Kimberly L. Turner, and Jacob N. Israelachvili. Jkr theory for the stick–slip peeling and adhesion hysteresis of gecko mimetic patterned surfaces with a smooth glass surface. *Langmuir*, 29(48):15006–15012, Dec 2013. ISSN 0743-7463. doi: 10.1021/la403420f.

René de Borst and Clemens V. Verhoorsel. Damage, material instabilities and failure. In Ltd. John Wiley & Sons, editor, *Encyclopedia of Computational Mechanics Second Edition*, page 50. John Wiley & Sons Ltd., 2017.

Audelia G. Dharmawan, Priti Xavier, Hassan H. Hariri, Gim Song Soh, Avinash Baji, Roland Bouffanais, Shaohui Foong, Hong Yee Low, and Kristin L. Wood. Design, Modeling, and Experimentation of a Bio-Inspired Miniature Climbing Robot With Bilayer Dry Adhesives. *Journal of Mechanisms and Robotics*, 11 (2), 02 2019. ISSN 1942-4302. doi: 10.1115/1.4042457. 020902.

R. Dimitri, M. Trullo, L. De Lorenzis, and G. Zavarise. Coupled cohesive zone models for mixed-mode fracture: A comparative study. *Engineering Fracture Mechanics*, 148:145 – 179, 2015. ISSN 0013-7944. doi: https://doi.org/10.1016/j.engfracmech.2015.09.029.

John Dolbow and Ted Belytschko. Volumetric locking in the element free galerkin method. *International Journal for Numerical Methods in Engineering*, 46(6):925–942, 1999. doi: 10.1002/(SICI)1097-0207(19991030)46:6<925::AID-NME729>3.0.CO;2-Y.

Jeffrey Eisenhaure and Seok Kim. A review of the state of dry adhesives: Biomimetic structures and the alternative designs they inspire. *Micromachines*, 8(4):125, Apr 2017. ISSN 2072-666X. doi: 10.3390/mi8040125.

Jeffrey Eisenhaure and Seok Kim. High-strain shape memory polymers as practical dry adhesives. *International Journal of Adhesion and Adhesives*, 81:74 – 78, 2018. ISSN 0143-7496. doi: https://doi.org/10.1016/j.ijadhadh.2017.11.008.

M. Elices, G.V. Guinea, J. Gómez, and J. Planas. The cohesive zone model: advantages, limitations and challenges. *Engineering Fracture Mechanics*, 69(2):137 – 163, 2002. ISSN 0013-7944. doi: https://doi.org/10.1016/S0013-7944(01)00083-2.

Walter Federle and David Labonte. Dynamic biological adhesion: mechanisms for controlling attachment during locomotion. *Philosophical Transactions of the Royal Society B: Biological Sciences*, 374(1784): 20190199, 2019. doi: 10.1098/rstb.2019.0199.

Lorena M. Fernández-Cañadas, Inés Iváñez, and Sonia Sanchez-Saez. Influence of the cohesive law shape on the composite adhesively-bonded patch repair behaviour. *Composites Part B: Engineering*, 91:414 – 421, 2016. ISSN 1359-8368. doi: https://doi.org/10.1016/j.compositesb.2016.01.056.

Gaetano Festa, Jean-Pierre Vilotte, Michel Raous, and Carole Henninger. Scale-Dependent Friction and Damage Interface law: implications for effective earthquake rupture dynamics and radiation. In *EGU General Assembly Conference Abstracts*, EGU General Assembly Conference Abstracts, page 11647, May 2010.

Toshinori Fujie, Noriyuki Matsutani, Manabu Kinoshita, Yosuke Okamura, Akihiro Saito, and Shinji Takeoka. Adhesive, flexible, and robust polysaccharide nanosheets integrated for tissue-defect repair. *Advanced Functional Materials*, 19(16):2560–2568, 2009. doi: 10.1002/adfm.200900103.

Y. Fukahori, P. Gabriel, and J.J.C. Busfield. How does rubber truly slide between schallamach waves and stick–slip motion? *Wear*, 269(11):854 – 866, 2010. ISSN 0043-1648. doi: https://doi.org/10.1016/j.wear.2010.08.016.

P. Gabriel, Y. Fukahori, A. G. Thomas, and J. J. C. Busfield. FEA MODELING OF SCHALLAMACH WAVES. *Rubber Chemistry and Technology*, 83(4):358–367, 12 2010. ISSN 0035-9475. doi: 10.5254/1.3481697.

J Galeano, P Español, and M. A Rubio. Experimental and theoretical results of stress relaxations in a model of earthquake dynamics. *Europhysics Letters (EPL)*, 49(4):410–416, feb 2000. doi: 10.1209/epl/i2000-00164-y.

A. Galliano, S. Bistac, and J. Schultz. Adhesion and friction of pdms networks: molecular weight effects. *Journal of Colloid and Interface Science*, 265(2):372 – 379, 2003. ISSN 0021-9797. doi: https://doi.org/10.1016/S0021-9797(03)00458-2.

Kevin C. Galloway, Kaitlyn P. Becker, Brennan Phillips, Jordan Kirby, Stephen Licht, Dan Tchernov, Robert J. Wood, and David F. Gruber. Soft robotic grippers for biological sampling on deep reefs. *Soft Robotics*, 3 (1):23–33, 2016. doi: 10.1089/soro.2015.0019.

Huajian Gao, Xiang Wang, Haimin Yao, Stanislav Gorb, and Eduard Arzt. Mechanics of hierarchical adhesion structures of geckos. *Mechanics of Materials*, 37(2):275 – 285, 2005. ISSN 0167-6636. doi: https://doi.org/10.1016/j.mechmat.2004.03.008. New Directions in Mechanics and Selected Articles in Micromechanics of Materials.

Ravinu Garg and Naresh V Datla. Peeling of heterogeneous thin films: Effect of bending stiffness, adhesion energy, and level of heterogeneity. *The Journal of Adhesion*, 95(3):169–186, 2019. doi: 10.1080/00218464.2017.1396215.

AK Geim, SV Dubonos, IV Grigorieva, KS Novoselov, AA Zhukov, and S Yu Shapoval. Microfabricated adhesive mimicking gecko foot-hair. *Nature materials*, 2(7):461—463, July 2003. ISSN 1476-1122. doi: 10.1038/nmat917.

Eric Gerde and M. Marder. Friction and fracture. *Nature*, 413(6853):285–288, Sep 2001. ISSN 1476-4687. doi: 10.1038/35095018.

Christophe Geuzaine and Jean-François Remacle. Gmsh: A 3-d finite element mesh generator with built-in pre- and post-processing facilities. *International Journal for Numerical Methods in Engineering*, 79:1309 – 1331, 09 2009. doi: 10.1002/nme.2579.

Ana M. Girão Coelho. Finite element guidelines for simulation of delamination dominated failures in composite materials validated by case studies. *Archives of Computational Methods in Engineering*, 23(2):363–388, Jun 2016. ISSN 1886-1784. doi: 10.1007/s11831-015-9144-1.

Saipraneeth Gouravaraju, Roger A. Sauer, and Sachin Singh Gautam. On the presence of a critical detachment angle in gecko spatula peeling - a numerical investigation using an adhesive friction model. *The Journal of Adhesion*, 0(0):1–21, 2020. doi: 10.1080/00218464.2020.1746652.

Mark W. Grinstaff. Designing hydrogel adhesives for corneal wound repair. *Biomaterials*, 28(35):5205 – 5214, 2007. ISSN 0142-9612. doi: https://doi.org/10.1016/j.biomaterials.2007.08.041.

Zhen Gu, Siheng Li, Feilong Zhang, and Shutao Wang. Understanding surface adhesion in nature: A peeling model. *Advanced Science*, 3(7):1500327, 2016. doi: 10.1002/advs.201500327.

Jingyi Guo. *Constitutive Modeling and Fracture Mechanics of a Self-Healing Hydrogel with Chemical and Physical Cross-Links*. PhD thesis, Cornell, 2019.

Martin D. Hager. *Self-healing Materials*, chapter 9, pages 201–225. American Cancer Society, 2017. ISBN 9783527691036. doi: 10.1002/9783527691036.hsscvol6016.

F. L. Hammond, R. K. Kramer, Q. Wan, R. D. Howe, and R. J. Wood. Soft tactile sensor arrays for force feedback in micromanipulation. *IEEE Sensors Journal*, 14(5):1443–1452, 2014.

Liwen He, Jia Lou, Sritawat Kitipornchai, Jie Yang, and Jianke Du. Peeling mechanics of hyperelastic beams: Bending effect. *International Journal of Solids and Structures*, 167:184 – 191, 2019a. ISSN 0020-7683. doi: https://doi.org/10.1016/j.ijsolstr.2019.03.011.

Xiaocong He. A review of finite element analysis of adhesively bonded joints. *International Journal of Adhesion and Adhesives*, 31(4):248 – 264, 2011. ISSN 0143-7496. doi: https://doi.org/10.1016/j.ijadhadh.2011.01.006.

Yiqian He, Di Zuo, Klaus Hackl, Haitian Yang, S. Jamaleddin Mousavi, and Stéphane Avril. Gradient-enhanced continuum models of healing in damaged soft tissues. *Biomechanics and Modeling in Mechanobiology*, 18 (5):1443–1460, Oct 2019b. ISSN 1617-7940. doi: 10.1007/s10237-019-01155-z.

Thomas H. Heaton. Evidence for and implications of self-healing pulses of slip in earthquake rupture. *Physics of the Earth and Planetary Interiors*, 64(1):1 – 20, 1990. ISSN 0031-9201. doi: https://doi.org/10.1016/0031-9201(90)90002-F.

M. Heidari-Rarani and A.R. Ghasemi. Appropriate shape of cohesive zone model for delamination propagation in enf specimens with r-curve effects. *Theoretical and Applied Fracture Mechanics*, 90:174 – 181, 2017. ISSN 0167-8442. doi: https://doi.org/10.1016/j.tafmec.2017.04.009.

Ismail Honsali. Propagation of peeling finite adhesive pads. Master's thesis, Ecole Polytechnique Federale de Lausanne, 2018.

Jen-Hsuan Hsiao, Jen-Yuan (James) Chang, and Chao-Min Cheng. Soft medical robotics: clinical and biomedical applications, challenges, and future directions. *Advanced Robotics*, 33(21):1099–1111, 2019. doi: 10.1080/01691864.2019.1679251.

Nguyen-Xuan Hung, Stéphane Pierre Alain Bordas, and Nguyen-Dang Hung. Addressing volumetric locking and instabilities by selective integration in smoothed finite elements. *Communications in Numerical Methods in Engineering*, 25(1):19–34, 2009. doi: 10.1002/cnm.1098.

Anthony R. Ingraffea and René de Borst. Computational fracture mechanics. In Ltd. John Wiley & Sons, editor, *Encyclopedia of Computational Mechanics Second Edition*, page 26. John Wiley & Sons Ltd., 2017.

A. Jagota, S. J. Bennison, and C. A. Smith. Analysis of a compressive shear test for adhesion between elastomeric polymers and rigid substrates. *International Journal of Fracture*, 104(2):105–130, Jul 2000. ISSN 1573-2673. doi: 10.1023/A:1007617102311.

Anand Jagota and Chung-Yuen Hui. Adhesion, friction, and compliance of bio-mimetic and bio-inspired structured interfaces. *Materials Science and Engineering: R: Reports*, 72(12):253 – 292, 2011. ISSN 0927-796X. doi: https://doi.org/10.1016/j.mser.2011.08.001.

Etelvina Javierre. Modeling self-healing mechanisms in coatings: Approaches and perspectives. *Coatings*, 9 (2):122, Feb 2019. ISSN 2079-6412. doi: 10.3390/coatings9020122.

Jefferson, Anthony, Selvarajoo, Tharmesh, Freeman, Brubeck, and Davies, Robert. An experimental and numerical study on vascular self-healing cementitious materials. *MATEC Web Conf.*, 289:01004, 2019. doi: 10.1051/matecconf/201928901004.

K. L. Johnson. *Contact Mechanics*. Cambridge University Press, 1985. doi: 10.1017/CBO9781139171731.

M. Karimi, H. Bayesteh, and S. Mohammadi. An adapting cohesive approach for crack-healing analysis in sma fiber-reinforced composites. *Computer Methods in Applied Mechanics and Engineering*, 349:550 – 575, 2019. ISSN 0045-7825. doi: https://doi.org/10.1016/j.cma.2019.02.019.

M. Khajeh Salehani, N. Irani, and L. Nicola. Modeling adhesive contacts under mixed-mode loading. *Journal of the Mechanics and Physics of Solids*, 130:320 – 329, 2019. ISSN 0022-5096. doi: https://doi.org/10.1016/j.jmps.2019.06.010.

H. Khoramishad, M. Hamzenejad, and R.S. Ashofteh. Characterizing cohesive zone model using a mixed-mode direct method. *Engineering Fracture Mechanics*, 153:175 – 189, 2016. ISSN 0013-7944. doi: https://doi.org/10.1016/j.engfracmech.2015.10.045.

Tae Kyung Kim, Jeong Koo Kim, and Ok Chan Jeong. Measurement of nonlinear mechanical properties of pdms elastomer. *Microelectronic Engineering*, 88(8):1982 – 1985, 2011a. ISSN 0167-9317. doi: 10.1016/j.mee.2010.12.108. Proceedings of the 36th International Conference on Micro- and Nano-Engineering (MNE).

Tae Kyung Kim, Jeong Koo Kim, and Ok Chan Jeong. Measurement of nonlinear mechanical properties of pdms elastomer. *Microelectronic Engineering*, 88(8):1982 – 1985, 2011b. ISSN 0167-9317. doi: https://doi.org/10.1016/j.mee.2010.12.108. Proceedings of the 36th International Conference on Micro- and Nano-Engineering (MNE).

Wolfgang G. Knauss. A review of fracture in viscoelastic materials. *International Journal of Fracture*, 196(1): 99–146, Nov 2015. ISSN 1573-2673. doi: 10.1007/s10704-015-0058-6.

Jayaprakash Krishnasamy, Sathiskumar A. Ponnusami, Sergio Turteltaub, and Sybrand van der Zwaag. Modelling the fracture behaviour of thermal barrier coatings containing healing particles. *Materials & Design*, 157:75 – 86, 2018. ISSN 0264-1275. doi: https://doi.org/10.1016/j.matdes.2018.07.026.

G. J. Lake and A. Stevenson. Wave phenomena in low angle peeling. *The Journal of Adhesion*, 12(1):13–22, 1981. doi: 10.1080/00218468108071185.

Sung Ho Lee, Insol Hwang, Bong Su Kang, Hoon Eui Jeong, and Moon Kyu Kwak. Highly flexible and self-adaptive dry adhesive end-effectors for precision robotics. *Soft Matter*, 15:5827–5834, 2019. doi: 10.1039/C9SM00431A.

J. Lengiewicz, M. de Souza, M.A. Lahmar, C. Courbon, D. Dalmas, S. Stupkiewicz, and J. Scheibert. Finite deformations govern the anisotropic shear-induced area reduction of soft elastic contacts. *Journal of the Mechanics and Physics of Solids*, 143:104056, Oct 2020. ISSN 0022-5096. doi: 10.1016/j.jmps.2020.104056.

Tamran H. Lengyel, Yuan Qi, Peter Schiavone, and Rong Long. Interface crack between a compressible elastomer and a rigid substrate with finite slippage. *Journal of the Mechanics and Physics of Solids*, 90: 142 – 159, 2016. ISSN 0022-5096. doi: https://doi.org/10.1016/j.jmps.2016.02.006.

Yasong Li, Jeffrey Krahn, and Carlo Menon. Bioinspired dry adhesive materials and their application in robotics: A review. *Journal of Bionic Engineering*, 13(2):181 – 199, 2016. ISSN 1672-6529. doi: https://doi.org/10.1016/S1672-6529(16)60293-7.

Yu-Yun Lin and C. Y. Hui. Mechanics of contact and adhesion between viscoelastic spheres: An analysis of hysteresis during loading and unloading. *Journal of Polymer Science Part B: Polymer Physics*, 40(9): 772–793, 2002. doi: 10.1002/polb.10140.

Zezhou Liu, Helen Minsky, Costantino Creton, Matteo Ciccotti, and Chung-Yuen Hui. Mechanics of zero degree peel test on a tape — effects of large deformation, material nonlinearity, and finite bond length. *Extreme Mechanics Letters*, 32:100518, 2019. ISSN 2352-4316. doi: https://doi.org/10.1016/j.eml.2019.100518.

Satoru Maegawa and Ken Nakano. Mechanism of stick-slip associated with schallamach waves. *Wear*, 268 (7):924 – 930, 2010. ISSN 0043-1648. doi: https://doi.org/10.1016/j.wear.2009.12.018.

Satoru Maegawa, Fumihiro Itoigawa, and Takashi Nakamura. Dynamics in sliding friction of soft adhesive elastomer: Schallamach waves as a stress-relaxation mechanism. *Tribology International*, 96:23 – 30, 2016. ISSN 0301-679X. doi: https://doi.org/10.1016/j.triboint.2015.11.034.

Spandan Maiti and Philippe H. Geubelle. Cohesive modeling of fatigue crack retardation in polymers: Crack closure effect. *Engineering Fracture Mechanics*, 73(1):22 – 41, 2006. ISSN 0013-7944. doi: https://doi.org/10.1016/j.engfracmech.2005.07.005.

G. Marckmann and E. Verron. Comparison of hyperelastic models for rubber-like materials. *Rubber Chemistry and Technology*, 79(5):835–858, 2006. doi: 10.5254/1.3547969.

P. A. L. S. Martins, R. M. Natal Jorge, and A. J. M. Ferreira. A comparative study of several material models for prediction of hyperelastic properties: Application to silicone-rubber and soft tissues. *Strain*, 42 (3):135–147, 2006. doi: 10.1111/j.1475-1305.2006.00257.x.

Luthfi M. Mauludin, Xiaoying Zhuang, and Timon Rabczuk. Computational modeling of fracture in encapsulation-based self-healing concrete using cohesive elements. *Composite Structures*, 196:63 – 75, 2018. ISSN 0263-8223. doi: https://doi.org/10.1016/j.compstruct.2018.04.066.

J. Patrick McGarry, Eamonn O Mairtin, Guillaume Parry, and Glenn E. Beltz. Potential-based and non-potential-based cohesive zone formulations under mixed-mode separation and over-closure. part i: Theoretical analysis. *Journal of the Mechanics and Physics of Solids*, 63:336 – 362, 2014. ISSN 0022-5096. doi: https://doi.org/10.1016/j.jmps.2013.08.020.

Edvin Memet, Feodor Hilitski, Zvonimir Dogic, and L. Mahadevan. Static adhesion hysteresis in elastic structures, 2020.

C. Menon, M. Murphy, and M. Sitti. Gecko inspired surface climbing robots. In *2004 IEEE International Conference on Robotics and Biomimetics*, pages 431–436, Aug 2004. doi: 10.1109/ROBIO.2004.1521817.

Janine C. Mergel, Riad Sahli, Julien Scheibert, and Roger A. Sauer. Continuum contact models for coupled adhesion and friction. *The Journal of Adhesion*, 95(12):1101–1133, 2019. doi: 10.1080/00218464.2018.1479258.

Janine C. Mergel, Julien Scheibert, and Roger A. Sauer. Contact with coupled adhesion and friction: Computational framework, applications, and new insights, 2020.

Nachiketa Mishra, Nigam Chandra Parida, and Soumyendu Raha. Time scales of the stick slip dynamics of the peeling of an adhesive tape. *Proceedings of the Royal Society A: Mathematical, Physical and Engineering Sciences*, 471(2174):20140399, 2015a. doi: 10.1098/rspa.2014.0399.

Nachiketa Mishra, Nigam Chandra Parida, and Soumyendu Raha. Time scales of the stick–slip dynamics of the peeling of an adhesive tape. *Proceedings of the Royal Society A: Mathematical, Physical and Engineering Sciences*, 471(2174):20140399, Feb 2015b. ISSN 1471-2946. doi: 10.1098/rspa.2014.0399.

A. Mitchell and David Griffiths. *The Finite Difference Method in Partial Differential Equations*. Wiley, 01 1980.

Idris Mohammed, Maria Charalambides, and Anthony Kinloch. Modelling the peeling of a pressure sensitive adhesive film using cohesive zones. *ResearchGate*, 03 2013.

Idris K. Mohammed, Anthony J. Kinloch, and Maria N. Charalambides. Modelling the peeling behavior of soft adhesives. *Procedia Structural Integrity*, 2:326 – 333, 2016. ISSN 2452-3216. doi: https://doi.org/10.1016/j.prostr.2016.06.042. 21st European Conference on Fracture, ECF21, 20-24 June 2016, Catania, Italy.

Ahmad R. Mojdehi, Douglas P. Holmes, and David A. Dillard. Revisiting the generalized scaling law for adhesion: role of compliance and extension to progressive failure. *Soft Matter*, 13:7529–7536, 2017a. doi: 10.1039/C7SM01098B.

Ahmad R. Mojdehi, Douglas P. Holmes, and David A. Dillard. Friction of extensible strips: An extended shear lag model with experimental evaluation. *International Journal of Solids and Structures*, 124:125 – 134, 2017b. ISSN 0020-7683. doi: https://doi.org/10.1016/j.ijsolstr.2017.06.021.

Rabibrata Mukherjee and Ashutosh Sharma. Instability, self-organization and pattern formation in thin soft films. *Soft Matter*, 11:8717–8740, 2015. doi: 10.1039/C5SM01724F.

Angelina Müller, Matthias C. Wapler, and Ulrike Wallrabe. A quick and accurate method to determine the poisson's ratio and the coefficient of thermal expansion of pdms. *Soft Matter*, 15:779–784, 2019. doi: 10.1039/C8SM02105H.

Ken Nakano and Satoru Maegawa. Stick-slip in sliding systems with tangential contact compliance. *Tribology International*, 42(11):1771 – 1780, 2009. ISSN 0301-679X. doi: https://doi.org/10.1016/j.triboint.2009.04.039. Special Issue: 35th Leeds-Lyon Symposium.

Hadi Noori, Mukesh Jain, Kent Nielsen, and Frank Brandys. Significance of peel test speed on interface strength in cohesive zone modeling. *The Journal of Adhesion*, 92(1):39–51, 2016. doi: 10.1080/00218464.2014.993755.

M. Ortiz and A. Pandolfi. Finite-deformation irreversible cohesive elements for three-dimensional crack-propagation analysis. *International Journal for Numerical Methods in Engineering*, 44(9):1267–1282, 1999. doi: 10.1002/(SICI)1097-0207(19990330)44:9<1267::AID-NME486>3.0.CO;2-7.

Chahmi Oucif and Luthfi Mauludin. Continuum damage-healing and super healing mechanics in brittle materials: A state-of-the-art review. *Applied Sciences*, 8(12):2350, Nov 2018. ISSN 2076-3417. doi: 10.3390/app8122350.

Shingo Ozaki, Toshio Osada, and Wataru Nakao. Finite element analysis of the damage and healing behavior of self-healing ceramic materials. *International Journal of Solids and Structures*, 100-101:307 – 318, 2016. ISSN 0020-7683. doi: https://doi.org/10.1016/j.ijsolstr.2016.08.026.

Veli Ozbolat, Madhuri Dey, Bugra Ayan, Adomas Povilianskas, Melik C. Demirel, and Ibrahim T. Ozbolat. 3d printing of pdms improves its mechanical and cell adhesion properties. *ACS Biomaterials Science and Engineering*, 4(2):682–693, February 2018. ISSN 2373-9878. doi: 10.1021/acsbiomaterials.7b00646.

R. D. O'Rorke, T. W. J. Steele, and H. K. Taylor. Bioinspired fibrillar adhesives: a review of analytical models and experimental evidence for adhesion enhancement by surface patterns. *Journal of Adhesion Science and Technology*, 30(4):362–391, 2016. doi: 10.1080/01694243.2015.1101183.

Xia-Hui Pan, Shi-Qing Huang, Shou-Wen Yu, and Xi-Qiao Feng. Interfacial slippage effect on the surface instability of a thin elastic film under van der waals force. *Journal of Physics D: Applied Physics*, 42(5): 055302, feb 2009. doi: 10.1088/0022-3727/42/5/055302.

A. Papangelo and M. Ciavarella. On mixed-mode fracture mechanics models for contact area reduction under shear load in soft materials. *Journal of the Mechanics and Physics of Solids*, 124:159 – 171, 2019. ISSN 0022-5096. doi: https://doi.org/10.1016/j.jmps.2018.10.011.

Kyoungsoo Park and Glaucio H. Paulino. Cohesive Zone Models: A Critical Review of Traction-Separation Relationships Across Fracture Surfaces. *Applied Mechanics Reviews*, 64(6), 02 2013. ISSN 0003-6900. doi: 10.1115/1.4023110. 060802.

Kyoungsoo Park, Glaucio H. Paulino, and Jeffery R. Roesler. A unified potential-based cohesive model of mixed-mode fracture. *Journal of the Mechanics and Physics of Solids*, 57(6):891 – 908, 2009. ISSN 0022-5096. doi: https://doi.org/10.1016/j.jmps.2008.10.003.

Zhilong Peng and Shaohua Chen. Effect of bending stiffness on the peeling behavior of an elastic thin film on a rigid substrate. *Phys. Rev. E*, 91:042401, Apr 2015. doi: 10.1103/PhysRevE.91.042401.

Zhilong Peng, Hanbin Yin, Yin Yao, and Shaohua Chen. Effect of thin-film length on the peeling behavior of film-substrate interfaces. *Phys. Rev. E*, 100:032804, Sep 2019. doi: 10.1103/PhysRevE.100.032804.

Noshir S. Pesika, Yu Tian, Boxin Zhao, Kenny Rosenberg, Hongbo Zeng, Patricia McGuiggan, Kellar Autumn, and Jacob N. Israelachvili. Peel-zone model of tape peeling based on the gecko adhesive system. *The Journal of Adhesion*, 83(4):383–401, 2007. doi: 10.1080/00218460701282539.

J.-M. Piau, G. Ravilly, and C. Verdier. Peeling of polydimethylsiloxane adhesives at low velocities: Cohesive failure. *Journal of Polymer Science Part B: Polymer Physics*, 43(2):145–157, 2005. doi: 10.1002/polb.20318.

Suomi Ponce, José Bico, and Benoît Roman. Effect of friction on the peeling test at zero-degrees. *Soft Matter*, 11:9281–9290, 2015. doi: 10.1039/C5SM01203A.

Sathiskumar A. Ponnusami, Jayaprakash Krishnasamy, Sergio Turteltaub, and Sybrand van der Zwaag. A cohesive-zone crack healing model for self-healing materials. *International Journal of Solids and Structures*, 134:249 – 263, 2018. ISSN 0020-7683. doi: https://doi.org/10.1016/j.ijsolstr.2017.11.004.

Shabnam Raayai-Ardakani, Zhantao Chen, Darla Rachelle Earl, and Tal Cohen. Volume-controlled cavity expansion for probing of local elastic properties in soft materials. *Soft Matter*, 15:381–392, 2019. doi: 10.1039/C8SM02142B.

P. Rahulkumar, A. Jagota, S.J. Bennison, and S. Saigal. Cohesive element modeling of viscoelastic fracture: application to peel testing of polymers. *International Journal of Solids and Structures*, 37(13):1873 – 1897, 2000. ISSN 0020-7683. doi: https://doi.org/10.1016/S0020-7683(98)00339-4.

L.D.C. Ramalho, R.D.S.G. Campilho, J. Belinha, and L.F.M. da Silva. Static strength prediction of adhesive joints: A review. *International Journal of Adhesion and Adhesives*, 96:102451, 2020. ISSN 0143-7496. doi: https://doi.org/10.1016/j.ijadhadh.2019.102451.

Charles J. Rand and Alfred J. Crosby. Insight into the periodicity of schallamach waves in soft material friction. *Applied Physics Letters*, 89(26):261907, 2006. doi: 10.1063/1.2408640.

Michel Raous. Interface models coupling adhesion and friction. *Comptes Rendus Mécanique*, 339(7):491 – 501, 2011. ISSN 1631-0721. doi: https://doi.org/10.1016/j.crme.2011.05.007. Surface mechanics : facts and numerical models.

Giovanni Rateni, Matteo Cianchetti, Gastone Ciuti, Arianna Menciassi, and Cecilia Laschi. Design and development of a soft robotic gripper for manipulation in minimally invasive surgery: a proof of concept. *Meccanica*, 50(11):2855–2863, Nov 2015. ISSN 1572-9648. doi: 10.1007/s11012-015-0261-6.

N. Richart and J.F. Molinari. Implementation of a parallel finite-element library: Test case on a non-local continuum damage model. *Finite Elements in Analysis and Design*, 100:41–46, 2015. ISSN 0168-874X. doi: https://doi.org/10.1016/j.finel.2015.02.003.

Nicolas Richart. *Akantu - User's Guide*, 2016.

Jared Risan, Andrew B. Croll, and Fardad Azarmi. Compliance switching for adhesion control. *Journal of Polymer Science Part B: Polymer Physics*, 53(1):48–57, 2015. doi: 10.1002/polb.23624.

L. Roldán, J.J. Muñoz, and P. Sáez. Computational modeling of epithelial wound healing: Short and long term chemo-mechanical mechanisms. *Computer Methods in Applied Mechanics and Engineering*, 350:28 – 56, 2019. ISSN 0045-7825. doi: https://doi.org/10.1016/j.cma.2019.02.018.

O. Ronsin, T. Baumberger, and C. Y. Hui. Nucleation and propagation of quasi-static interfacial slip pulses. *The Journal of Adhesion*, 87(5):504–529, 2011. doi: 10.1080/00218464.2011.575342.

Rahul Sahay, Hong Yee Low, Avinash Baji, Shaohui Foong, and Kristin L. Wood. A state-of-the-art review and analysis on the design of dry adhesion materials for applications such as climbing micro-robots. *RSC Adv.*, 5:50821–50832, 2015. doi: 10.1039/C5RA06770G.

J.A. Sanz-Herrera, A. Aliko-Benitez, and A.M. Fadrique-Contreras. Numerical investigation of the coupled mechanical behavior of self-healing materials under cyclic loading. *International Journal of Solids and Structures*, 160:232 – 246, 2019. ISSN 0020-7683. doi: https://doi.org/10.1016/j.ijsolstr.2018.10.029.

Jayati Sarkar and Ashutosh Sharma. A unified theory of instabilities in viscoelastic thin films: From wetting to confined films, from viscous to elastic films, and from short to long waves. *Langmuir*, 26(11):8464–8473, 2010. doi: 10.1021/la9049007. PMID: 20205403.

Carlos Sarrado, Frank A. Leone, and Albert Turon. Finite-thickness cohesive elements for modeling thick adhesives. *Engineering Fracture Mechanics*, 168:105 – 113, 2016. ISSN 0013-7944. doi: https://doi.org/10.1016/j.engfracmech.2016.03.020. Modeling of fracture and damage in composite materials.

Roger A. Sauer. The peeling behavior of thin films with finite bending stiffness and the implications on gecko adhesion. *The Journal of Adhesion*, 87(7-8):624–643, 2011a. doi: 10.1080/00218464.2011.596084.

Roger A. Sauer. Enriched contact finite elements for stable peeling computations. *International Journal for Numerical Methods in Engineering*, 87(6):593–616, 2011b. doi: 10.1002/nme.3126.

Roger A. Sauer. Local finite element enrichment strategies for 2D contact computations and a corresponding post-processing scheme. *Computational Mechanics*, 52(2):301–319, August 2013. doi: 10.1007/s00466-012-0813-8.

Roger A. Sauer. A survey of computational models for adhesion. *The Journal of Adhesion*, 92(2):81–120, 2016. doi: 10.1080/00218464.2014.1003210.

A. Schallamach. How does rubber slide? *Wear*, 17(4):301 – 312, 1971. ISSN 0043-1648. doi: https://doi.org/10.1016/0043-1648(71)90033-0.

R.A. Schapery. A model for the prediction of rubber friction with schallamach waves. *Tribology International*, 143:106018, 2020. ISSN 0301-679X.

E. Serrano. Glued-in rods for timber structures—an experimental study of softening behaviour. *Materials and Structures*, 34(4):228–234, May 2001. ISSN 1871-6873. doi: 10.1007/BF02480593.

Jun Shintake, Vito Cacucciolo, Dario Floreano, and Herbert Shea. Soft robotic grippers. *Advanced Materials*, 30(29):1707035, 2018. doi: 10.1002/adma.201707035.

Ben H. Skopic and Hannes C. Schniepp. Peeling in biological and bioinspired adhesive systems. *JOM*, 72(4): 1509–1522, Apr 2020. ISSN 1543-1851. doi: 10.1007/s11837-020-04037-3.

Leonardo Snozzi and Jean-François Molinari. A cohesive element model for mixed mode loading with frictional contact capability. *International Journal for Numerical Methods in Engineering*, 93(5):510–526, 2013. doi: 10.1002/nme.4398.

Aarash Sofla, Erkin Seker, James P. Landers, and Matthew R. Begley. PDMS-Glass Interface Adhesion Energy Determined Via Comprehensive Solutions for Thin Film Bulge/Blister Tests. *Journal of Applied Mechanics*, 77(3), 02 2010. ISSN 0021-8936. doi: 10.1115/1.4000428. 031007.

Ala Tabiei and Wenlong Zhang. Composite Laminate Delamination Simulation and Experiment: A Review of Recent Development. *Applied Mechanics Reviews*, 70(3), 06 2018. ISSN 0003-6900. doi: 10.1115/1.4040448. 030801.

M.D. Thouless and Q.D. Yang. A parametric study of the peel test. *International Journal of Adhesion and Adhesives*, 28(4):176 – 184, 2008. ISSN 0143-7496. doi: https://doi.org/10.1016/j.ijadhadh.2007.06.006. Peel testing.

Koji Uenishi and James R. Rice. Universal nucleation length for slip-weakening rupture instability under nonuniform fault loading. *Journal of Geophysical Research: Solid Earth*, 108(B1), 2003. doi: 10.1029/2001JB001681.

V. Venzal, S. Morel, T. Parent, and F. Dubois. Frictional cohesive zone model for quasi-brittle fracture: Mixed-mode and coupling between cohesive and frictional behaviors. *International Journal of Solids and Structures*, 198:17 – 30, 2020. ISSN 0020-7683. doi: https://doi.org/10.1016/j.ijsolstr.2020.04.023.

Richard Villey, Costantino Creton, Pierre-Philippe Cortet, Marie-Julie Dalbe, Thomas Jet, Baudouin Saintyves, Stéphane Santucci, Loïc Vanel, David J. Yarusso, and Matteo Ciccotti. Rate-dependent elastic hysteresis during the peeling of pressure sensitive adhesives. *Soft Matter*, 11:3480–3491, 2015. doi: 10.1039/C5SM00260E.

Koushik Viswanathan, Narayan K. Sundaram, and Srinivasan Chandrasekar. Slow wave propagation in soft adhesive interfaces. *Soft Matter*, 12:9185–9201, 2016a. doi: 10.1039/C6SM01960A.

Koushik Viswanathan, Narayan K. Sundaram, and Srinivasan Chandrasekar. Stick-slip at soft adhesive interfaces mediated by slow frictional waves. *Soft Matter*, 12:5265–5275, 2016b. doi: 10.1039/C6SM00244G.

M. Vocialta, N. Richart, and J.-F. Molinari. 3d dynamic fragmentation with parallel dynamic insertion of cohesive elements. *International Journal for Numerical Methods in Engineering*, 109(12):1655–1678, 2016. doi: 10.1002/nme.5339.

K. Y. Volokh. Comparison between cohesive zone models. *Communications in Numerical Methods in Engineering*, 20(11):845–856, 2004. doi: 10.1002/cnm.717.

Kelin Wang and Anne M. Tréhu. Invited review paper: Some outstanding issues in the study of great megathrust earthquakes—the cascadia example. *Journal of Geodynamics*, 98:1 – 18, 2016. ISSN 0264-3707. doi: https://doi.org/10.1016/j.jog.2016.03.010.

L. Wang, D.C. Li, J.S. Yang, F. Shao, X.H. Zhong, H.Y. Zhao, K. Yang, S.Y. Tao, and Y. Wang. Modeling of thermal properties and failure of thermal barrier coatings with the use of finite element methods: A review. *Journal of the European Ceramic Society*, 36(6):1313 – 1331, 2016. ISSN 0955-2219. doi: https://doi.org/10.1016/j.jeurceramsoc.2015.12.038.

Q Jane Wang and Yip-Wah Chung, editors. *Encyclopedia of Tribology*. Springer, 2013. ISBN 9780387928982.

Julie F. Waters and Pradeep R. Guduru. Mode-mixity-dependent adhesive contact of a sphere on a plane surface. *Proceedings of the Royal Society A: Mathematical, Physical and Engineering Sciences*, 466(2117): 1303–1325, 2010. doi: 10.1098/rspa.2009.0461.

Yueguang Wei. Modeling nonlinear peeling of ductile thin films–critical assessment of analytical bending models using fe simulations. *International Journal of Solids and Structures*, 41(18):5087 – 5104, 2004. ISSN 0020-7683. doi: https://doi.org/10.1016/j.ijsolstr.2004.04.026.

John A. Williams and James J. Kauzlarich. Application of the bulk properties of a silicone psa to peeling. *International Journal of Adhesion and Adhesives*, 28(4):192 – 198, 2008. ISSN 0143-7496. doi: https://doi.org/10.1016/j.ijadhadh.2007.06.007. Peel testing.

S.M. Xia, L. Ponson, G. Ravichandran, and K. Bhattacharya. Adhesion of heterogeneous thin films—i: Elastic heterogeneity. *Journal of the Mechanics and Physics of Solids*, 61(3):838 – 851, 2013. ISSN 0022-5096. doi: https://doi.org/10.1016/j.jmps.2012.10.014.

Yangjian Xu, Yuvraj Singh, Changliang Pan, and Ganesh Subbarayan. Adhesive toughness and instability in bonded heterogeneous films. *International Journal of Solids and Structures*, 169:41 – 54, 2019. ISSN 0020-7683. doi: https://doi.org/10.1016/j.ijsolstr.2019.04.003.

Caihong Xue, Wengui Li, Jianchun Li, and Kejin Wang. Numerical investigation on interface crack initiation and propagation behaviour of self-healing cementitious materials. *Cement and Concrete Research*, 122:1 – 16, 2019. ISSN 0008-8846. doi: https://doi.org/10.1016/j.cemconres.2019.04.012.

Tetsuo Yamaguchi, Yoshinori Sawae, and Shmuel M. Rubinstein. Effects of loading angles on stick–slip dynamics of soft sliders. *Extreme Mechanics Letters*, 9:331 – 335, 2016. ISSN 2352-4316. doi: https://doi.org/10.1016/j.eml.2016.09.008.

H.B. Yin, L.H. Liang, Y.G. Wei, Z.L. Peng, and S.H. Chen. Determination of the interface properties in an elastic film substrate system. *International Journal of Solids and Structures*, 191-192:473 – 485, 2020. ISSN 0020-7683. doi: https://doi.org/10.1016/j.ijsolstr.2020.01.003.

Jun Zhang, Jiaqi Wang, Zhenwei Yuan, and Hong Jia. Effect of the cohesive law shape on the modelling of adhesive joints bonded with brittle and ductile adhesives. *International Journal of Adhesion and Adhesives*, 85:37 – 43, 2018. ISSN 0143-7496. doi: https://doi.org/10.1016/j.ijadhadh.2018.05.017.

Liang Zhang and Jyhwen Wang. A generalized cohesive zone model of the peel test for pressure-sensitive adhesives. *International Journal of Adhesion and Adhesives*, 29(3):217 – 224, 2009. ISSN 0143-7496. doi: https://doi.org/10.1016/j.ijadhadh.2008.05.002.

Yiming Zhang and Xiaoying Zhuang. A softening-healing law for self-healing quasi-brittle materials: Analyzing with strong discontinuity embedded approach. *Engineering Fracture Mechanics*, 192:290 – 306, 2018. ISSN 0013-7944. doi: https://doi.org/10.1016/j.engfracmech.2017.12.018.

Yongde Zhang and Mingyue Lu. A review of recent advancements in soft and flexible robots for medical applications. *The International Journal of Medical Robotics and Computer Assisted Surgery*, 16(3):e2096, 2020. doi: 10.1002/rcs.2096.

Ming Zhou, Noshir Pesika, Hongbo Zeng, Yu Tian, and Jacob Israelachvili. Recent advances in gecko adhesion and friction mechanisms and development of gecko-inspired dry adhesive surfaces. *Friction*, 1(2):114–129, Jun 2013. ISSN 2223-7704. doi: 10.1007/s40544-013-0011-5.

W. Zhu, L. Yang, J.W. Guo, Y.C. Zhou, and C. Lu. Determination of interfacial adhesion energies of thermal barrier coatings by compression test combined with a cohesive zone finite element model. *International Journal of Plasticity*, 64:76 – 87, 2015. ISSN 0749-6419. doi: https://doi.org/10.1016/j.ijplas.2014.08.003.

Yong Zhu, Kenneth M. Liechti, and K. Ravi-Chandar. Direct extraction of rate-dependent traction–separation laws for polyurea/steel interfaces. *International Journal of Solids and Structures*, 46(1):31 – 51, 2009. ISSN 0020-7683. doi: https://doi.org/10.1016/j.ijsolstr.2008.08.019.

Zhongmeng Zhu, Yan Xia, Jian Li, Chengkai Jiang, and Han Jiang. Rate dependent shear debonding between a highly stretchable elastomer and a rigid substrate: Delayed debonding and pre-stretch effect. *Engineering Fracture Mechanics*, 222:106743, 2019. ISSN 0013-7944. doi: https://doi.org/10.1016/j.engfracmech.2019.106743.

A. Zosel. Effect of cross-linking on tack and peel strength of polymers. *The Journal of Adhesion*, 34(1-4): 201–209, 1991. doi: 10.1080/00218469108026514.

V. Zotti, K. Rapina, P.-P Cortet, L. Vanel, and Stéphane Santucci. Bending to kinetic energy transfer in adhesive peel front microinstability. *Physical Review Letters*, 122, 02 2019. doi: 10.1103/PhysRevLett.122.068005.

Appendices

A Additional Examples of Applications

In the introduction in Section 1.1 a couple of examples of the applications of stronger adhesive pads were mentioned. This Appendix will describe some of the applications in more depth to show the extent of the possibilities emerging from dry adhesive technology, who go far beyond mimicking gecko feet.

Robots with adhesive feet show exceptional climbing abilities, showing reversibility of their adhesive feet without damaging the surface on which they are climbing [Li et al., 2016, Dharmawan et al., 2019, Sahay et al., 2015]. Their application ranges from inspection devices in dangerous environments such as high-rise buildings and nuclear power plants [Menon et al., 2004] to search and rescue operations [Dharmawan et al., 2019]. Examples of designs of such adhesive robots are shown in Figure 46.

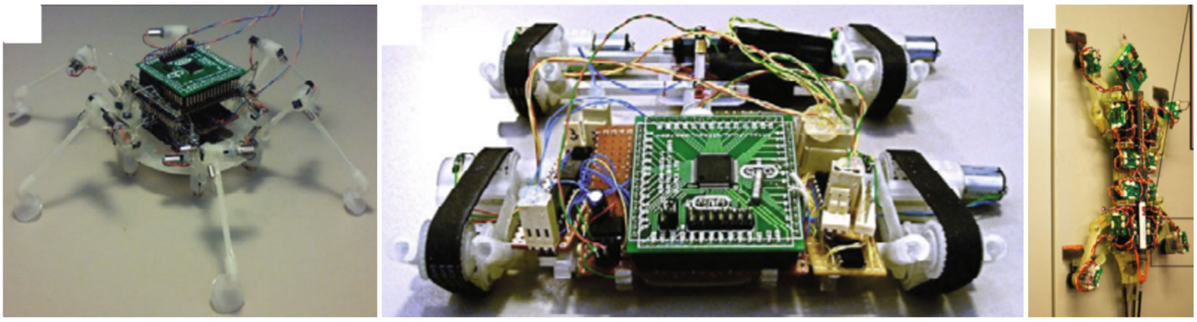

Figure 46: Climbing robots, designed with adhesive surfaces as feet. Different designs exist, ranging from spider-inspired (left) to gecko-inspired (right) designs and adhesive wheels (middle). An example of future applications of better design of adhesive pads, achieved from the current state-of-the-art knowledge. Pictures from [Li et al., 2016].

Continuing in the field of robotics, high-precision grippers have gained interest because they allow moving objects without modifying or damaging them, as dry adhesives do not leave any residue and because of their visco-elastic behavior do not indent the hard materials they attach to [Shintake et al., 2018, Lee et al., 2019, Zhang and Lu, 2020, Hsiao et al., 2019]. They can be applied in minimally invasive surgery, where instead of an incision, a mechanical robot is inserted in the patient to execute the surgery[Rateni et al., 2015], or assist in invasive surgery, replacing a human hand by a more precise robotic gripper [Hammond et al., 2014]. High-precision non-damaging gripper application has recently also been extended to the probing of fragile biological samples under-water, in the case of deep reefs [Galloway et al., 2016]. Figure 47 shows images of these various applications.

(a) Soft gripper for minimally invasive surgical procedures where instead of an incision, a mechanical device is inserted in the body. Figure from Rateni et al. [2015].

(b) Super-precise sensors used for medical procedures, where a robot gripping device can more accurately monitor the applied pressure and thus the amount of damage caused, than a human could. Figure from Hammond et al. [2014].

(c) Device used to micro-probe and grip coral without damaging them with soft adhesives. Figure from Galloway et al. [2016].

Figure 47: Images showing examples of applications of soft, dry adhesives in high-precision non-damaging robots. Dry adhesives are superior in that they do not leave any residue on the material, yet allow to capture it very precisely and hold it reliably.

In medicine, bio-compatible dry adhesives allow large mechanical deformations, adaptability to changing tissue, compatibility with pharmaceutical compounds, and can adhere quickly and easily to rough or wet surfaces [Baik et al., 2019, Boyadzhieva et al., 2019]. They are thus used as scaffolds for external wounds [Boyadzhieva et al., 2019] and scaffolds for eye wounds [Grinstaff, 2007], but also as tissue defect repair patches for the heart, abdomen or stomach [Hsiao et al., 2019, Fujie et al., 2009] or as pharmaceutical drug patches [Mohammed et al., 2016]. The adhesive attachment of such pads allows sealing the tissue defect with damaging close-by tissue with anchoring systems [Hsiao et al., 2019]. In other applications, wearable electronics are incorporated into skin patches or drugs are delivered through the skin [Baik et al., 2019]. Illustrative images of electronics in adhesive patches and adhesive patches to repair internal tissue damage are shown in Figure 48.

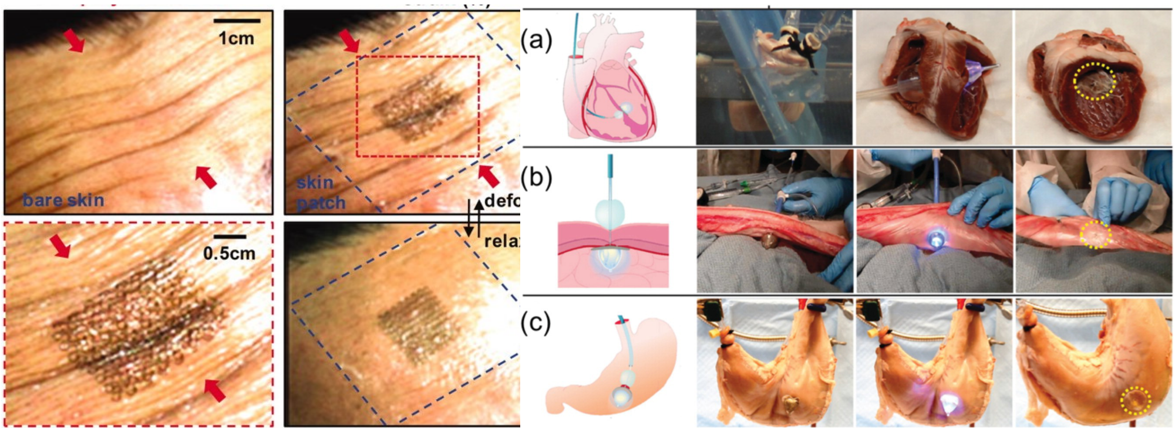

(a) Adhesive patch attached to the skin with a wearable electronic registering vital sign. Figure from Baik et al. [2019].

(b) Illustration of application of adhesive patches for healing internal skin tissue damage of the heart, abdomen, or stomach by application of pressure with balloons. Figure from Hsiao et al. [2019].

Figure 48: Images showing examples of applications of soft, dry adhesives in medical patches for internal tissue damage healing and externally applied with wearable electronics for monitoring of vital functions.

B Appendices to Simulation Development

B.1 Finite Element Solution Method in Akantu

The finite element solution method used in Akantu uses a modified Newton-Raphson method to solve nonlinear systems. In the dynamic solution procedure, this is implemented as a predictor and corrector scheme. The dynamic solution method is based on a Newmark-Beta discretization of time, with as default setting the central difference method, an explicit integration scheme. In this section, detailed descriptions of the solution methods are given, largely reproduced from Richart [2016]. Note that no special notation will be used for tensors and vectors, as this differentiation is already explicitly made in the text.

Akantu allows the input of Dirichlet (displacement) or Neumann (tractions) imposed boundary conditions. For static simulations, the following equation needs to be solved, to obtain the full state of the system under static equilibrium:

$$F_{int}(u) = F_{ext} \tag{26}$$

Where K is the global stiffness matrix of the solid, F^i_{int} is the internal force vector, calculated based on the vector of the nodal displacements u and F_{ext} is the vector of applied forces.The internal force vector at the previous iteration is denoted F^i_{int} and the displacement increment relative to the last iteration is denoted δu^{i+1}. The linearization leads to a systems of equations expressed as:

$$K^i \delta_u^{i+1} = F_{ext} - F^i_{int} \tag{27}$$

A modified Newton-Raphson scheme is implemented to solve the equation. The modified scheme refers to the update of stiffness tensor K at every iteration. In a non-linear scheme, K is dependant on the displacement of the nodes. During the Newton-Raphson iterations, K is updated according to the new displacement vector. A pre-defined maximum tolerance $r_{residual}$ is input and the scheme is continued until the difference between internal and external forces is smaller than the predefined tolerance, or until too many iterations have been executed The iteration-based solution procedure is started from the initial displacement u^0.

$$r^i = ||F_{ext} {-} F^i_{int}|| = ||F_{ext} - Ku^i|| \tag{28a}$$

$$\text{While } r^i > r_{residual} : \tag{28b}$$

$$K \cdot \delta u^i = r^i \quad \rightarrow \text{Solve for } \delta u^i \tag{28c}$$

$$u^{i+1} = u^i + \delta u^i \tag{28d}$$

$$\text{recalculate } r^i \tag{28e}$$

For a dynamic system without damping, the system of equations to solve becomes:

$$M\ddot{u} + Ku = F_{ext} \tag{29}$$

Where $\ddot{u}$ designates the nodal acceleration vector, $\dot{u}$ the nodal velocity vector and M the mass matrix of the system. In our case, this is the lumped mass matrix. Other choices are possible as well depending on the targeted application. The Newmark-Beta scheme for the solution of a time-discretization problem consists of a system of three equations to be solved:

$$M\ddot{u}_{t+\Delta t} + Ku_{t+\Delta t} = F_{ext,t+\Delta t} \tag{30a}$$

$$u_{t+\Delta t} = u_t + (1-\alpha)\Delta t \cdot \dot{u}_t + \alpha\Delta t \cdot \dot{u}_{t+\Delta t} + (1/2-\alpha)(\Delta t)^2 \cdot \ddot{u}_t \tag{30b}$$

$$\dot{u}_{t+\Delta t} = \dot{u}_t + (1-\beta)\Delta t \cdot \ddot{u}_t + \beta\Delta t \cdot \ddot{u}_{t+\Delta t} \tag{30c}$$

The last known time is t and the timestep used is Δt. Prior knowledge of the full state of the system at time t exists, as well as boundary conditions for the time $t + \Delta t$. Parameters for accuracy and stability of the algorithm are α and β. In Akantu, β is set to $1/2$ and by default, α is equal to 0, which simplifies to the central difference method, an explicit solution procedure. Setting $\beta = 1/2$ and $\alpha = 1/2$ results in an implicit schema, the middle point role, that is unconditionally stable (but does not necessarily converge in the Newton-Raphson solution iteration).

$$M\ddot{u}_{t+\Delta t} + Ku_{t+\Delta t} = F_{ext,t+\Delta t} \tag{31a}$$

$$u_{t+\Delta t} = u_t + \Delta t \cdot \dot{u}_t + 1/2(\Delta t)^2 \cdot \ddot{u}_t \tag{31b}$$

$$\dot{u}_{t+\Delta t} = \dot{u}_t + 1/2\Delta t \cdot \ddot{u}_t + 1/2\Delta t \cdot \ddot{u}_{t+\Delta t} \tag{31c}$$

To solve the system of equations practically, a solution method with a predictor and corrector is used.

$$u_{t+\Delta t} = u_t + \Delta t \cdot \dot{u}_t + 1/2(\Delta t)^2 \cdot \ddot{u}_t \tag{32a}$$

$$\dot{u}^{pred}_{t+\Delta t} = \dot{u}_t + \Delta t \cdot \ddot{u}_t \tag{32b}$$

$$M \cdot (\delta\ddot{u} + \ddot{u}_t) = F_{ext,t+\Delta t} - F_{int,t+\Delta t} = F_{ext,t+\Delta t} - Ku_{t+\Delta t} \tag{32c}$$

$$\dot{u}_{t+\Delta t} = \dot{u}^{pred}_{t+\Delta t} + \frac{\Delta t}{2}\delta\ddot{u} \tag{32d}$$

$$\ddot{u}_{t+\Delta t} = \ddot{u}_t + \delta\ddot{u} \tag{32e}$$

B.2 Validation of the Reattachment at a Different Location in the Cohesive Law

The reattachment adaptation of the cohesive law was validated using a simulation of simple pulling tests, both in a static and a dynamic simulation. The test confirms that the same behavior is recovered after reattachment at a different location. The test sequence is shown in Figure 49 and the corresponding force response is schematically illustrated in Figure 50. It consists of two blocks joined by a cohesive zone being pulled until full damage of the cohesive zone. Then, the top block is moved sideways and pressed downwards for reattachment. Once reattached, it is pulled upwards again to test the reattachment. The exact same behavior on the top block and cohesive zone should be and is observed during the pulling before and after reattachment. The same test is done in three dimensions and is confirmed to work as well.

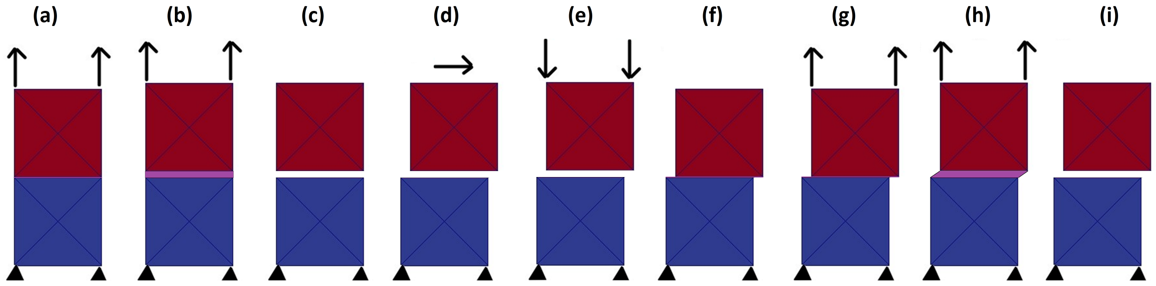

Figure 49: Sequence of the pulling test confirming the correct implementation of the cohesive zone, where reattachment at another location is allowed. Two blocks with a cohesive zone in between are pulled in tension until full damage of the cohesive zone. (Figures a-c) The top block is moved sideways (Figure d) and pressed downwards (Figure e) for reattachment (Figure f). Once reattached, it is pulled upwards (Figure g-i). The exact same behavior on the top block and cohesive zone should be and is observed.

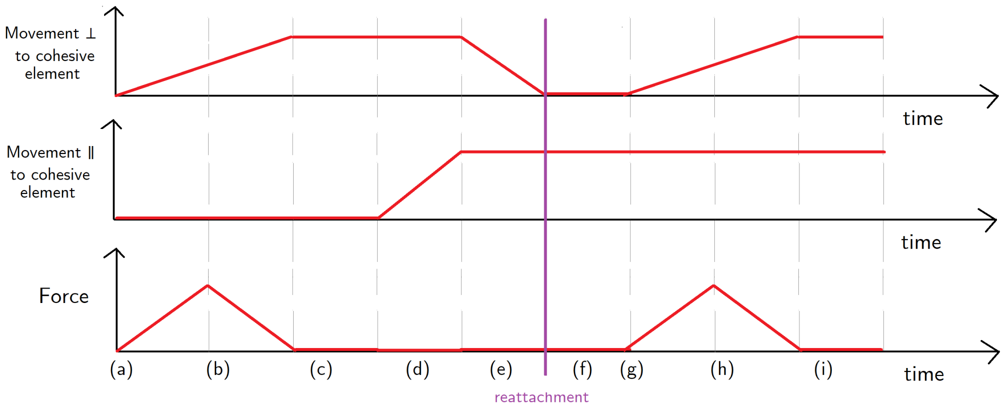

Figure 50: Schematic force values for the pulling test confirming the functioning of the reversibility of the cohesive zone, corresponding to Figure 49. Two blocks with a cohesive zone in between are pulled in tension until full damage of the cohesive zone: the perpendicular movement steadily increases while the force follows the cohesive law. (Figures a-c) The top block is moved sideways, increasing parallel displacement steadily (Figure d) and pressed downwards decreasing perpendicular movement (Figure e) for reattachment (Figure f). Once reattached, it is pulled upwards (Figure g-i). The exact same behavior is observed before and after reattachment in sequence a-c and g-i.

As the behavior should correspond exactly according to the implementation of the formulae and is confirmed to do so, the material parameters used are of no significance here and therefore not reported.

B.3 Determination of Desired Damping Value

An initial estimate for an appropriate $t_{damp1\%}$ was obtained by pulling a 2D square block of linear elastic material and without a cohesive zone in pure tension with a speed v until 1 % strain and releasing it to observe oscillations resulting from the loading relaxation. This was done for different values of $t_{damp1\%}$, for material parameters similar to the simulations. The parameters used for this are shown in Table 4.

Young's modulus E	100	kPa
Poisson's ratio μ	0.45	[-]
Mass Density ρ	1000	kg/m^3
Dimension t	10	mm
Element size t	1	mm
Speed v	0.5	mm/s
Time to 1 % damping $t_{damp1\%}$	$1ms$, $1\mu s$,	100, 10 ns, 0

Table 4: Material properties used for the calibration test of the time to 1 % damping.

The desired situation is to have the block returning almost immediately to its stable position at rest, both in the pulling direction and in the perpendicular direction without oscillations. The results obtained are shown on Figure 51. The damping time of 0 s matches an infinite damping, while the no damping case is not depicted as the simulation would not converge. Instead, the highest possible damping time is used as a reference for little damping as it is visible that for this case already the amount of damping is insufficient. The graphs show that at an infinite amount of damping and at low damping times, the damping creates additional resistance and the level force is affected in a physically unacceptable way. Damping times that do not significantly increase the force level and sufficiently damp oscillations, are 1-10 ns. This will be used as an initial estimate for the damping time and during the execution of the adhesive pad simulations, and will be further corrected where necessary.

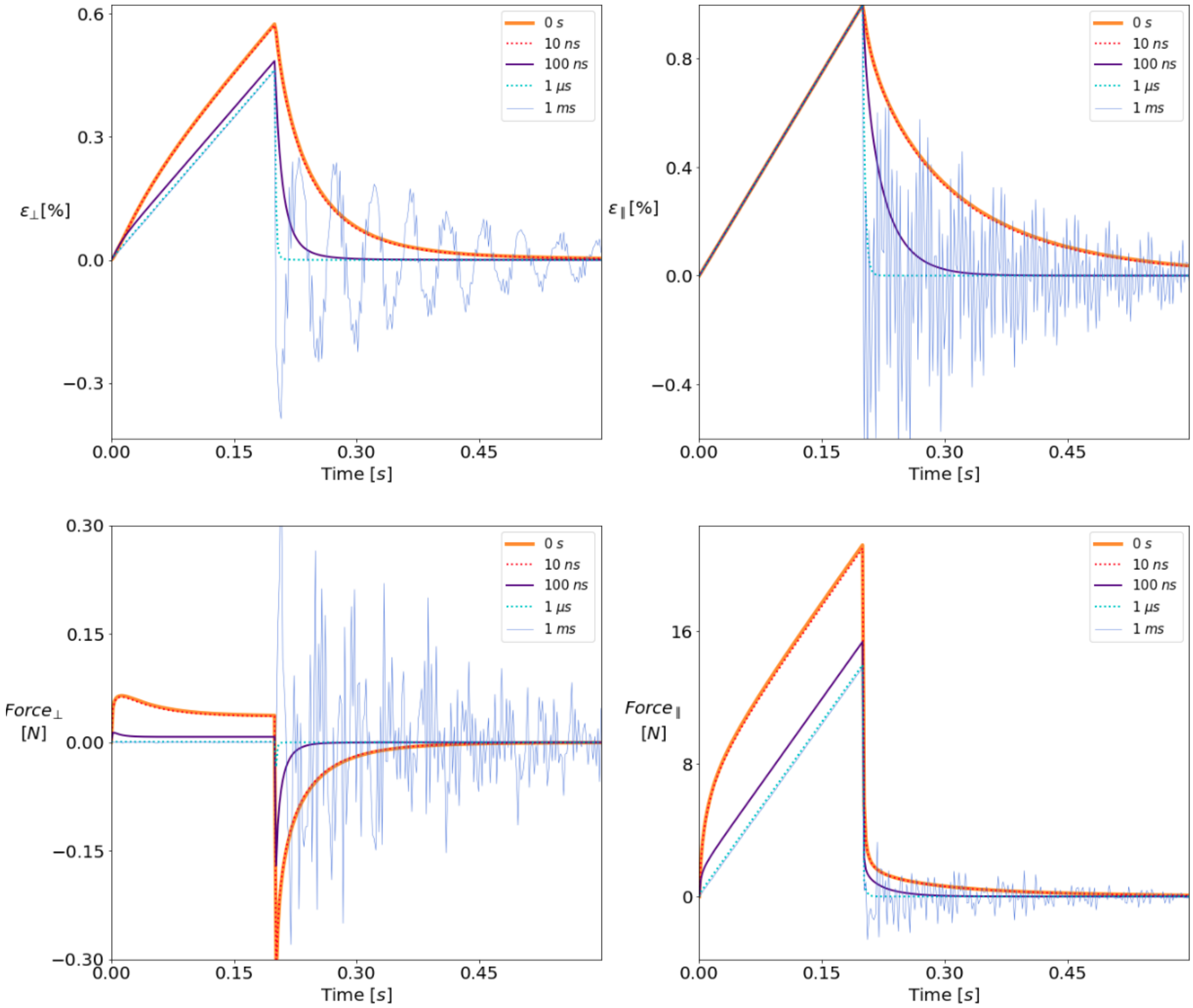

Figure 51: Results of the pulling test to calibrate damping for a loading velocity comparable to the simulation. Different colors are used for the different damping times. The right graphs show the behavior in the pulling direction, the left graphs in the perpendicular direction. The top graph shows the displacement (expressed as stretch of the full block) and the bottom graphs the force. For the displacement and perpendicular force, the node furthest away from the middle of the block is studied and for the pulling force, the resultant of forces for all the pulled nodes is studied. All graphs show that a damping time of 1 ms causes excessive oscillations. Meanwhile, the graphs for 0 s (infinite damping) and 10 ns overlap. They show undesirable characteristics: a non-physically high pulling force, higher displacement in the perpendicular direction, and a very long time to return to the equilibrium position. The values of 1-10 μs corresponds best to the desired behavior.

B.4 Visualization of Solution Algorithm

The simulation is started with a static solution procedure, switched to a dynamic solution procedure as soon as damage is sufficiently initiated, and pulling is paused at the instances of breaking of cohesive elements. At the start of the dynamic procedure and after pulling pauses, the velocity is imposed gradually. This is summarized in the following visualization of the algorithm.

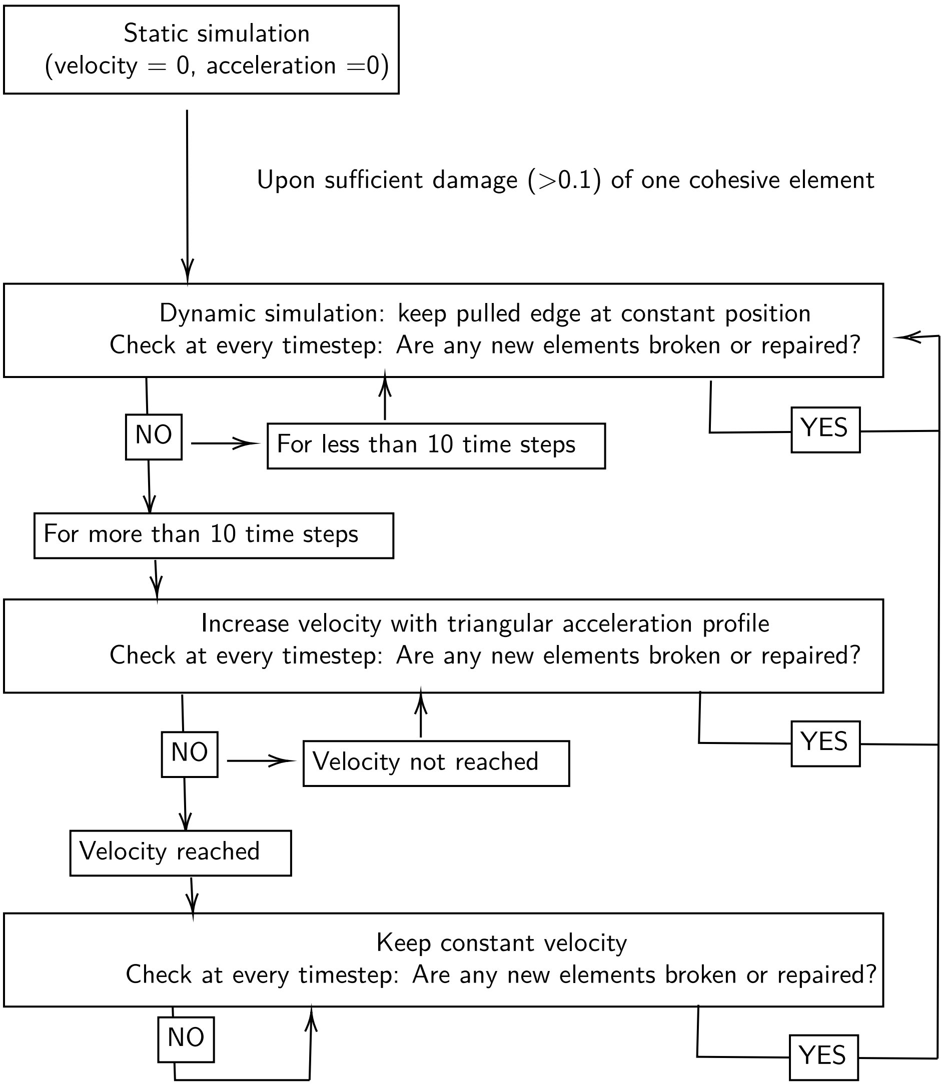

C Appendices to Results

C.1 Selection of Design Parameters

The geometrical parameters L,t and t_b of the simulations are chosen in the same order of magnitude as earlier experiments [Cohen et al., 2018, Honsali, 2018]. Bulk properties of elastic stiffness of the adhesive and backing were chosen among reasonable values for a PDMS sample, a commonly used soft adhesive. The linear elastic stiffness of the adhesive surface is chosen of the same order of magnitude as approximations based on fitting to experiments in [Cohen et al., 2018]. For the surface properties: the surface strength, energy, and mixed-mode coupling factor, a range of possible values was found in the literature (Section 4.1.4). Due to this uncertainty, the values were chosen for numerical convenience: small enough to allow failure in a reasonable time and large enough to allow convergence.

The following normalization values used and numerical properties used are common for all two-dimensional simulations. The depth of the pad d is in this case a geometrical as well as numerical parameter since this is by definition the case for a two-dimensional simulation: all output units are expressed per depth unit of length.

Geometrical and bulk properties

t	E	d
8 mm	50 kPa	1 m

Numerical Properties

ν	v	v'	$t_{1\%damp}$	T_{damp}	$L_{cohesive}$	ρ
0.45	0.6 mm/s	85 $\times 10^{-6}$	0.1 ms	1130	0.8 mm	1000 $kg/3^3$

Table 5: The normalization values E and t and numerical properties used for all simulations.

The parameters used for the simulations in the results are shown in Table 6.

Geometrical and Bulk Properties						
	Dimensional properties			Non-dimensional properties		
	$t_b(mm)$	$E_b(MPa)$	$L(mm)$	α	β	L/t
Cavitation, peeling and curling (5.1.1)	8	2	120	0.2	8	15
Pure curling (5.1.2)	8	2	16	0.2	8	2
Curling with interfacial cavitation(5.1.3)	8	5	120	0.2	20	15
Infinitely long pad (5.2)	8	2	640	0.2	8	80
Stick-Slip convergence (C.2)	8	0.4	120	0.2	1.6	15
Stick-Slip phase diagram (6.2)	8	0.4	120	0.2	1.6	15
PParameter sensitivity, convergence (6.1, C.2, C.5)	8	0.4	120	0.2	1.6	15

Surface Properties									
	Dimensional properties					Non-dimensional properties			
	$\delta_0(\mu m)$	$\sigma_c(kPa)$	$G_c(10^{-3}J/m^2)$	$k(10^6 N/m^3)$	$\delta_c(mm)$	γ	$\zeta(10^{-3})$	$\theta(10^{-3})$	κ
Cavitation, peeling and curling (5.1.1)	100	1.6	0.2	16	0.25	2.6	32	0.5	0.4
Pure curling (5.1.2)	100	1.6	0.2	16	0.25	2.6	32	0.5	0.4
Curling with interfacial cavitation(5.1.3)	100	3	0.18	30	0.12	4.8	60	0.45	0.4
Infinitely long pad (5.2)	100	0.4	0.2	4	1	0.64	8	0.5	0.4
Stick-Slip convergence (C.2)	50	0.6	0.025	12	0.083	1.9	12	0.0625	1
Stick-Slip phase diagram (6.2)	50	0.3	0.1	6	0.667	0.96	6	0.25	1
Parameter sensitivity, convergence (6.1, C.2, C.5)	50	0.3	0.1	6	0.667	0.96	6	0.25	1

Table 6: List of geometrical and surface parameters used for the two different reference simulations that were used for the study of the adhesive pad failure behavior.

C.2 Discussion of Convergence

The simulation results need to be converged in terms of mesh size refinement and of dynamic time step to prove convergence in time and space. A sample simulation will be used to show convergence, and as there is sufficient convergence to coarsen both mesh and time step, changing parameters without ceasing convergence is still possible.

The dynamic time step used of $0.5T_{crit}$ is converged: the curves for all smaller times steps almost exactly coincide with this one as seen on Figure 52. Some curves do show a spike in the moment of transition from a static to dynamic timestep: as this does not happen in all curves, this is not a physical event but a numerical side-effect of imposing a velocity and thus an acceleration. It can be seen that only the very large time steps of higher than $2T_{crit}$ depart from the other curves. Moreover, the opening profiles of $0.125T_{crit}$ and $1T_{crit}$ look exactly the same (figure not included).

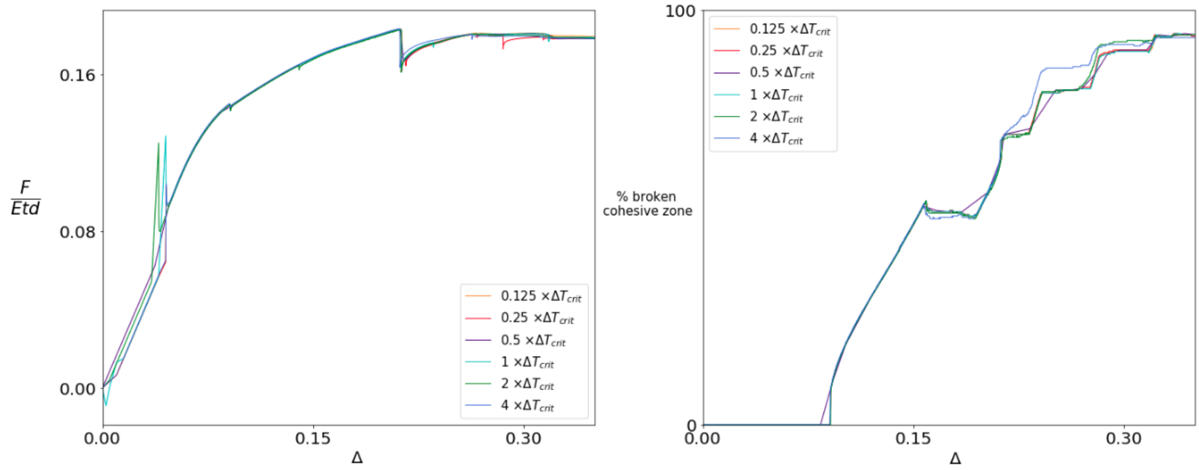

Figure 52: Force-displacement (left) and percentage of failure-displacement (right) graphs for simulations with different dynamic time steps. The force is the total pulling force in the X-direction that needs to be exerted upon the pulling end of the backing to pull this end the amount of displacement imposed. Until a time step of the size of the critical time step, there is an almost exact correspondence between the curves.

The mesh convergence study also shows a high coincidence between mesh size varied over a factor up to 30. Almost exact correspondence in the force-displacement curve is obtained (Figure 53 left), with the exception of the transition between the static and dynamic simulation that shows different spikes and the occurrence of a large drop and re-increase in force at the end of the simulation. Both of these events happen at larger meshes and are non-physical. The first spike in force is related to the build-up of a velocity in a shorter time, which has a relatively bigger effect on larger meshes. The drop and re-increases in force on the end for larger meshes are related to the pad being almost fully detached: in coarse meshes force redistributions in the elements lead more easily to non-physical detachment and reattachment. Both numerical phenomena have only a limited effect on the perceptual failure curve (Figure 53 right) as all the curves are almost coinciding. Even better convergence is reached at an element size of $t/5$ to $t/10$.

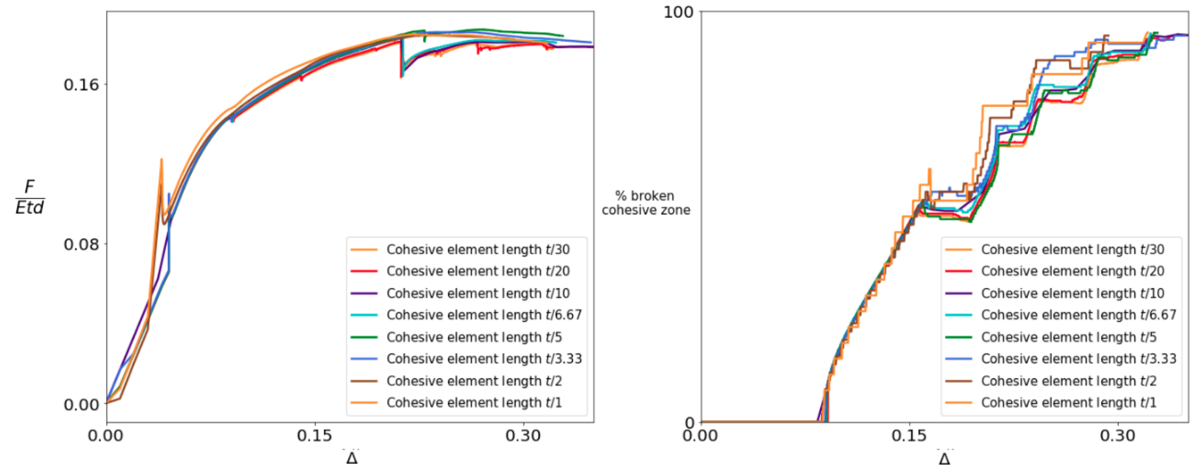

Figure 53: Force-displacement (left) and percentage of failure-displacement (right) graphs for simulations with different mesh sizes: the lengths shown are the size of the cohesive elements. The force is the total pulling force in the X-direction that needs to be exerted upon the pulling end of the backing to pull this end the amount of displacement imposed. While the force converges even at very rough meshes, the failure needs a more fine mesh to converge: $t/5$ is sufficient but $t/10$ would be preferred.

The opening profiles for simulations with a very large difference in mesh size, even when their global failure evolution (Figure 53 right) differs, shows very little differences in Figure 54. While the graphical resolution of the simulation with a very rough mesh is not as high (more blurring) as with a fine mesh size, the evolution and magnitude of events happening is barely affected. The non-physical mesh effects (drop and re-increase in force at the end, a spike in force at the beginning) do not create any significant difference in the opening profile here either. Rather than unnecessarily refining the mesh, these events can thus be disregarded in analyzing the physical situation.

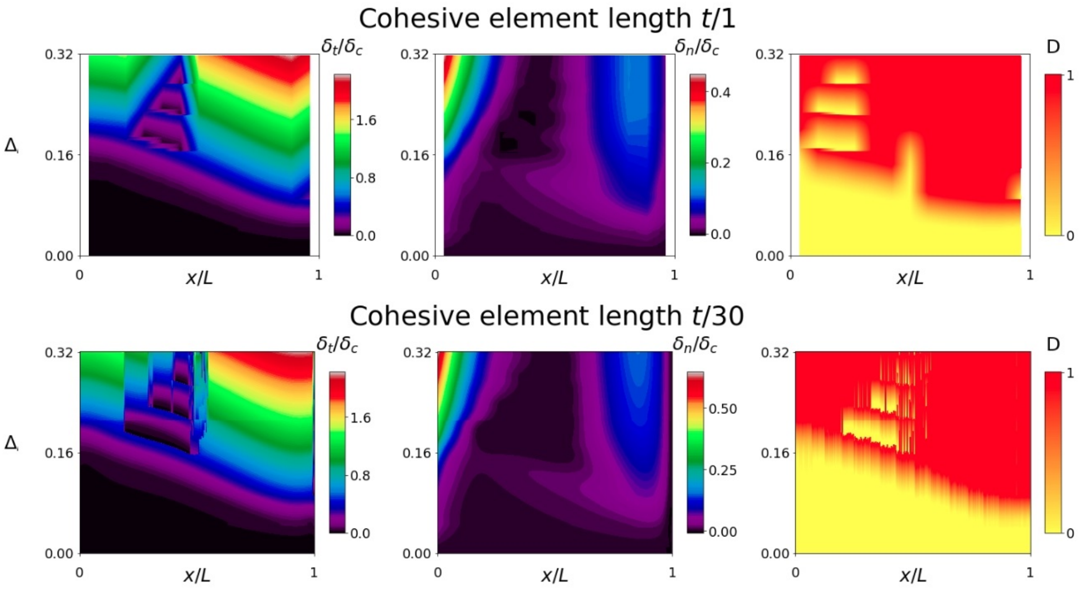

Figure 54: Detachment analysis of the surface of two simulations using different mesh sizes. The amount of displacement is advanced over the y-axis and the pad length is advanced over the x-axis on each of the Figures. The left graphs show the opening of the adhesive surface in the tangential direction, the middle graphs the opening in the normal direction, and the right graphs the damage of the surface.

To investigate the mesh-dependence of stick-slip events, convergence of another simulation with large amounts of stick-slip is checked. For the material parameters used for this simulation, refer to Appendix C.1. It is found, as shown in the force-displacement graphs in Figure 55 for different mesh sizes, that the occurrence of stick-slip is mesh-independent. The size of the force drops and their amount does vary with mesh size, but the regions of their occurrence and their existence are mesh independent. It is concluded based on this analysis that stick-slip is not a mesh effect and the mesh size is sufficiently refined to capture it.

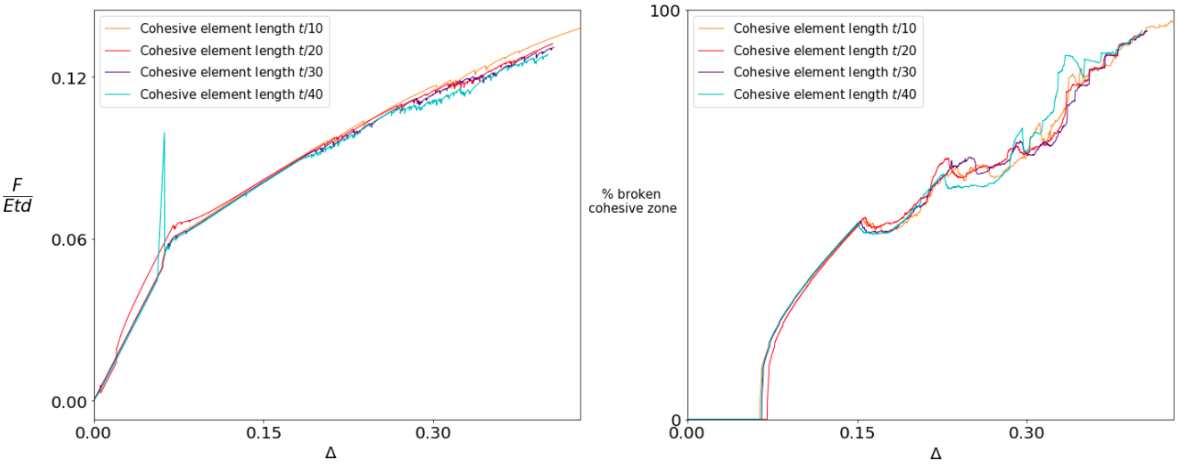

Figure 55: Force-displacement (left) and percentage of failure-displacement (right) graphs for simulations with different mesh sizes. The force is the total pulling force in the X-direction that needs to be exerted upon the pulling end of the backing to pull this end the amount of displacement imposed. Good correspondence between all mesh sizes is found. The amount of stick-slip and the size of the force drops related to it vary with mesh size, but the location and the occurrence of stick-slip do not.

C.3 Linear Elastic Region

In the linear elastic region of the simulation, upon application of an almost infinitesimally small displacement on the backing, the pad forms a cavitation-like shape as shown in Figure 56. The boundary conditions of the rigid substrate and the sideways pulling of the backing cause a moment in the pad that creates this shape which can also be observed in Figure 57 (top). Figure 58 (top) shows the mechanical reason for this: all the stress is located in the backing.

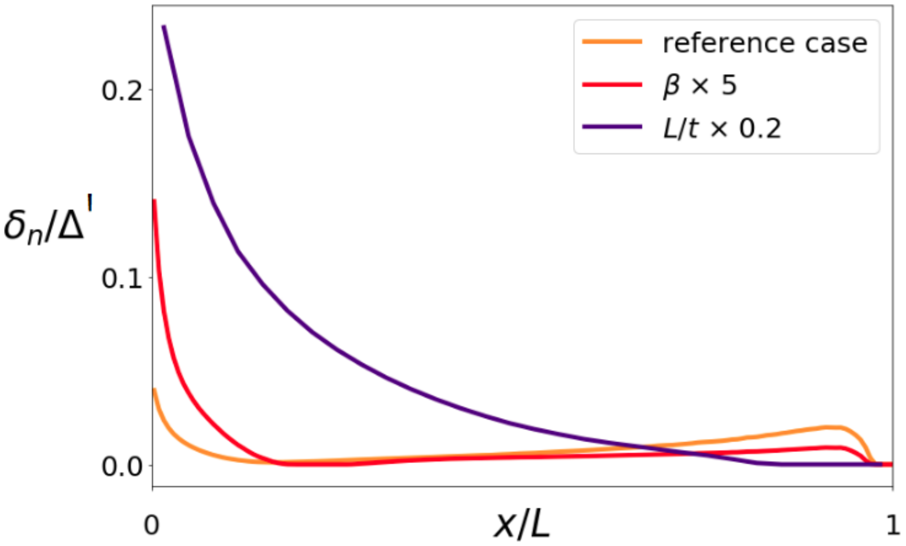

Figure 56: Shape in the normal direction of the pad surface at very small displacements (7 orders of magnitude smaller than the pad thickness). A reference case with mixed cavitation and curling shapes is shown, together with the shape if the parameters β and L/t are varied. Both a higher β and a lower L/t favor curling development over interfacial cavity development.

In a pad with a stiffer backing (higher β), this force will be spread through a longer part of the backing as shown in Figure 58, resulting in a more arched deformation as shown in Figure 57. In shorter pads (lower L/t), if the same length of the backing is activated, this constitutes a relatively longer part of the pad, also shown in Figure 58. Figure 57 then shows how this deformation field for a lower L/t ratio is not stretched out enough to develop a successive convex and concave curvatures along the pad length starting from the pulling end, but only a convex curvature is developed. It is these bulk parameters (stiffness of the backing, length of the pad) that thus will determine how the pulling forces are distributed in the pad relative to the pulled distance, prior to detachment initiation.

The adhesive surface layer failure characteristics (ζ, θ) then determines for which level of imposed displacement failure will initiate. These parameters determine at which displacement the first element starts softening.

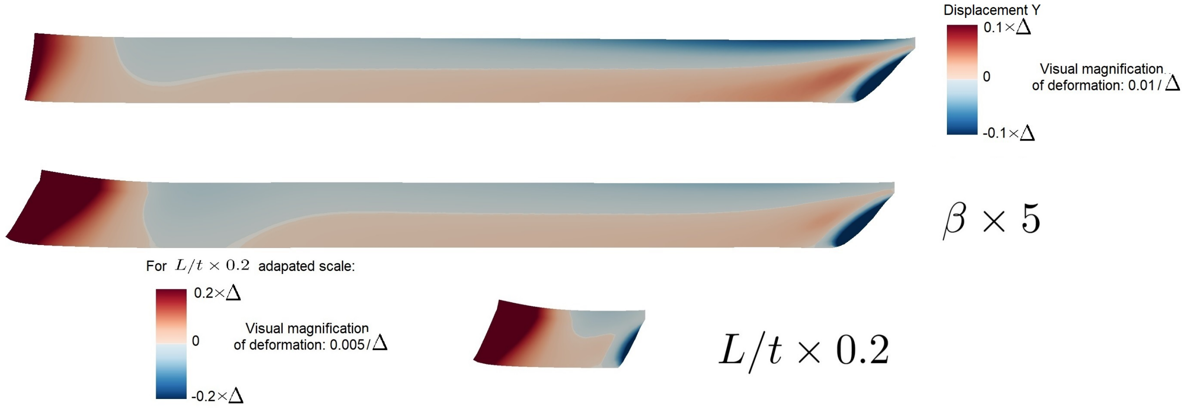

Figure 57: Visualisation of the shape of the pad at very small deformation. Shown in color are the displacements in the Y direction. Visual magnification of the deformation is applied. The pad is shown for the reference case, with a 5 times higher β and with a 5 times lower L/t to show the influence of these parameters. Number are expressed in terms of the pulled displacement Δ, and a different scale is used for the case with a lower L/t. Both a higher β and a lower L/t favor a single-curved convex shape, while the reference case shows more of a tendency to develop a double curvature: concave near the pulling end and convex further towards the opposite end.

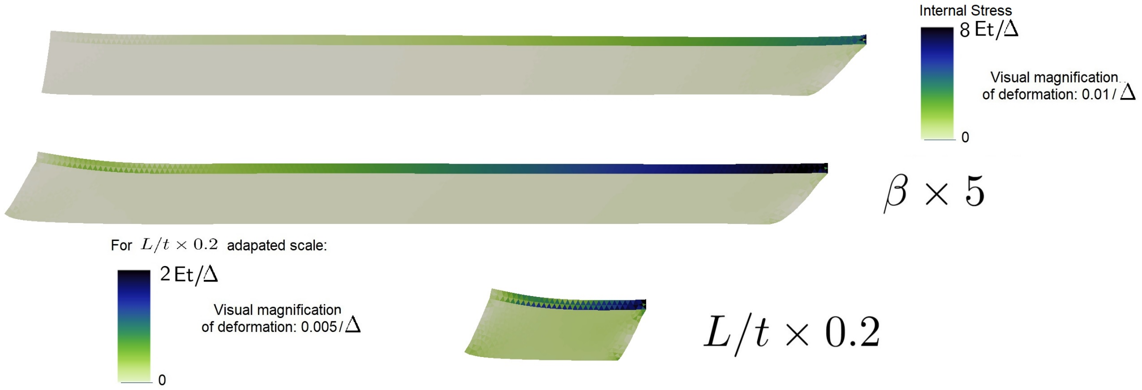

Figure 58: Visualisation of the shape of the pad at very small deformation. Shown in color are the total internal stresses. Visual magnification of the deformation is applied. The pad is shown for the reference case, with a 5 times higher β and with a 5 times lower L/t to show the influence of these parameters. Number are expressed in terms of the pulled displacement Δ, and a different scale is used for the case with a lower L/t. Both a higher β and a lower L/t allow the stresses to distribute over a larger portion of the backing.

C.4 Discretized Model Internal Distributions

Results showed that it is the stress distribution inside the soft material of the adhesive pad that leads to the failure behavior. These distributions could intuitively be understood based on the deformation graphs shown in Section 5. For a more complete understanding, the discretized force internal force distributions will be provided in this Appendix. It will be shown the resultants of these internal forces due to non-uniform stress distributions over the pad will indeed have a resultant couple. We will however present them as nodal internal force distributions, as the high stiffness of the backing of the pads makes stress distribution very inhomogeneous and therefore visually hard to read. Note that the forces will be shown color-coded over the adhesive pad area, but are in reality nodal forces of a discrete nature.

The nodal force distributions discussed will show the propagation of failure during increased imposed displacement increasing from (I) up. The deformation of the pad is visually magnified for clarity, and the damage of the adhesive surface is shown on the initial surface. The left figures show color-coded the internal forces in the Y-direction (axes provided on the figure for reference) and the right figure shows color-coded the internal forces in the X-direction, the pulling direction. For the convenience of the reader, the resultant forces from these distributions (equivalent to the stress state) are schematically drawn on the figures as red arrows. The couples resulting from these forces are also indicated on the figures. For a description of the failure sequences related to this pad, the reader is referred to Section 5.1.

Consider Figure 59 showing the internal forces for the curling case. We will here draw the resulting couples associated with the internal stress distributions next to the pad. We will subsequently in Figure 60 and Figure 61 for readability draw them inside the pad, despite the couple being the resultant of the also drawn resultant forces of the internal forces. On Figure 59, during the initial loading of the pad (I), the boundary conditions prescribe the pulling of a stiff backing from one side on a soft adhesive, that has an even softer surface adhesion. This causes a vertical force on the opposite end of the pad and a difference in horizontal force between the top and bottom of the pad, both resulting in a couple in the same direction. During the continued pulling and curling movement of the pad in Figure 59 (II) this continues. During phase (III) when the curling continues, it is seen that the horizontal forces now also appear in the detached bottom of the pad, as this is now allowed to deform. The couple resulting from the horizontal forces decreases. The upwards vertical force spreads over a larger part of the pad. Finally, this movement is continued in (IV) and the horizontal forces are on the soft part of the adhesive, with almost no forces in the backing. This creates an opposite couple that now cancels out the moment from the vertical forces: an equilibrium amount of rotation of the pad is almost reached.

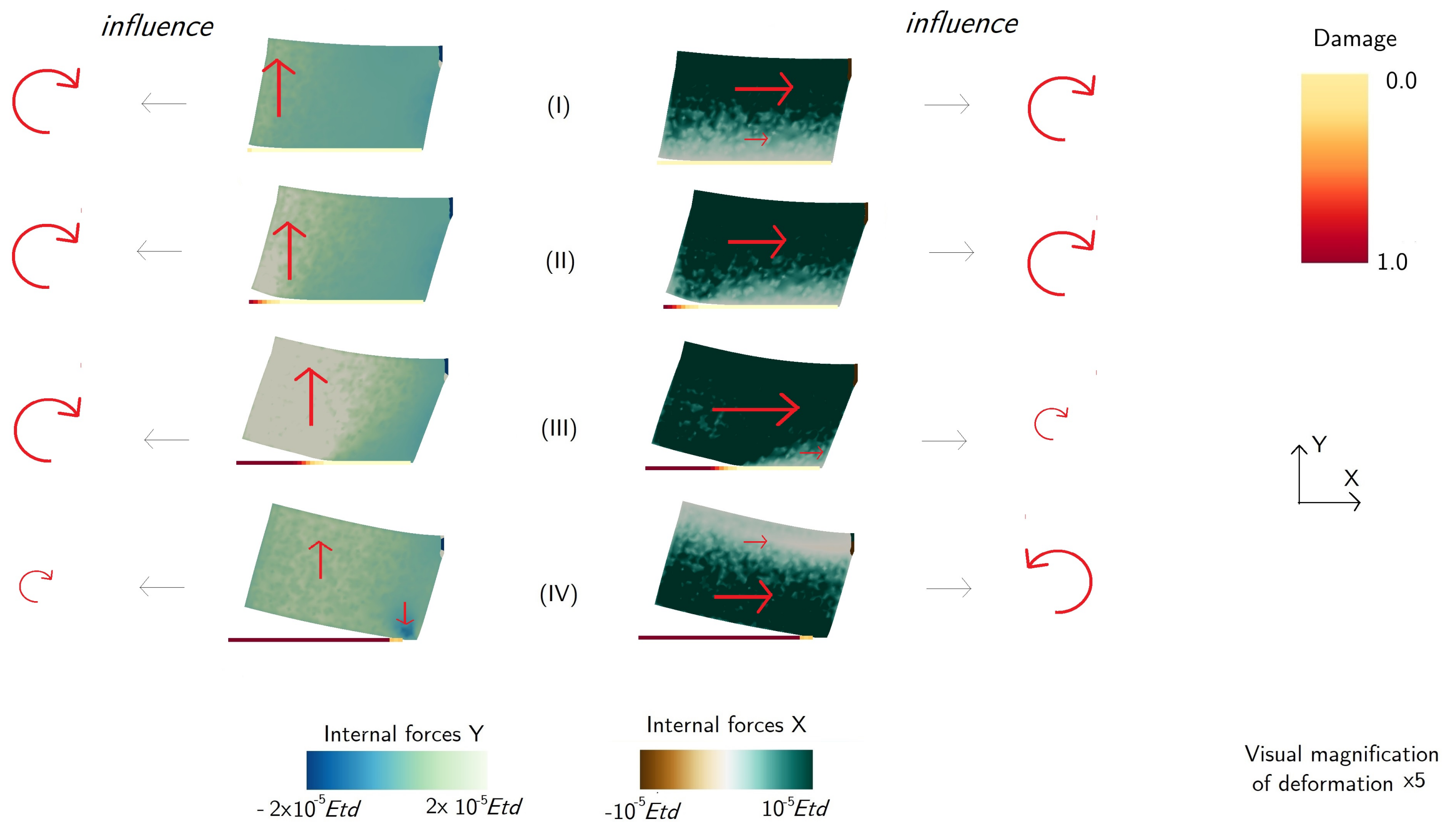

Figure 59: Internal force diagrams of the peeling of the simulation that shows a failure mode of curling followed by interfacial cavitation with parameters $(\beta,\, \alpha,\, L/t,\, \theta,\, \zeta,\, \gamma,\, \kappa) = (8,\, 2,\, 2,\, 0.5{\times}10^{-3},\, 32{\times}10^{-3},\, 2.6,\, 0.4)$. The imposed displacement is increasing from (I) up over the figure. The deformation of the pad is visually magnified for clarity, and the damage of the surface is shown on the initial surface. The left figures show color-coded the internal forces in the Y-direction (axes provided on the figure for reference) and the right figure shows color-coded the internal forces in the X-direction, the pulling direction. For the convenience of the reader, the forces observed in the color-code will are schematically drawn as red arrows. The resulting couples from these forces are also indicated.

Consider Figure 60, for the curling plus interfacial cavitation failure mode. In step (I) the vertical forces are located at pulling end and the opposite end, creating a couple on the full pad. The horizontal forces are located near the pulling end and in the backing, creating a couple at the beginning of the pad. In Figure (II), both types of movement continue during the development of the curling detachment. In Figure (III), after the interfacial cavity has failed, a vertical downward force is noticed at the region where the pad failed and an additional vertical upwards force right around the detachment front. This difference in vertical forces can be related to the horizontal force where the horizontal force is spread mostly over the detached region near the surface. Both force distributions cause an additional set of couples. Finally, in Figure (IV), the horizontal forces are distributed all over the pad and the vertical forces near the detachment front are diminishing.

Consider now Figure 61 for the interfacial cavitation, combined with steady peeling and curling failure mode. During phase (I), the only horizontal and vertical forces are located now near the pulling end. In Figure (II), the additional vertical forces around the detachment front and the concentration of horizontal forces at the detached surface are apparent. The propagation of this region continues in Figure (III). In figure (IV), an additionally formed couple under the influence of vertical forces released by the stress relaxation behind the detachment front is seen, as the detached region becomes longer. In Figure (V), this region propagates away from the first couple as a reattachment is observed, under the influence of this region (the blue zones). This reattachment location now also has an influence on the vertical force distributions, as an additional couple is observed there as well.

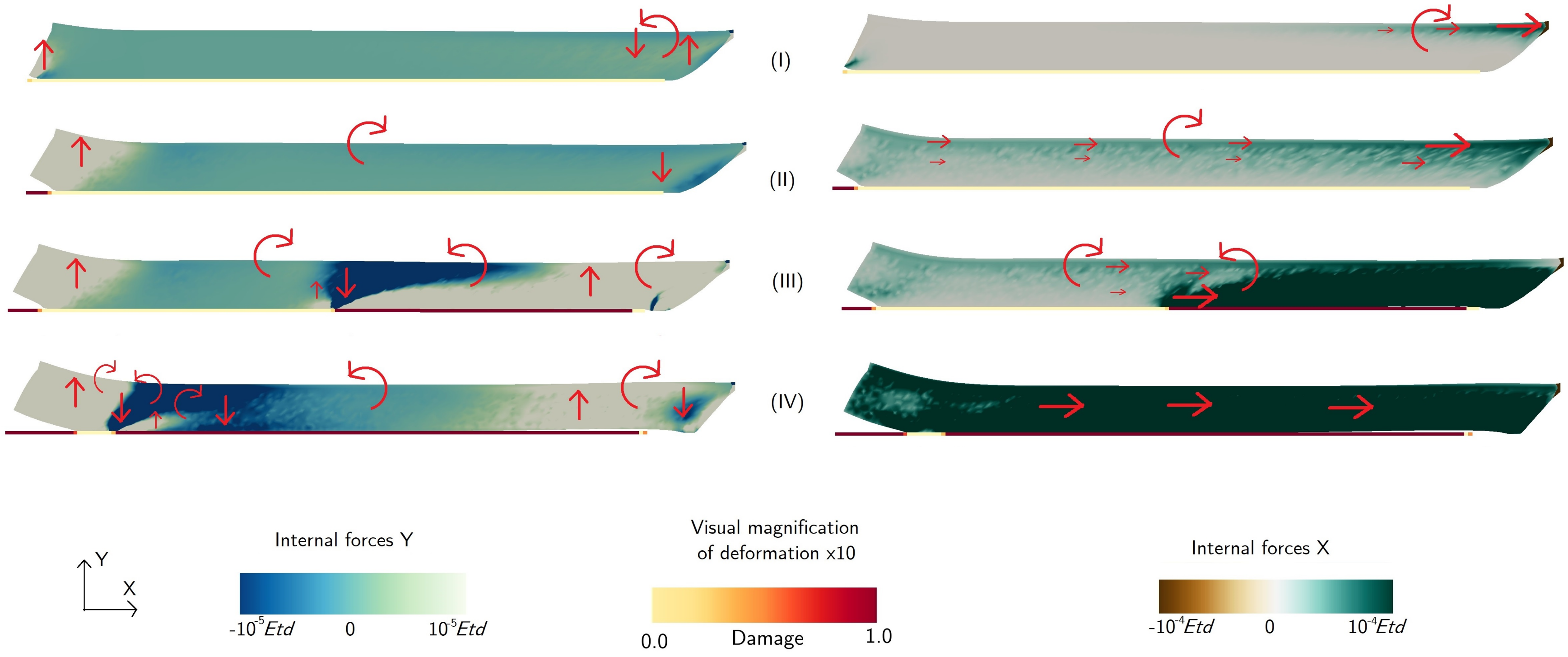

Figure 60: Internal force diagrams of the peeling of the simulation that shows a curling failure mode with parameters (β, α, L/t, θ, ζ, γ, κ) $=$ (20, 2, 15, 0.5$\times10^{-3}$, 60$\times10^{-3}$, 4.8, 0.4). The imposed displacement is increasing from (I) up over the figure. The deformation of the pad is visually magnified for clarity, and the damage of the surface is shown on the initial surface. The left figures show color-coded the internal forces in the Y-direction (axes provided on the figure for reference) and the right figure shows color-coded the internal forces in the X-direction, the pulling direction. For the convenience of the reader, the forces observed in the color-code will are schematically drawn as red arrows. The couples resulting from these forces are also indicated.

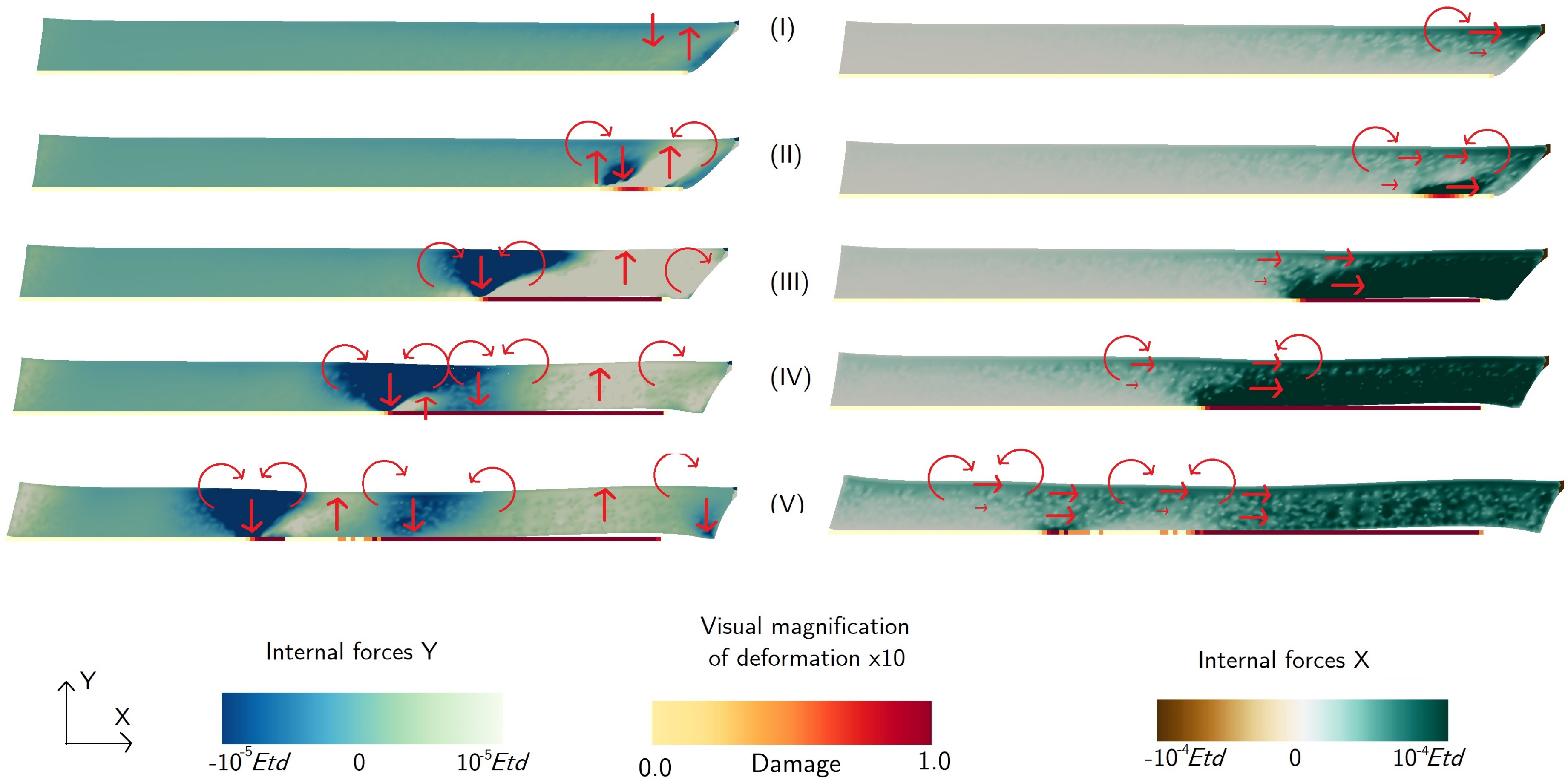

Figure 61: Internal force diagrams of the peeling of the simulation that shows a combined failure mode of interfacial cavitation, steady peeling and curling with parameters (β, α, L/t, θ, ζ, γ, κ) $=$ (8, 2, 15, 0.5×10^{-3}, 32×10^{-3}, 2.6, 0.4). The imposed displacement is increasing from (I) up over the figure. The deformation of the pad is visually magnified for clarity, and the damage of the surface is shown on the initial surface. The left figures show color-coded the internal forces in the Y-direction (axes provided on the figure for reference) and the right figure shows color-coded the internal forces in the X-direction, the pulling direction. For the convenience of the reader, the forces observed in the color-code will are schematically drawn as red arrows. The couples resulting from these forces are also indicated.

C.5 Parameter Sensitivity of Simulation

Each parameter variation is done by increasing and decreasing the design parameter from the reference case detailed in table 6.

C.5.1 *Influence of Backing Stiffness β*

Increase of the parameter $\beta = \frac{E_b t_b}{Et}$, the amount of energy contained in the backing versus the amount of energy in the soft adhesive, results in the distribution of the imposed forces over a larger part of the backing. As a result, as shown in Figure 62, as higher beta creates larger normal and tangential openings in the opposite end of the pad, making the steady peeling phase faster and the region of curling larger.

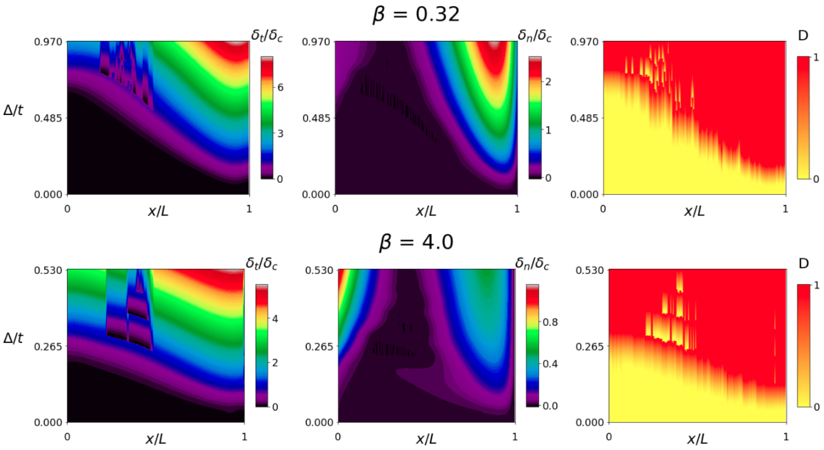

Figure 62: Detachment analysis of the surface of two pads with as only different parameter β. The amount of displacement is advanced over the y-axis and the pad length is advanced over the x-axis on each of the Figures. The left graphs show the opening of the adhesive surface in the tangential direction, the middle graphs the opening in the normal direction, and the right graphs the damage of the surface.

The faster peeling wave for a higher β is also linked to a global faster failure of elements (Figure 63 right) and a higher force during this failure (Figure 63 left). As the forces spread out over a longer part of the pad, once the failure wave onsets, it can propagate faster. However, for its initial development, a larger force will be required.

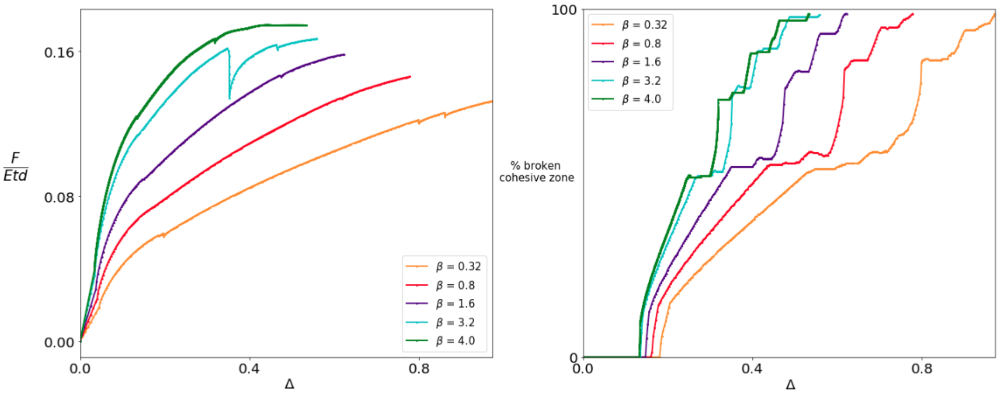

Figure 63: Force-displacement (left) and percentage of failure-displacement (right) graphs for pads with as only different parameter β. The force is the total pulling force in the X-direction that needs to be exerted upon the pulling end of the backing to pull this end the amount of displacement imposed. The large drop and re-increase in the force curves is a mesh effect as shown before in Appendix C.2: the curve would continue smoothly there.

C.5.2 Influence of Backing Thickness α

The influence of parameter $\alpha = \frac{t_b}{t}$ on the global force as shown in Figure 64 is small compared to the influence of β has, as shown in the previous section. The force graph keeps the same shape and forces increase marginally as α increases. For the global failure graph, 4 of the 5 cases almost coincide, the fifth case with the highest α value shows relatively less reattachment. Recall that by varying α, but no other parameters, the total amount of elastic energy in the pad is kept constant, but only the backing thickness is varied. It is not surprising this has relatively less impact than varying the parameter β which does affect the amount of the elastic energy. The increase in force with increasing backing thickness is the result of more material that the stresses can be distributed over in the backing.

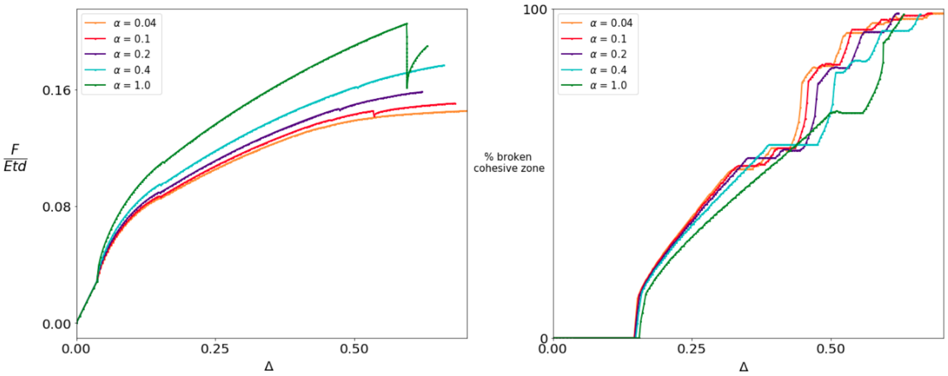

Figure 64: Force-displacement (left) and percentage of failure-displacement (right) graphs for pads with as only different parameter α. The force is the total pulling force in the X-direction that needs to be exerted upon the pulling end of the backing to pull this end the amount of displacement imposed.

On Figure 65 the influence of α on the opening and damage development profile is shown. The damage graph development of the larger α value, a thicker backing, shows multiple larger slow failure events, while the damage graph for a smaller α value shows smaller fast failure events. This is the result of the different distributions of forces over a higher backing thickness and the resulting higher moments acting on the soft adhesive. The abrupt events then result in more reattachment waves, which result in the different global failure curve observed in Figure 64 (right).

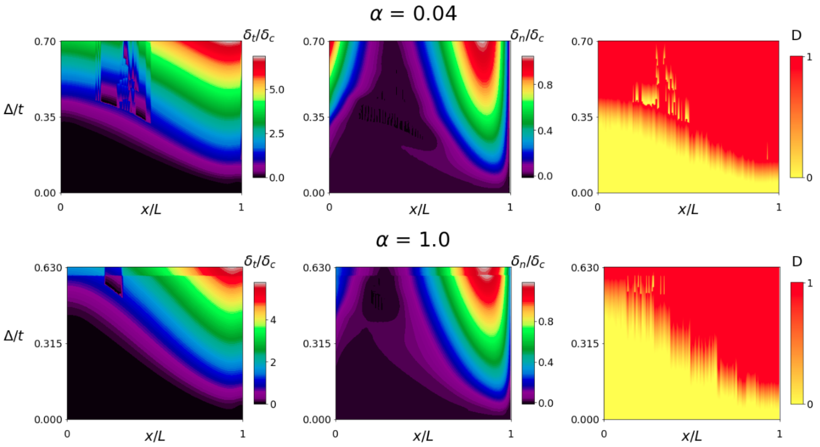

Figure 65: Detachment analysis of the surface of two pads with as only different parameter α. The amount of displacement is advanced over the y-axis and the pad length is advanced over the x-axis on each of the Figures. The left graphs show the opening of the adhesive surface in the tangential direction, the middle graphs the opening in the normal direction, and the right graphs the damage of the surface.

C.5.3 *Influence of Pad Length L/t*

All the force-displacement curves (Figure 66) coincide on the same generic curve until right before their failure. They appear to follow the same initiation and peeling pattern, and only differ once curling of the opposite end is reached. To observe this on the percentual failure graph (Figure 66 right), remark that the percentage of failure is expressed in terms of the length of the pad: the curves coincide here as well.

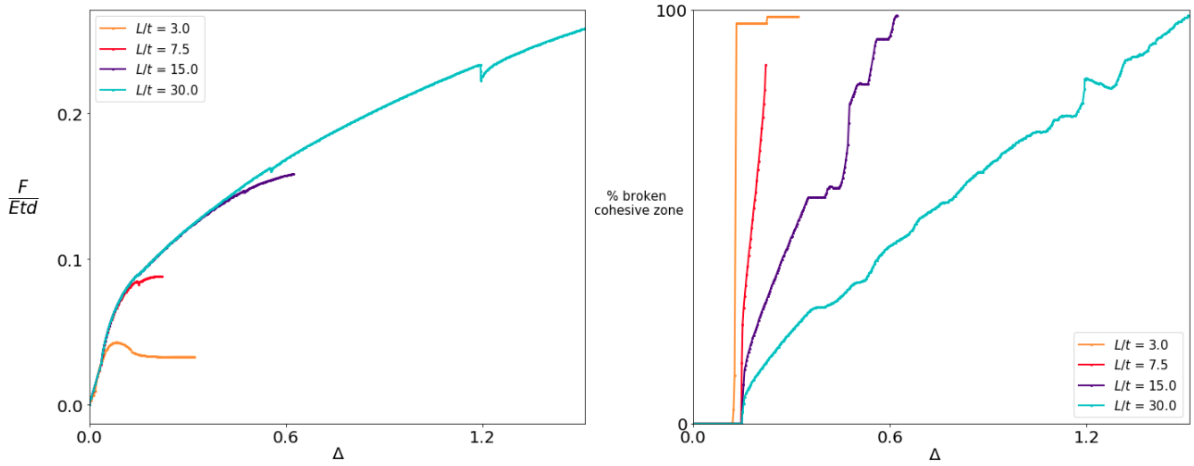

Figure 66: Force-displacement (left) and percentage of failure-displacement (right) graphs for pads with as only different parameter L/t. The force is the total pulling force in the X-direction that needs to be exerted upon the pulling end of the backing to pull this end the amount of displacement imposed.

This is supported by the opening profiles on Figure 67 where for the case of a low L/t immediately curling is observed, while for the high L/t value steady peeling occurs, with curling at the opposite end right before full failure.

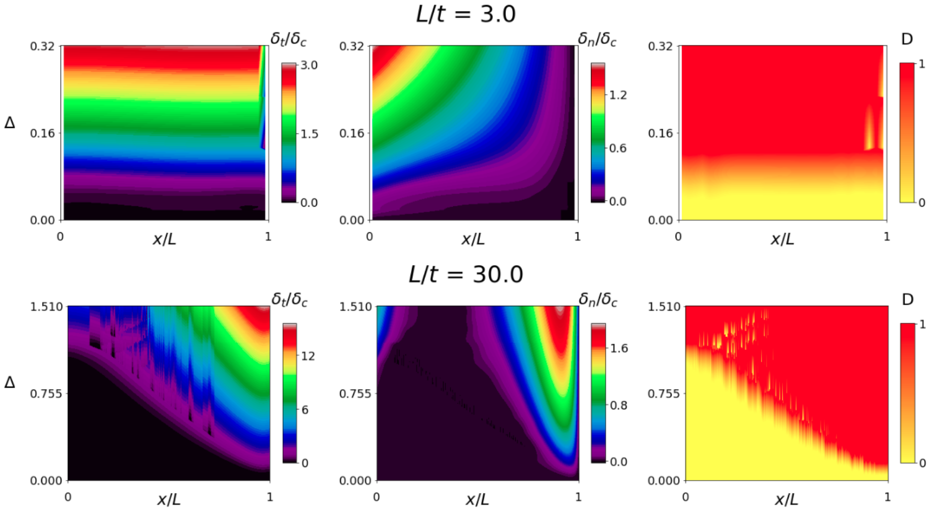

Figure 67: Detachment analysis of the surface of two pads with as only different parameter L/t. The amount of displacement is advanced over the y-axis and the pad length is advanced over the x-axis on each of the Figures. The left graphs show the opening of the adhesive surface in the tangential direction, the middle graphs the opening in the normal direction, and the right graphs the damage of the surface.

C.5.4 *Influence of Bond Stiffness* γ

To vary γ, there are multiple possibilities of parameters to vary. Recall that $\gamma = kt/E = \frac{\sigma_c t}{\delta_0 E}$. As t is used as the length normalization unit and E is used as the energetic normalization unit, they are kept constant. Secondly, σ_c is found as well in parameter ζ. Thus to vary γ as the only parameter, δ_0 and by extension k is varied. The global behavior is observed to be not changed in Figure 68. When looking at the linear elastic behavior in Figure 68 left for small displacements, a difference is observed: the initial elastic slope is affected, which results from a change in the linear elastic slope of the cohesive law k. Despite this, at the onset of failure, this difference disappears and different curves coincide.

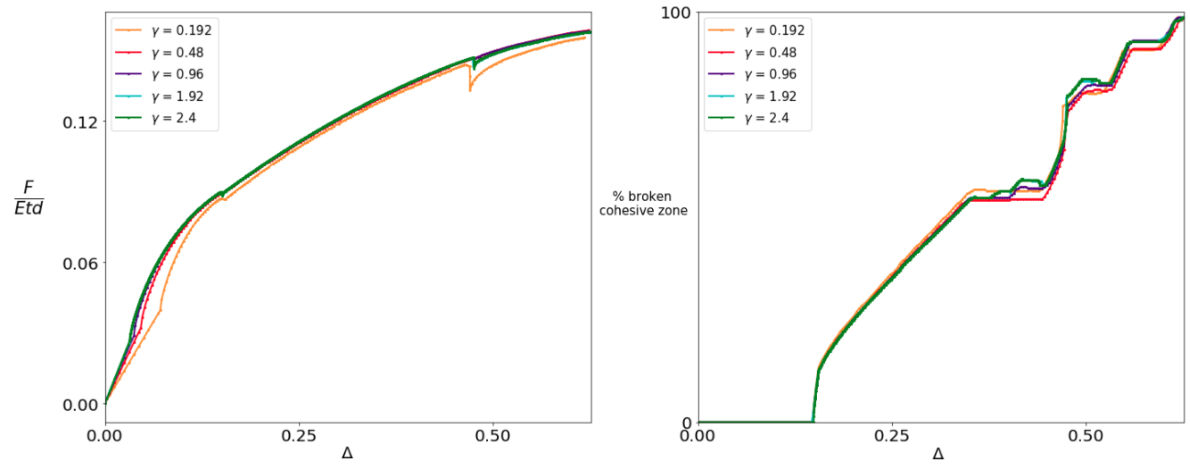

Figure 68: Force-displacement (left) and percentage of failure-displacement (right) graphs for pads with as only different parameter γ. The force is the total pulling force in the X-direction that needs to be exerted upon the pulling end of the backing to pull this end the amount of displacement imposed.

The opening profiles on Figure 69 also show little difference, apart from abrupter failure for lower values of γ. As a lower γ means a higher δ_0 and thus a longer elastic phase and shorter softening phase, this seems to be related to the abrupter development of softening.

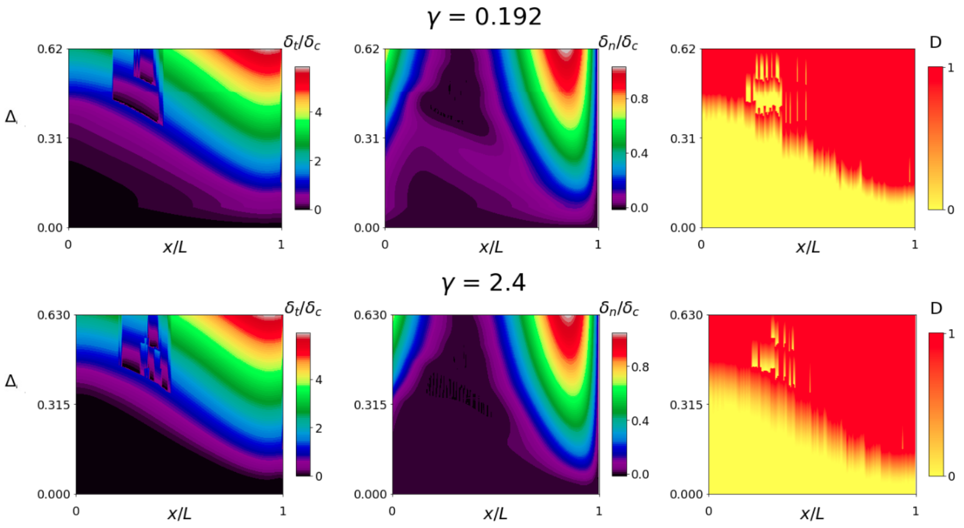

Figure 69: Detachment analysis of the surface of two pads with as only different parameter γ. The amount of displacement is advanced over the y-axis and the pad length is advanced over the x-axis on each of the Figures. The left graphs show the opening of the adhesive surface in the tangential direction, the middle graphs the opening in the normal direction, and the right graphs the damage of the surface.

C.5.5 Influence of Mixed-mode Energy Ratio κ

In all earlier simulations of this section, $\kappa = \frac{G_{c,II}}{G_{c,I}}$ was 1. Thus the change of cohesive zone properties applied both to mode I and mode II cohesive laws. To change κ, either one of them could be kept constant. For completeness, both will be done here. First, κ will be varied by varying the mode I law and keeping the mode II constant. In the force-displacement graphs and global failure on Figure 70 no difference can be observed. The large drops and re-increases of force at the end of the graph are a mesh effect as shown before in Appendix C.2: the curve would continue smoothly there and this is not a stick-slip event.

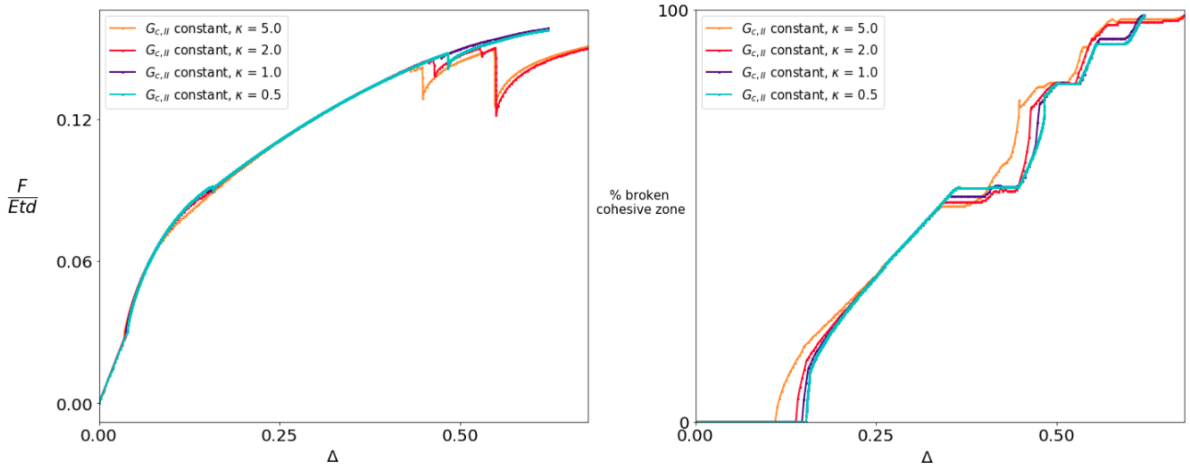

Figure 70: Force-displacement (left) and percentage of failure-displacement (right) graphs for pads with as only different parameter κ, while keeping $G_{c,II}$ constant. The force is the total pulling force in the X-direction that needs to be exerted upon the pulling end of the backing to pull this end the amount of displacement imposed.

The opening profiles on Figure 71 left and middle show no difference in shape but an expected difference in values for the opening: in case of a higher κ, i.e., a lower $G_{c,I}$, the total energy in the mixed modes is lower and thus both the tangential and normal opening are larger for the same force. The damage profile on Figure 71 right corresponds in location, but is more grouped for lower κ. This can be explained again by a higher total cohesive energy.

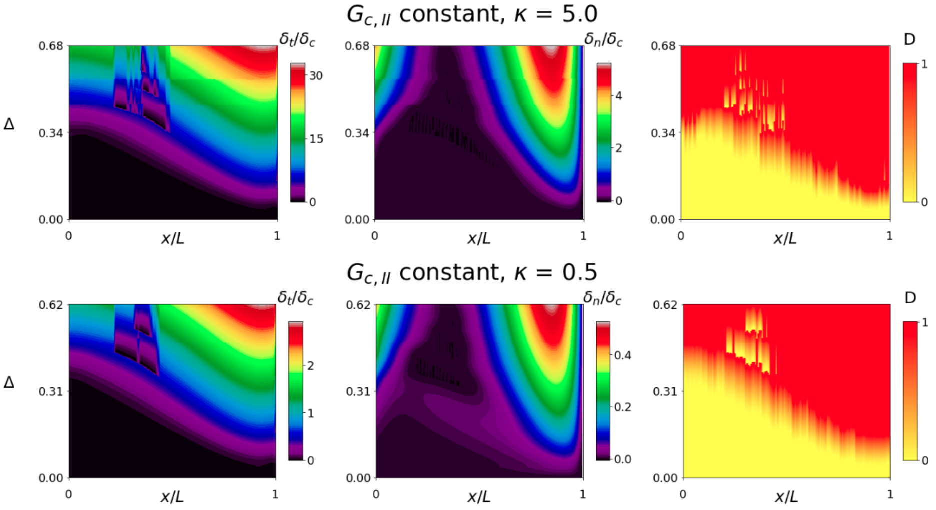

Figure 71: Detachment analysis of the surface of two pads with as only different parameter κ, while keeping $G_{c,II}$ constant. The amount of displacement is advanced over the y-axis and the pad length is advanced over the x-axis on each of the Figures. The left graphs show the opening of the adhesive surface in the tangential direction, the middle graphs the opening in the normal direction, and the right graphs the damage of the surface.

Next, κ is varied by keeping the mode I cohesive law constant and varying the mode two law. In this case, a higher κ results in a higher force (Figure 72 left) as it is linked to a higher mode II energy. Based on this, mode II cohesive energy is determinant for the global force. Secondly, a higher κ results in less reattachment (Figure 72 right and Figure 73 right).

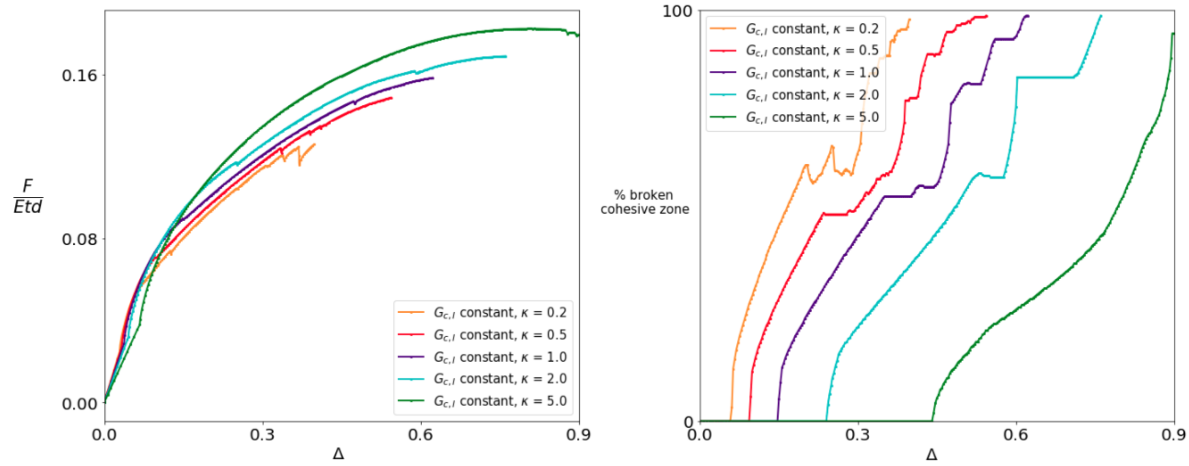

Figure 72: Force-displacement (left) and percentage of failure-displacement (right) graphs for pads with as only different parameter κ, while keeping $G_{c,I}$ constant. The force is the total pulling force in the X-direction that needs to be exerted upon the pulling end of the backing to pull this end the amount of displacement imposed.

In the opening profiles, a higher κ results in the further propagation of the tangential opening, and similarly for more curling: the forces spread out further in the pad. From this, the influence of the mode II cohesive energy is the more important one for the simulation relative to mode I.

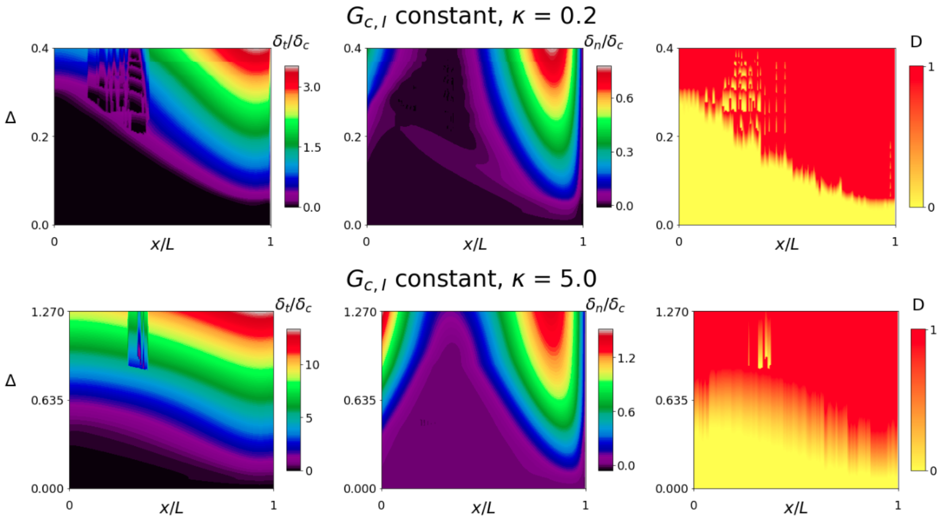

Figure 73: Detachment analysis of the surface of two pads with as only different parameter κ, while keeping $G_{c,II}$ constant. The amount of displacement is advanced over the y-axis and the pad length is advanced over the x-axis on each of the Figures. The left graphs show the opening of the adhesive surface in the tangential direction, the middle graphs the opening in the normal direction, and the right graphs the damage of the surface.

C.5.6 Influence of Velocity v'

While v' is a numerical necessity to introduce rather than a physical parameter, its sensitivity reveals where the potential shortcomings of the current simulation are. The forces increase with increasing v and the amount of reattachment increases as well (Figure 74). The amount of force is highly dependant on this value and thus likely quantitatively not corresponding to experiments. Meanwhile, for a correct estimate of the amount of reattachment, a low value of v' is important. Moreover, the exact speed of development of these reattachment areas is uncertain.

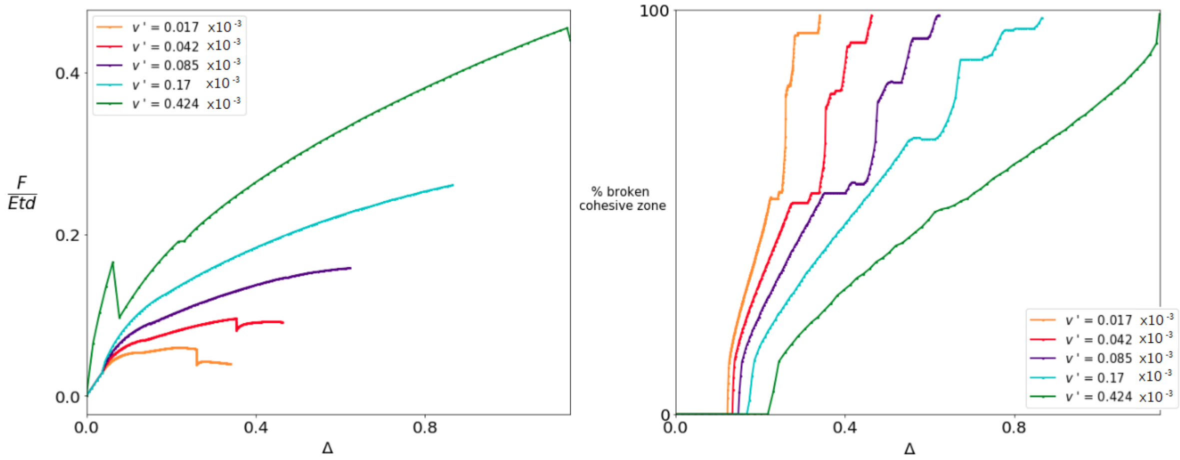

Figure 74: Force-displacement (left) and percentage of failure-displacement (right) graphs for pads with as only different parameter v'. The force is the total pulling force in the X-direction that needs to be exerted upon the pulling end of the backing to pull this end the amount of displacement imposed.

The opening and reattachment profiles (Figure 75) show that lower v' values favor curling. Again, a low enough value of v' is important to ensure forces in the dynamic simulation have the time to redistribute as they would in a fully static equilibrium.

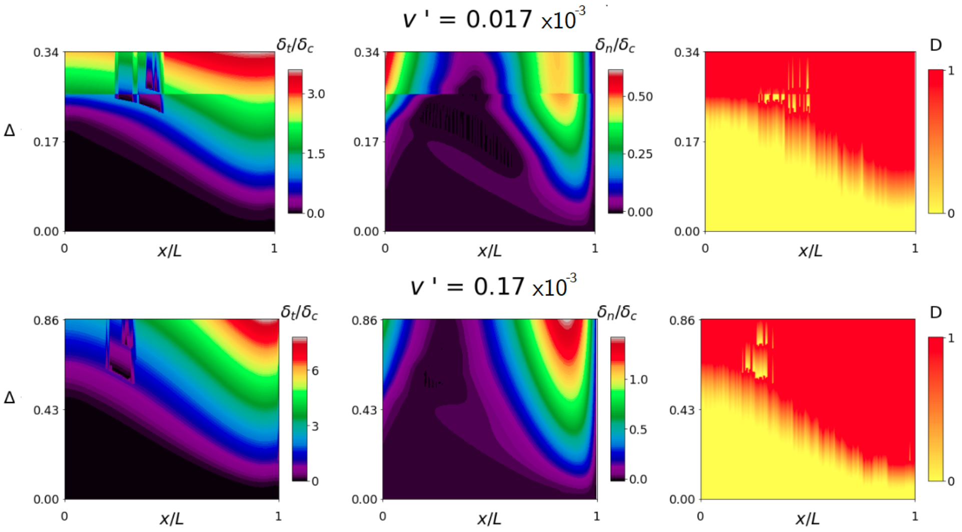

Figure 75: Detachment analysis of the surface of two pads with as only different parameter v'. The amount of displacement is advanced over the y-axis and the pad length is advanced over the x-axis on each of the Figures. The left graphs show the opening of the adhesive surface in the tangential direction, the middle graphs the opening in the normal direction, and the right graphs the damage of the surface.

C.5.7 Influence of Damping T_{damp}

Similar to v', T_{damp} is a numerical necessity. The effects of increasing damping, (Figure 76) correspond to a large degree to the effects of increasing the speed. As damping is increased, forces increases and reattachment decreases. This provides another pointer to conclude that the reattachment is linked to dynamic waves.

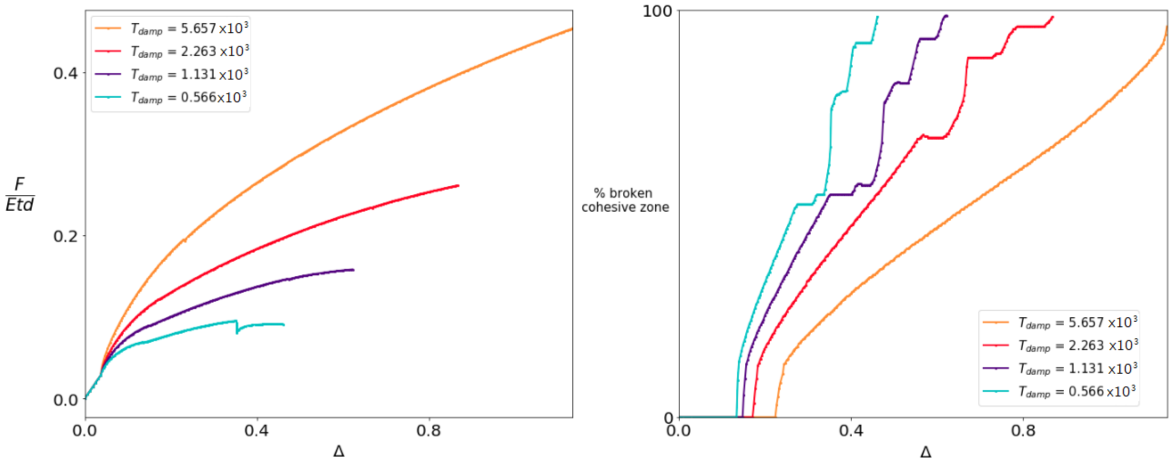

Figure 76: Force-displacement (left) and percentage of failure-displacement (right) graphs for pads with as only different parameter T_{damp}. The force is the total pulling force in the X-direction that needs to be exerted upon the pulling end of the backing to pull this end the amount of displacement imposed.

The opening profiles in Figure 77 provide again show similarities between increasing T_{damp} and increasing velocity: both disfavor curling. The propagation of forces to the opposite end is thus at least partially dynamic.

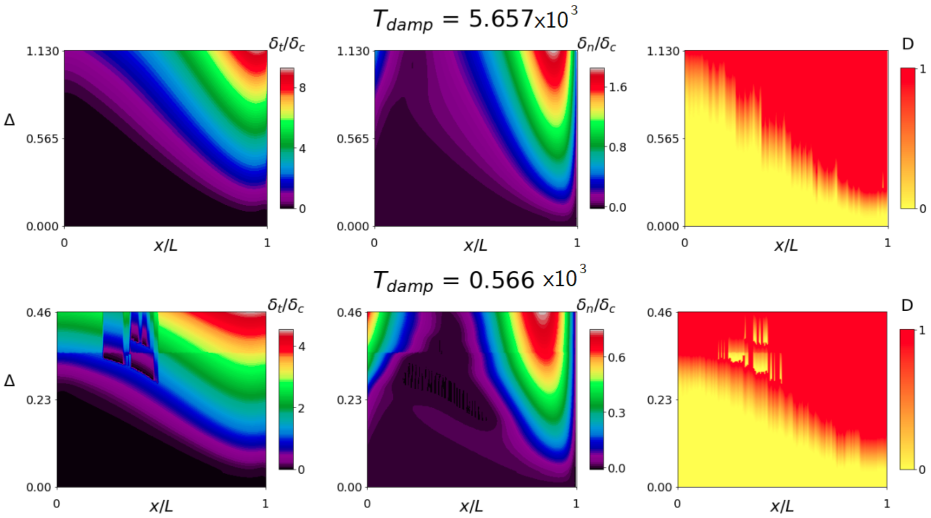

Figure 77: Detachment analysis of the surface of two pads with as only different parameter T_{damp}. The amount of displacement is advanced over the y-axis and the pad length is advanced over the x-axis on each of the Figures. The left graphs show the opening of the adhesive surface in the tangential direction, the middle graphs the opening in the normal direction, and the right graphs the damage of the surface.

C.6 Three-dimensional Simulation

As discussed in Section 4.4, numerical limitations have prevented the use of a full 3D model for this study. Nevertheless, a 3D model was developed and tested. The same properties as for the simulation showing interfacial cavitation in Section 5.1.1 were used, with additionally a depth parameter of $d = 16mm = 2 \cdot t$. In the linear region, this provides correspondence with the two-dimensional simulation. Moreover, the start of the development of the interfacial cavity can be studied in detail and matches experimental behavior.

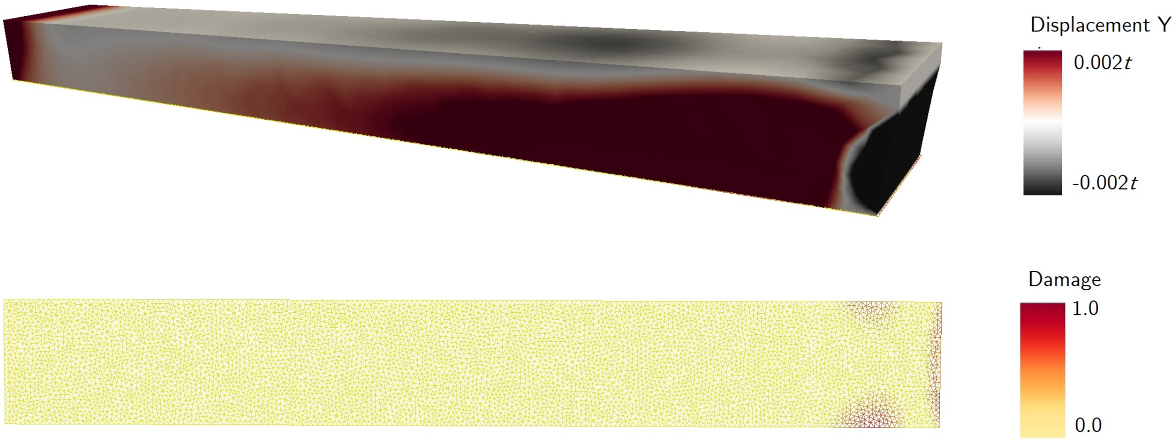

Figure 78: State of the 3D simulation of the pad with properties (β, α, L/t, d/t, θ, ζ, γ, κ) =(8, 2, 8, 2, 0.5$\times10^{-3}$, 8$\times10^{-3}$, 0.64, 0.4) . The top graph shows the deformation state and the bottom graph the damage of the surface.

In Figure 78 top, the state of the pad at maximal displacement that could be computationally achieved ($\Delta = 0.12$) is shown. The top figure shows the deformation of the pad visually, with the deformation in the Y-direction also colored. In the bottom figure, the cohesive surface damage is shown. Especially the cohesive damage profile is interesting, as when comparing it to the experimental detachment profile in Figure 15a (I.b), the same initiation of failure on both sides of the pad close to the pulling end is retrieved. Further, the displacement profile in this three-dimensional simulation corresponds to the one retrieved in the two-dimensional simulation.